DIRECTION FINDING IN THE PRESENCE OF ARRAY IMPERFECTIONS,
MODEL MISMATCHES AND MULTIPATH

A THESIS SUBMITTED TO
THE GRADUATE SCHOOL OF NATURAL AND APPLIED SCIENCES
OF
MIDDLE EAST TECHNICAL UNIVERSITY

BY

AHMET M. ELBIR

IN PARTIAL FULFILLMENT OF THE REQUIREMENTS
FOR
THE DEGREE OF DOCTOR OF PHILOSOPHY
IN
ELECTRICAL AND ELECTRONICS ENGINEERING

JUNE 2016

Approval of the thesis:

DIRECTION FINDING IN THE PRESENCE OF ARRAY IMPERFECTIONS, MODEL MISMATCHES AND MULTIPATH

submitted by **AHMET M. ELBIR** in partial fulfillment of the requirements for the degree of **Doctor of Philosophy in Electrical and Electronics Engineering Department, Middle East Technical University** by,

Prof. Dr. Gülbin Dural Ünver
Dean, Graduate School of **Natural and Applied Sciences**
_____

Prof. Dr. Gönül Turhan Sayan
Head of Department, **Electrical and Electronics Engineering**
_____

Prof. Dr. T. Engin Tuncer
Supervisor, **Electrical and Electronics Engineering**
Department, METU
_____

Examining Committee Members:

Prof. Dr. Orhan Arıkan
Electrical and Electronics Engineering Department,
Bilkent University
_____

Prof. Dr. T. Engin Tuncer
Electrical and Electronics Engineering Department, METU
_____

Prof. Dr. Çağatay Candan
Electrical and Electronics Engineering Department, METU
_____

Assoc. Prof. Dr. Umut Orguner
Electrical and Electronics Engineering Department, METU
_____

Assist. Prof. Dr. Yakup Özkazanç
Electrical and Electronics Engineering Department,
Hacettepe University
_____

Date:
_____

I hereby declare that all information in this document has been obtained and presented in accordance with academic rules and ethical conduct. I also declare that, as required by these rules and conduct, I have fully cited and referenced all material and results that are not original to this work.

Name, Last Name: AHMET M. ELBIR

Signature   :

ABSTRACT

DIRECTION FINDING IN THE PRESENCE OF ARRAY IMPERFECTIONS, MODEL MISMATCHES AND MULTIPATH

Elbir, Ahmet M.

Ph.D., Department of Electrical and Electronics Engineering

Supervisor   : Prof. Dr. T. Engin Tuncer

June 2016, 117 pages

In direction finding (DF) applications, there are several factors affecting the estimation accuracy of the direction-of-arrivals (DOA) of unknown source locations. The major distortions in the estimation process are due to the array imperfections, model mismatches and multipath. The array imperfections usually exist in practical applications due to the nonidealities in the antenna array such as mutual coupling (MC) and gain/phase uncertainties. The model mismatches usually occur when the model of the received signal differs from the signal model used in the processing stage of the DF system. Another distortion is due to multipath signals. In the multipath scenario, the antenna array receives the transmitted signal from more than one path with different directions and the array covariance matrix is rank-deficient. In this thesis, three new methods are proposed for the problems in DF applications in the presence of array imperfections, model mismatches and multipath.

In the first problem, calibration of antenna arrays mounted on aeronautical vehicles is considered. The complete 3-D model of an antenna array and a UH-60 helicopter is constructed and simulated in a numerical electromagnetic tool, FEKO, and the array observations are obtained both in time and frequency. When the antenna arrays are mounted on such platforms, antenna pattern and characteristics change significantly leading to erroneous DF results. In this thesis, a new calibration technique is proposed when the vehicle is on the ground. In ground calibration, the major error sources

are the reflections from the platform and the multipath from the ground. In order to mitigate these distortions, a time-gating method is proposed. When the received signals from the antennas are observed in time, the reflections are present with a time delay after the desired signal component. This part of the signals is gated and sufficiently clean calibration data is obtained for DF operation. The evaluation of the calibration data is done using both correlative interferometer and the MUSIC algorithms. The proposed method is advantageous for its simplicity, accuracy and cost effectiveness.

In the second problem, a DF scenario is considered where the antenna array receives a mixture of a far-field signal and its near-field multipaths. Due to the model mismatch of the received signal components, both far- and near-field signal models should be used accordingly for accurate parameter estimation. Moreover, the array covariance matrix is rank-deficient due to multipath so that the subspace methods cannot be directly used for accurate DOA estimation. A new method is proposed for the estimation of DOA angles of far- and near-field signals and the ranges of near-field multipaths. 2-D DOA angle of the far-field source is estimated by using a calibration technique. A near-to-far-field transformation is proposed to suppress the far-field components of the array output so that the near-field source parameters can be estimated. Then spatial smoothing is employed to estimate the near-field source DOA angles. In order to estimate the near-field source ranges, a compressed sensing approach is presented where a dictionary with near-field sources with different ranges is employed. The proposed method is evaluated using close-to-real world data generated by a numerical electromagnetic tool, Wireless Insite, where the array and transmitter are placed in an irregular terrain and the array data is generated using full 3-D propagation model. It is shown that unknown source parameters can be estimated effectively showing the potential of the proposed approach in applications involving high-frequency direction finding and indoor localization.

In the third problem, 2-D DOA and MC coefficient estimation is considered for arbitrary array structures. Previous methods in the literature are usually proposed for certain array geometries and show limited performance at low SNR or for small number of snapshots. In this thesis, compressed sensing is used to exploit the joint-sparsity of the array model to estimate both DOA and MC coefficients with a single snapshot for an unstructured array where the antennas are placed arbitrarily in space. A joint-sparse recovery algorithm for a single snapshot (JSR-SS) is presented by embedding the source DOA angles and MC coefficients into a joint-sparse vector. A dictionary matrix is defined by considering the symmetricity of the MC matrix for the unstructured antenna array. The proposed method is extended to the multiple snapshots, and the joint-sparse recovery algorithm with multiple snapshots (JSR-MS) is developed. A new joint-sparsity structure, namely, joint-block-sparsity is introduced to take advantage of the structure in the composite matrix involving both DOA and MC coefficients. In order to utilize the joint-block-sparsity effectively in the optimization

problem, new norm structures, namely L-2,2,0- and L-2,2,1-norms are defined. The same technique is modified in order to solve the gain/phase mismatch problem in multipath scenario. Several simulations are done in order to show the performance of the proposed techniques.

Keywords: Direction Finding, Array Signal Processing, Mutual Coupling, Gain/phase Mismatch, Calibration.

ÖZ

DİZİLİM KUSURLARI, MODEL UYUŞMAZLIKLARI VE ÇOK-YOLLU
YANSIMALARIN OLDUĞU DURUMDA YÖN BULMA

Elbir, Ahmet M.

Doktora, Elektrik ve Elektronik Mühendisliği Bölümü

Tez Yöneticisi   : Prof. Dr. T. Engin Tuncer

Haziran 2016 , 117 sayfa

Yön bulma (YB) uygulamalarında, bilinmeyen kaynak konumlarının varış-yönünün (VY) kestirim doğruluğunu etkileyen birçok etmen vardır. Kestirim sürecindeki başlıca bozulmalar dizilim kusurları, model uyuşmazlıkları ve çok-yollu yansımalardır. Dizilim kusurları genellikle pratik uygulamalarda ortak bağlaşım (OB) ve genlik/faz uyuşmazlıkları gibi kusurlardan kaynaklanır. Model uyuşmazlıkları genellikle alınan işaretin modeli, YB sisteminin işleme basamağında kullanılan modelden farklılaştığında ortaya çıkar. Bir diğer bozulma nedeni çok-yollu yansıyan işaretlerdir. Çok-yollu yansıma senaryosunda, anten dizilimi yollanan işareti farklı yönlerden birden fazla yoldan alır, öyle ki, işaretler kolayca ayrıştırılamazlar. Bu tezde, dizilim kusurları, model uyuşmazlıkları ve çok-yollu yansımaların olduğu durumda YB uygulamalarındaki sorunlar için dört yeni algoritma önerilmiştir.

Birinci problemde, hava araçları üzerine yerleştirilen anten dizilimlerinin kalibrasyonu incelenmiştir. Anten diziliminin ve UH-60 helikopterin tüm 3-B modeli numerik elektromanyetik programında yaratılmış ve benzetimi yapılıp, anten gözlemleri zamanda ve frekansta elde edilmiştir. Anten dizilimleri bu gibi platformlara yerleştirildiğinde, anten örüntüsü ve karakteristiği önemli ölçüde değişir ve hatalı YB sonuçlarına neden olur. Bu tezde, hava aracı yerde iken yapılan yeni ve kalibrasyon tekniği önerilmiştir. Yerde kalibrasyon işleminde, ana hata unsurları yerden ve platformdan yansıyan çok-yollu yansımalardır. Bu bozulmaları giderebilmek için zamanda pence-

releme yöntemi önerilmiştir. İşaretler antenlerden alınıp zamanda gözlemlendiğinde, yansımalar istenilen işaret bileşeninden bir zaman gecikmesiyle elde edilir. İşaretin bu bölümü pencerelenmiş ve YB işlemi için yeterince iyi bir kalibrasyon verisi elde edilmiştir. Elde edilen kalibrasyon verisinin değerlendirmesi MUSIC algoritması ile yapılmıştır. Önerilen yöntem basitliği, doğruluğu ve düşük maliyetli oluşu ile avantajlıdır.

İkinci problemde, anten diziliminden uzak- ve yakın-alan çok-yollu işaretlerin alındığı bir YB senaryosu incelenmiştir. Alınan işaret bileşenlerindeki model uyuşmazlıklarından dolayı, doğru bir parametre kestirimi için uzak- ve yakın-alan işaret düzgün bir şekilde modellenmelidir. Ayrıca, çok-yollu işaretlerden dolayı, dizilim ortak örtüşme dizeyi eksik kertelidir, öyle ki, bu durumda alt-uzay yöntemleri doğru bir VY kestirimi için doğrudan kullanılamazlar. Uzak- ve yakın-alan işaretlerin VY'si ve yakın-alan çok-yollu işaretlerin menzillerinin kestirimi için yeni bir yöntem önerilmiştir. Uzak-alan işaretin 2-B VY açısı bir kalibrasyon tekniği ile kestirilmiştir. Yakın-alan parametrelerinin kestirilmesi amacıyla, dizilim çıkışındaki uzak-alan bileşenleri yakın-uzak alan dönüşümü kullanılarak bastırılmıştır. Daha sonra, yakın-alan VY'lerini kestirmek amacıyla uzamsal yumuşatma kullanılmıştır. Yakın-alan menzillerin kestirilmesi için farklı menzillere ait yakın-alan kaynakların kullanıldığı bir sözlüğün olduğu sıkıştırılmış algılama yaklaşımı sunulmuştur. Önerilen yöntem, 3-B yayılım modelinin kullanıldığı numerik elektromanyetik benzetim aracı Wireless Insite ile üretilmiş gerçek dünyaya yakın veriler ile değerlendirilmiştir. Önerilen yöntemin yüksek frekans ön bulma ve bina-içi konumlama gibi uygulamalardaki performansını gösteren etkin parametre kestirim sonuçları gösterilmiştir.

Üçüncü problemde, 2-B VY ve OB katsayılarının kestirimi rastgele dizilim yapıları için incelenmiştir. Literatürdeki diğer yöntemler genellikle belirli dizilim yapıları için önerilmiş ve düşük SNR ve az ölçüm sayısı durumunda sınırlı başarım göstermişlerdir. Bu tezde, antenlerin uzayda rastgele konumlandığı bir yapısız dizilim için, tek bir gözlem ile VY ve OB katsayılarının kestirimi için dizilim modelindeki ortak-seyrekliği sıkıştırılmış algılama ile ortaya çıkaran yeni bir yöntem önerilmiştir. Kaynak VY'lerini ve OB katsayılarını ortak-seyrek bir yöneye yerleştiren tek gözlem için ortak-seyrek geri oluşturma (TGOSGO) yöntemi sunulmuştur. Önerilen yöntem, çoklu gözlem durumu için genişletilmiş ve çoklu gözlem için ortak-seyrek geri oluşturma (ÇGOSGO) algoritması geliştirilmiştir. Kompozit bir dizeydeki VY ve OB katsayılarının oluşturduğu yapıdan faydalanarak yeni bir ortak-blok-seyrekli yapısı tanıtılmıştır.

Nihayet son problemde, çok-yollu yayılım ve genlik/faz uyuşmazlıklarının olduğu durumda, rastgele dizilim yapıları için VY kestirimi problemi incelenmiştir. Evre-uyumlu kaynak işaretlerinin VY açıları ve uyuşmazlık parametrelerini kestirmek için bir ortak-seyrek geri oluşturma yöntemi önerilmiştir.

Anahtar Kelimeler: Yön Bulma, Dizilim İşaret İşleme, Ortak Bağlaşım, Genlik/Faz Uyumsuzluğu, Kalibrasyon.

To my daughter, Zeynep.

ACKNOWLEDGMENTS

TABLE OF CONTENTS

APPENDICES

LIST OF TABLES

TABLES

LIST OF FIGURES

FIGURES

CHAPTER 1

INTRODUCTION

1.1 Motivation and Objectives

Direction-of-arrival (DOA) estimation of the plane waves impinging on antenna arrays is an important problem in a variety of fields including, radar, sonar, acoustics and communications [1, 2]. Several high resolution methods are proposed to estimate the DOA angles of unknown source locations such as the multiple signal classification (MUSIC) algorithm [3]. While these methods perform well in ideal scenarios, their performance degrades significantly in case of array imperfections. There are different error sources in array processing some of which are bulletined as below:

- **Array Imperfections:**

  1. Mutual coupling (MC): Due to the interaction between the antennas in the array, the received signal from each antenna is coupled to the other antennas. Hence, MC causes distortions in the array manifold and reduces the direction-finding (DF) accuracy [4, 5].

  2. Gain and phase uncertainties: The received signal from each antenna in the array have certain gain and phase mismatches (GPM) due to the effect of the antenna pattern, temperature changes, instabilities in the electronic circuitry and cabling mismatches [6–8].

  3. Sensor location errors: In certain applications, perfect knowledge of the antenna positions in the array is not possible, for example, in towed arrays or in DF systems where the array needs to be dismantled and reassembled in the field [9, 10].

1

- **Model Mismatches:** Model mismatches occur when the received signal model differs from the array signal model used in the DF operation. While most of the received signals are modeled with the far-field array model [11], near-field signals are also received by the DF sensors. In this case, there is a certain performance loss for parameter estimation due to the model mismatches between the near- and far-field array model.

- **Multipath:** Multipath occurs if the antenna array receives the transmitted signal by two or more paths [12–14]. In this case, it is not easy to distinguish the true source directions since the array covariance matrix is rank deficient.

The motivation of this thesis is to examine and mitigate the effect of these errors in practical DF scenarios so that satisfactory DOA estimation performance can be obtained. Hence, the main objective is to develop novel algorithms for DF problems in the presence of these factors.

1.2 Literature Overview

In this section, a literature overview is presented for the problems investigated in this thesis.

DOA estimation is a problem which is investigated for almost a hundred years. While several different methods are proposed in this context, most of these methods either fail or do not meet the expectations in practical scenarios [4–7, 15].

One of the array imperfection is mutual coupling (MC) [4, 5, 15]. MC affects the array output so that the corrupted array data lead to erroneous DOA estimation results. The effect of MC eventually decreases as the distance between the antenna pairs in the array increases [16–18]. Hence, the antennas should be placed far from each other increasing the array aperture. However, as the array aperture becomes larger, spatial aliasing occurs if the inter-element distance exceeds the half wavelength [19]. Usually, the array separation is selected as half-wavelength and MC is calibrated using signal processing techniques [6, 15, 20].

There are several methods in the literature which estimate the DOA angles in antenna

2

arrays with MC [6,21–24]. The effect of MC is usually mitigated by using the special structure of the MC matrix for fixed array geometries such as linear [15], circular [6] or rectangular [20] arrays. Uniform linear array (ULA) has a banded Toeplitz MC matrix while uniform circular arrays (UCA) and uniform rectangular arrays (URA) have circulant [6] and block-Toeplitz [20] MC structures respectively. If the array structure has arbitrary geometry, the MC matrix for this kind of array does not have any of these forms except that the MC matrix is symmetric [25]. Since the structure of the MC matrix is important to deal with MC effect, MC mitigation for arbitrary arrays is a harder problem in comparison.

In [6], an iterative approach is considered for DOA estimation using ULA and UCA geometries in the presence of MC. In [21] and [22], rank reduction methods are proposed for uniform array structures for uncorrelated source signals. Higher order statistics is used in [23] for DOA estimation using UCA. DOA estimation under multipath propagation and MC is investigated in [14,26,27]. In [14], a maximum likelihood estimator is derived for DOA estimation under multipath and MC for ULA. In [26], a direct data domain approach is proposed with the MUSIC algorithm for DOA estimation of coherent source signals using ULA. An ESPRIT-like method is proposed in [27] for an antenna array with parallel ULA geometry. Mitigation of MC in antenna arrays is still an open problem and being investigated by several researchers.

Gain and phase mismatches cause larger DOA estimation errors as compared to MC since GPM corrupt the gain and phase information of the received signal which are critical for the DF accuracy [28]. While the structure of the MC matrix depends on the array structure, the GPM matrix is usually modeled as a diagonal matrix [6]. Several array calibration methods are proposed in the literature in order to mitigate the effect of GPM [6,7,28–30]. In order to correct the effect of GPM, array calibration is used in [7] and [31] using calibration source antennas with known positions. In [7], a sensor array with an arbitrary geometry is considered where GPM is calibrated. While above methods consider the effect of only GPM on DOA estimation, joint calibration of MC and GPM is performed in [6], [28] and [32].

Array calibration techniques can be divided into offline and online techniques. In offline calibration, sensor array is calibrated using calibration sources with known

locations [28, 31]. While this operation provides satisfactory results, it may be extremely complex to build the physical setup in certain cases. Moreover, the collected calibration data may not represent the whole DF system behavior especially when the system parameters change in time. In order to overcome these difficulties, online calibration techniques are proposed [6, 32]. In online scenario, calibration is performed using the array output of incoming signals from unknown DOA angles. A joint process is carried out where both the unknown GPM parameters and the unknown source DOA angles are estimated at the same time.

Besides the array imperfections, model mismatches due to the near-field signals are also an important issue for DF operation [33]. In order to obtain accurate DF performance, far-field and near-field signals should be treated accordingly. In [34], the ESPRIT algorithm is used for the localization of mixed far- and near-field sources. In [35] and [36], cumulants are used together with the MUSIC algorithm in order to treat both near- and far-field sources. In [37], the MUSIC algorithm is employed by assuming well separated and statistically independent source signals. Similarly, [38] employs the ESPRIT algorithm for the independent source signals in a uniform linear array. Both [37] and [38] use additional assumptions which limit the practical application of these methods. In [39] and [40], near- and far-field sources are assumed to be uncorrelated while in case of multipaths, near-field sources are coherent with the far-field sources.

While the effect of array imperfections on DF accuracy is limited, multipath is the most problematic case within the DF error sources [33]. In multipath scenario, the antenna array receives the same signal from different directions and the true direction of the source cannot be estimated unambiguously using conventional techniques [12, 13]. Although multipath is a dominant factor in DF applications, independent source signal assumption is usually made in the majority of proposed methods in the literature [3, 6, 32, 41]. When this assumption is violated, most of the DF methods fail and cannot provide satisfactory estimation results.

In order to resolve the multipath signals, spatial smoothing is proposed for ULA [42] and URA [43]. In [44] and [27], ESPRIT-like approaches are proposed to estimate the DOA's of coherent source signals in the presence of MC using URA and ULA

4

respectively. In [27], parallel-ULA geometry is used for coherent source localization in case of MC where spatial smoothing [42] and the ESPRIT methods are utilized. Maximum likelihood estimation is proposed to estimate the coherent source DOA's in [26] using ULA structure. When the array structure is different than ULA and URA, smoothing algorithms cannot be employed since they require the Vandermonde array model [11, 45]. For these array structures, array interpolation [46, 47] is proposed to transform the array data to ULA or URA so that the smoothing methods can be applied. However, such approaches also have several disadvantages one of which is te angular sector dependency.

1.3 Thesis Overview

In this thesis, we proposed three new algorithms for the problems in DF applications in the presence of array imperfections, model mismatches and multipath.

In the first problem, calibration of the antenna arrays mounted on aeronautical vehicles is investigated. A method is proposed for the offline calibration of a DF antenna array mounted on the vehicle. In this case, the antenna array should be calibrated before the DF operation. The calibration is done on an open field test area with a flat ground plane. Ground reflections are the main sources of error corrupting the calibration data. The proposed method eliminates the ground reflections by employing a time-gating technique. Calibration data is generated by considering the platform effects. Complete calibration scenario is simulated by using numerical electromagnetic simulation tools.

In the second problem, a DF scenario is considered where the antenna array is placed in a mountainous terrain where near and far-field multipaths occur. This scenario is built using 3-D digital map which is then meshed for a numerical electromagnetic simulation in order to obtain antenna signals. When the antenna array receives multipath reflections which are coherent with the far-field line-of-sight signal, estimating the far- and near-field components becomes a hard-to-solve problem. A new method is proposed to estimate the 2-D DOA of the far-field source and to localize its near-field multipaths. Far-field source DOA is estimated using a calibration technique. A

near-to-far transformation is proposed for the estimation of the near-field source DOA angles. In order to estimate the near-field range parameters, a compressive sensing approach is presented where a dictionary with near-field sources with different ranges is employed. As a result, the proposed method estimates the far-field and near-field source DOAs as well as the range and the signal amplitudes of the near-field sources. This method is evaluated using close-to-real world data generated by a numerical electromagnetic tool, where the array and transmitter are placed in an irregular terrain and array data is generated.

In the third problem, 2-D DOA and MC coefficient estimation is considered for arbitrary array structures. There are limited number of works for arbitrary array structures [48–50] where the DOA estimation problem under MC is considered with the assumption that the number of snapshots is large and the signal-to-noise ratio (SNR) is sufficiently high. When there is a single snapshot, these methods cannot provide accurate DF results. Hence, a new method is proposed for single snapshot scenario. The sparsity of the received source signals in the spatial domain is utilized and a compressed sensing approach [51–54] is presented in order to estimate the unknown source parameters. In order to mitigate the effect of MC, joint-sparsity of the spatial source directions and the MC coefficients is used and a joint-sparse recovery algorithm with a single snapshot (JSR-SS) is proposed. Once the DOA angles are found, the MC coefficients are estimated using the estimated DOA angles. The proposed method is extended to the multiple snapshots, and the joint-sparse recovery algorithm with multiple snapshots (JSR-MS) is developed. A new joint-sparsity structure, namely, joint-block-sparsity is introduced to take advantage of the structure in the composite matrix involving both DOA angles and the MC coefficients. Furthermore, the proposed method is applied for direction finding in the presence of gain/phase mismatches and multipath. Then, the DOA angles and the mismatch parameters are estimated.

Some parts of this thesis are produced from the papers in [28, 33, 55] which are published during the thesis work.

6

1.4 Contributions

The main contributions of the thesis can be summarized as follows:

- [Ch. 3] An efficient calibration technique is proposed for DOA estimation using DF arrays mounted on aeronautical vehicles [28]. The proposed method is advantageous for simplifying the calibration procedure and reducing the cost as well as decreasing the measurement errors compared to the conventional approaches [56–58].

- [Ch. 4] Mixed far- and near-field source localization problem is solved for multipath signals [33]. While this problem is considered in the literature for independent source signals [35, 37], this is the first work that treats the problem in multipath scenario.

- [Ch. 5] 2-D DOA and MC coefficients are estimated for antenna arrays with arbitrary geometries using a single snapshot. JSR with a single snapshot (JSR-SS) algorithm is presented for the solution of this problem. The problem is solved using mixed $l_{2,1}$-norm in order to take advantage of joint-sparsity inherit in the unknown vector.

- [Ch. 5] JSR-SS algorithm is extended to multiple snapshots and JSR with multiple snapshot (JSR-MS) method is developed. Triple mixed norms, $l_{2,2,0}$-norm and $l_{2,2,1}$-norm, are introduced in order to take advantage of joint-sparsity in case multiple snapshots. While mixed $l_{2,1}$-norm is used in the literature [59,60], this is the first time, triple mixed norms are employed.

- [Ch. 5] JSR-SS and JSR-MS methods are applicable for both 1-D and 2-D DOA estimation in case of single and multiple snapshots respectively. In 2-D DOA estimation, azimuth and elevation angles are coupled especially for unstructured arbitrary array geometries. This coupling generates biased estimates and 2-D DOA estimation becomes more problematic. Furthermore "pairing problem" [61] should be solved. The proposed methods use sparsity in two dimensions in order to present a solution without a "pairing problem" when there is mutual coupling between the antennas as opposed to the previous methods [32, 48–50] where a 1-D problem is considered.

7

- [Ch. 5] The DOA angles and MC coefficient parameters can be obtained simultaneously, and hence JSR-SS and JSR-MS can be used as an online calibration [32] technique. This is an important advantage, especially for the applications where mutual coupling coefficients change in time and online calibration is required for an accurate and stable operation.

1.5 Organization of The Thesis

The remainder of this thesis is organized as follows. In Chapter 2, detailed information is provided for the array imperfections, model mismatches and multipath. In Chapter 3, a ground calibration technique is presented for DF arrays mounted on aeronautical vehicles. In Chapter 4, a source localization algorithm is presented for the estimation of DOA angles of far- and near-field sources and the ranges of the near-field reflection points. In Chapter 5, JSR-SS and JSR-MS algorithms are presented for the estimation of 2-D DOA angles and the MC coefficients for arbitrary array structures. Finally, in Chapter 6, conclusions are presented.

CHAPTER 2

THE MAJOR ERROR SOURCES IN DIRECTION FINDING: ARRAY IMPERFECTIONS, MODEL MISMATCHES AND MULTIPATH

In this chapter, the major error sources in direction finding (DF) applications are described in detail. In a DF scenario, the received signals from the antennas in the array are processed in order to estimate the direction-of-arrival (DOA) angle of the source locations. The output of an M-element antenna array can be given as

$$\mathbf{y}(t_i) = \mathbf{C}\mathbf{\Gamma}\mathbf{A}(\Theta)\mathbf{s}(t_i) + \mathbf{e}(t_i) \tag{2.1}$$

where $\mathbf{y}(t_i) = [y_1(t_i), y_2(t_i), \ldots, y_M(t_i)]^T$, $i = 1, \ldots, T$ and T is the number of snapshots. $\mathbf{s}(t_i) = [s_1(t_i), s_2(t_i), \ldots, s_K(t_i)]^T$ and $s_k(t_i)$ is the baseband signal of the kth source and $\mathbf{e}(t_i) = [e_1(t_i), e_2(t_i), \ldots, e_M(t_i)]^T$ is zero-mean spatially and temporarily white Gaussian noise vector. $\mathbf{A}(\Theta)$ is $M \times K$ nominal array steering matrix and defined as

$$\mathbf{A} = [\mathbf{a}(\Theta_1), \mathbf{a}(\Theta_2), \ldots, \mathbf{a}(\Theta_K)] \tag{2.2}$$

where $\Theta_k = (\phi_k, \theta_k)$ represents the azimuth and elevation angles of the kth source respectively. The mth element of the array steering vector $\mathbf{a}(\Theta_k)$ is given as

$$a_m(\Theta_k) = \exp\left\{j\frac{2\pi}{\lambda}\mathbf{r}_k^T\mathbf{p}_m\right\} \tag{2.3}$$

where $j = \sqrt{-1}$, $\mathbf{r}_k = [\cos(\phi_k)\sin(\theta_k) \ \sin(\phi_k)\sin(\theta_k) \ \cos(\theta_k)]^T$, λ is the wavelength and $\mathbf{p}_m = [x_m \ y_m \ z_m]^T$ is the mth antenna position. $\mathbf{C}$ and $\mathbf{\Gamma}$ are the mutual coupling and gain/phase mismatch matrices respectively. The structures of $\mathbf{C}$ and $\mathbf{\Gamma}$ are defined in the following parts of this chapter.

2.1   Mutual Coupling

When transmitted signal is received by an antenna array, each antenna in the array re-transmits a part of the signal due to impedance mismatch. These retransmitted signals are received by each antenna proportional with the distance between the retransmit-ting and receiving antennas. Hence, a coupling between the receiving antennas occurs which is called as mutual coupling (MC).

In Fig. 2.1, an antenna array with two passively loaded antennas is shown [62]. As it is seen, the incident wave strikes the left antenna where it is received and re-scattered. The incident wave and re-scattered waves are vectorially added and received from the right antenna. The same scenario also occurs for the left antenna leading to a coupling between the received signals in the array.
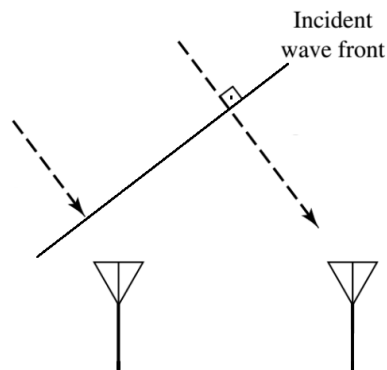
Figure 2.1: An antenna array with two antennas in receive scenario.

MC is modeled in accordance with the geometry of antenna array. For mostly used array geometries in DF applications, the MC matrix in the array signal model can be structured as Toeplitz, circulant and block-Toeplitz for linear [15], circular [6] and rectangular [20] arrays respectively. In the following, the MC matrix structures for different array geometries are explained.

2.1.1   Uniform Linear Array

In a uniform linear array (ULA), the antennas are placed with equal spacing as shown in Fig. 2.2. The distinct MC coefficients are $\{c_m\}_{m=1}^{M}$ for M-element antenna array
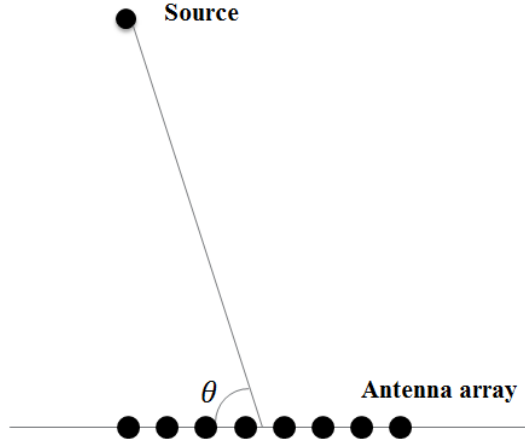
Figure 2.2: Placement of an $M = 8$ antennas in a uniform linear array.

and the form of the MC matrix for an ULA is given as

$$
\mathbf{C}^{ULA} =
\begin{pmatrix}
c_1 & c_2 & c_3 & \dots & c_M \\
c_2 & c_1 & c_2 & \dots & c_{M-1} \\
c_3 & c_2 & \ddots & \ddots & \vdots \\
\vdots & \ddots & \ddots & c_1 & c_2 \\
c_M & c_{M-1} & \dots & c_2 & c_1
\end{pmatrix}.
\tag{2.4}
$$
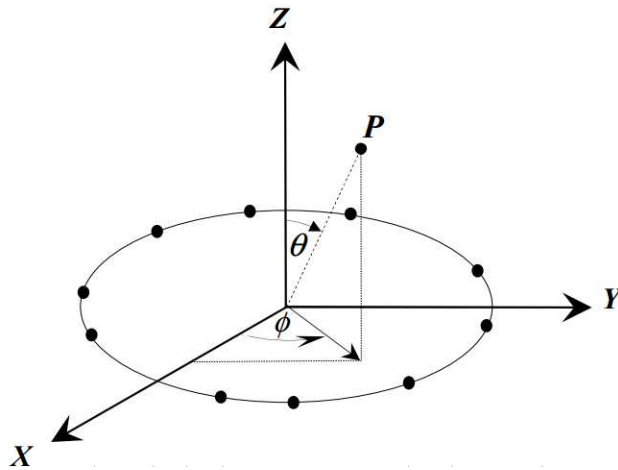
Figure 2.3: Placement of an uniform circular array in xy-plane.

2.1.2 Uniform Circular Array

In a uniform circular array (UCA), antennas are placed in the circumference of the array center as shown in Fig. 2.3 [63]. The structure of the MC matrix depends on

11

whether the number of antennas in the array is even or odd. Then, the form of the MC matrix for UCA is given as follows [6]

For M is even:

$$\mathbf{C}^{UCA} = \begin{pmatrix} c_1 & c_2 & \dots & c_L & c_{L-1} & \dots & c_2 \\ c_2 & c_1 & c_2 & & & & \\ \vdots & c_2 & \ddots & \ddots & & & \\ c_L & & \ddots & & & & \\ c_{L-1} & & & & & & \\ \vdots & & & & & \ddots & \vdots \\ c_2 & & & & & \dots & c_1 \end{pmatrix} \tag{2.5}$$

For M is odd:

$$\mathbf{C}^{UCA} = \begin{pmatrix} c_1 & c_2 & \dots & c_L & c_L & \dots & c_2 \\ c_2 & c_1 & c_2 & & & & \\ \vdots & c_2 & \ddots & \ddots & & & \\ c_L & & \ddots & & & & \\ c_L & & & & & & \\ \vdots & & & & & \ddots & \vdots \\ c_2 & & & & & \dots & c_1 \end{pmatrix} \tag{2.6}$$

where L is the number of distinct MC coefficients and it is given as

$$L = \begin{cases} \frac{M+1}{2}, & M \ \text{odd} \\ \frac{M+2}{2}, & M \ \text{even} \end{cases}. \tag{2.7}$$

2.1.3 Uniform Rectangular Array

In a uniform rectangular array (URA), antennas in the subarrays are placed in the array uniform linearly as in the Fig 2.4 where an $M \times N$ array is shown [64]. The URA consists of M subarrays with size N. Due to the uniform linearity of each subarray, the MC matrix for subarrays is modeled as a Toeplitz matrix. Then, the
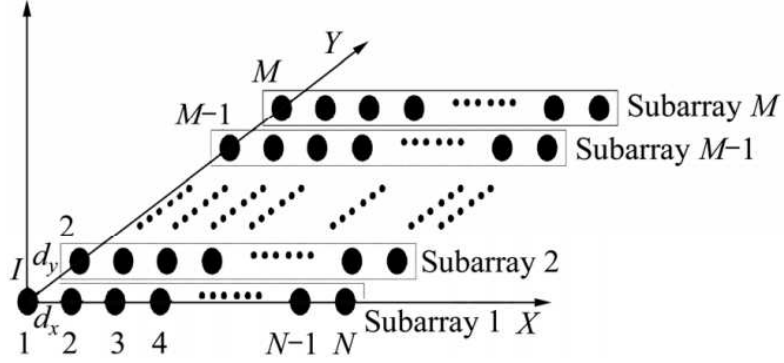
Figure 2.4: Placement of an $M \times N$ uniform rectangular array.

complete MC matrix of URA has a Block-Toeplitz structure, i.e, [20]

$$\mathbf{C}^{URA} = \begin{pmatrix} \mathbf{C}_1 & \mathbf{C}_2 & \dots & \mathbf{C}_{M-1} & \mathbf{C}_M \\ \mathbf{C}_2 & \mathbf{C}_1 & \mathbf{C}_2 & \dots & \mathbf{C}_{M-1} \\ \vdots & \mathbf{C}_2 & \ddots & \ddots & \vdots \\ \mathbf{C}_{M-1} & \ddots & \ddots & \mathbf{C}_1 & \mathbf{C}_2 \\ \mathbf{C}_M & \mathbf{C}_{M-1} & \dots & \mathbf{C}_2 & \mathbf{C}_1 \end{pmatrix} \quad (2.8)$$

where $\mathbf{C}^{URA}$ is an $MN \times MN$ matrix for $M \times N$ array in 2-D plane. $\mathbf{C}_m$ is a Toeplitz MC matrix corresponding to the mth subarray for $m = 1, \dots, M$ and $\mathbf{C}_m$ is constructed as

$$\mathbf{C}_m = Toeplitz\{[c_1^{(m)}, c_2^{(m)}, \dots, c_N^{(m)}]\} \quad (2.9)$$

where $c_n^{(m)}$ is the MC coefficient in the mth subarray for $n = 1, \dots, N$ and $Toeplitz\{\cdot\}$ is the Toeplitz operation.

2.1.4 Randomly Placed Array

In a randomly placed array (RPA), antennas are arbitrarily placed in 2-D plane as shown in Fig. 2.5. Unlike the above array geometries which have uniform structures, an RPA has no uniform structure. Therefore the MC matrix does not have a special
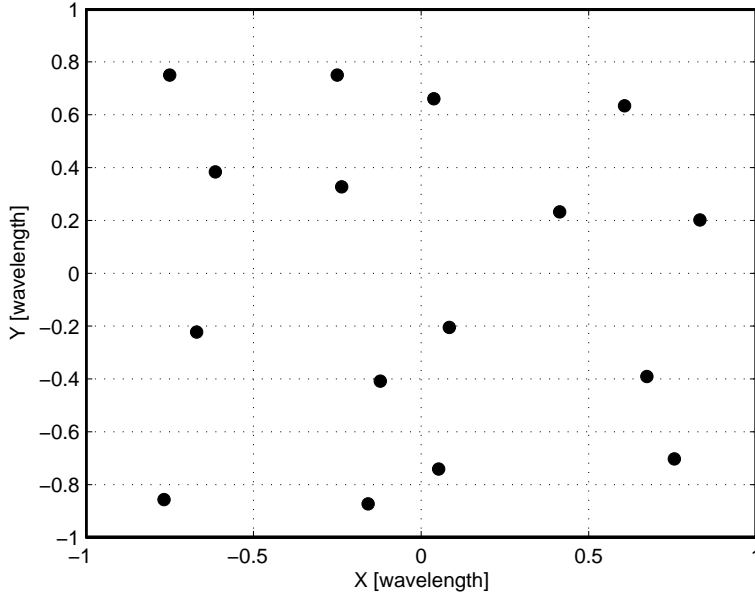
Figure 2.5: The placement of $M = 16$ antennas in a randomly placed array.

form except symmetry [25]. The form of the MC matrix for an RPA is given as

$$\mathbf{C}^{RPA} = \begin{pmatrix} c_{1,1} & c_{1,2} & c_{1,3} & \cdots & & c_{1,M} \\ c_{2,1} & c_{2,2} & c_{2,3} & \cdots & & c_{2,M} \\ c_{3,1} & c_{3,2} & \ddots & \ddots & & \vdots \\ \vdots & \ddots & \ddots & c_{M-1,M-1} & c_{M-1,M} \\ c_{M,1} & c_{M,2} & \cdots & c_{M,M-1} & c_{M,M} \end{pmatrix} \quad (2.10)$$

where $c_{i,j} = c_{j,i}$ is the MC coefficient between the $(i,j)^{th}$ antenna pair in the array for $i, j = 1, \ldots, M$.

2.2 Gain/Phase Mismatches

Antenna arrays use radio frequency (RF) chains to receive signals and downconvert to baseband. These RF chains for different antennas have different gain and phase mismatch contributions for the received signal. Furthermore, each antenna has a different gain and phase for a given DOA. Another cause of mismatch is the differences in the electronic circuitry of the antennas and the receiving media such as cables. Cables with different lengths and materials introduce additional gain and phase mismatches. A DF processor should equalize these gain/phase mismatches in order to estimate

14

DOA angles with a sufficient accuracy.

While the structure of the MC matrix changes for different array geometries, a gain/phase mismatch matrix is usually represented by a diagonal matrix as follows [6]

$$
\boldsymbol{\Gamma} = \begin{pmatrix} \gamma_1 & 0 & \dots & 0 \\ 0 & \gamma_2 & \ddots & \vdots \\ \vdots & \ddots & \ddots & 0 \\ 0 & \dots & 0 & \gamma_M \end{pmatrix} \tag{2.11}
$$

where $\{\gamma_m\}_{m=1}^M$ are the mismatch parameters for M-element array.

2.3 Model Mismatches of Near-field Signals

In most of the DF applications, it is assumed that the transmitter source is located in the far-field of the antenna arrays [11, 65]. While this assumption is usually true for DF applications, reflections in the near vicinity of the array are also received [33,66,67]. The array model of these reflections differs from the far-field array model as the distance of these reflections get closer to the array. This scenario is depicted in Fig. 2.6 where the electromagnetic (EM) field radiation of sources located in the near- and far-field of the antenna array is given. As it is seen, when the source is in the near-field, where the transmitter range satisfies $d < \frac{2D^2}{\lambda}$ where D is the array aperture and λ is the wavelength, the EM fields received by the array are spherical or curved. As these fields travel out from the source (i.e., $d > \frac{2D^2}{\lambda}$), rounding becomes less and the shape turns into more planar. Therefore, the antenna array receives planar waves when the source is in the far-field.

In order to investigate the difference between two array models, a computer simulation is done. For this purpose, an 8-element uniform linear array composed of identical antennas with half-wavelength spacing is considered as shown in Fig. 2.7. A transmitter antenna is located with distance r from the array with the azimuth and elevation angle $\phi = 50°$ and $\theta = 90°$ respectively. The operating frequency is $f = 30\text{MHz}$ and the corresponding wavelength is $\lambda = 10\text{m}$. Note that all the antennas have isotropic antenna pattern. The far-field steering vector is calculated using
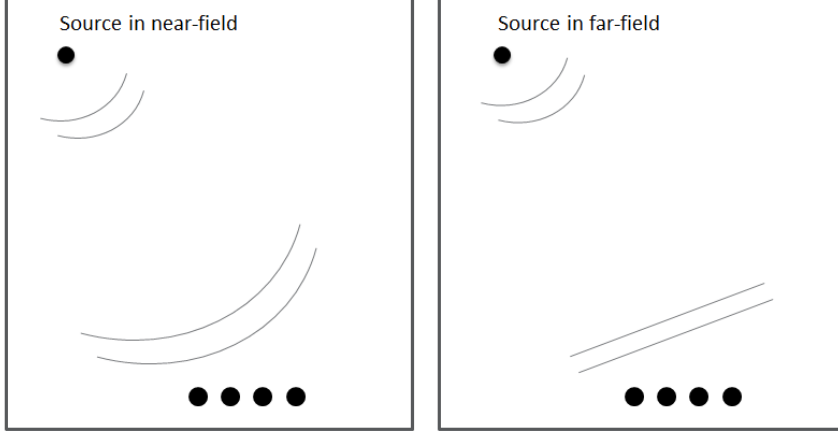
Figure 2.6: Electromagnetic radiation of a source located in the near-field (left) where the range of the transmitter source $d < \frac{2D^2}{\lambda}$ and far-field (right) of the antenna array (i.e., $d > \frac{2D^2}{\lambda}$). D is the array aperture.
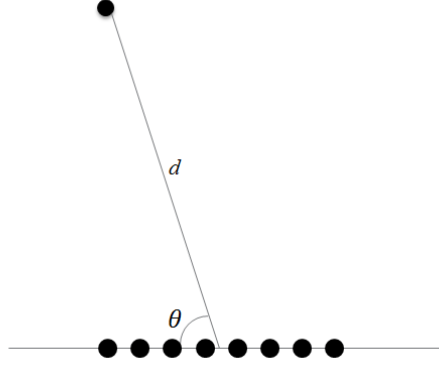
Figure 2.7: Placement of an $M = 8$ antennas in a uniform linear array.

the far-field array model as

$$\mathbf{a}^{FAR}(\Theta) = [a_1^{FAR}(\Theta), a_2^{FAR}(\Theta), \dots, a_M^{FAR}(\Theta)]^T \tag{2.12}$$

where

$$a_m^{FAR}(\Theta) = \exp\left\{ j\frac{2\pi}{\lambda}\mathbf{r}^T\mathbf{p}_m \right\} \tag{2.13}$$

where $\mathbf{r} = [\cos(\phi)\sin(\theta) \ \sin(\phi)\sin(\theta) \ \cos(\theta)]^T$ and $\mathbf{p}_m = [x_m \ y_m \ z_m]^T$ is the mth antenna position. The near-field steering vector is calculated as [28]

$$\mathbf{a}^{NEAR}(\Theta, d) = [a_1^{NEAR}(\Theta, d), a_2^{NEAR}(\Theta, d), \dots, a_M^{NEAR}(\Theta, d)]^T \tag{2.14}$$

where

$$a_m^{NEAR}(\Theta, d) = \exp\left\{ -j\frac{2\pi}{\lambda}d\left(\sqrt{1 - \frac{2}{d}\mathbf{r}^T\mathbf{p}_m + \frac{\mathbf{p}_m^T\mathbf{p}_m}{d^2}} - 1 \right) \right\}. \tag{2.15}$$

16

Then the norm of the difference of steering vectors (i.e., $||\mathbf{a}^{FAR}(\Theta) - \mathbf{a}^{NEAR}(\Theta, d)||_2$) is calculated for different d values and the result is presented in Fig. 2.8. The figure shows the difference between the near- and far-field models as a function of the range of the transmitter. The dashed line is $\frac{2D^2}{\lambda}$ where D is the array aperture. As it is seen, the difference decreases as the range of the source increases. In this case, the near-field model converges to the far-field model as expected. For small values of d where the source is located in the near-field of the array, the difference is large so that there is a mismatch between two array models.
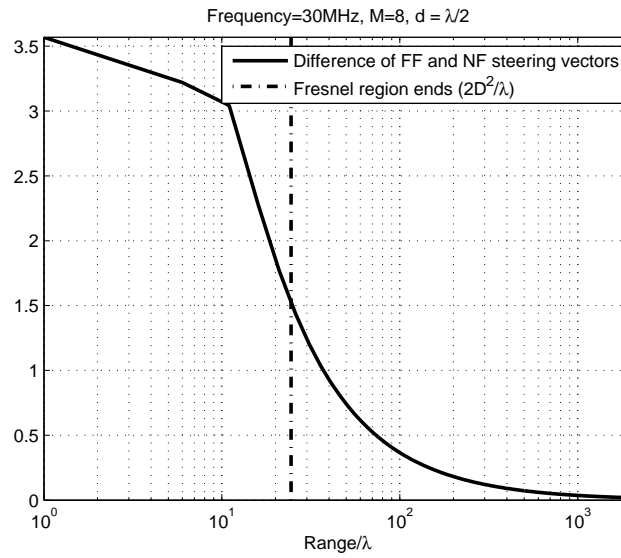
Figure 2.8: Difference between near- and far-field array models versus the range of the transmitter source.

The effect of model mismatch increases as the operating frequency decreases since the range of near-field region is frequency dependent. Therefore model mismatch is mostly effective for low frequencies such as HF (3-30MHz) band for practical applications. In an HF DF scenario, there is usually a source together with its reflections [65]. These reflections are observed in the near-field of the antenna array. In this region, the angular field distribution of the antenna array depends on the range of these reflections, whereas in the far-field model, the shape of the antenna array pattern is independent of the distance between the source and the receive array. Therefore this distance should be taken into account to model the received signals accurately.
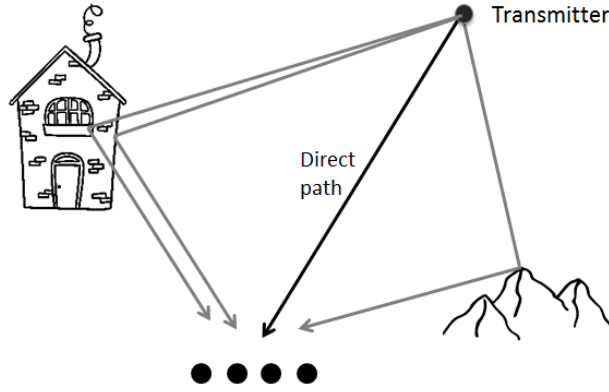
Figure 2.9: A multipath scenario where the transmitter signals is received from different paths.

2.4 Multipath

In DF applications, a source signal is usually reflected from the surfaces in the transmission path (e.g. hills, buildings, etc.) as shown in Fig. 2.9. In this case, the original signal and the reflected signal are received by the antenna array with different directions. In this case, the array covariance matrix becomes singular. As an example, consider the multipath scenario where the output of an array for narrowband model [11] is given as

$$\mathbf{y}(t_i) = \mathbf{A}(\Theta)\mathbf{s}(t_i) + \mathbf{e}(t_i), \qquad i = 1, \ldots, T \tag{2.16}$$

where $\mathbf{A}(\Theta) = [\mathbf{a}(\Theta_1), \mathbf{a}(\Theta_2)]$ is the array steering matrix for two signal paths from different directions. $\mathbf{s}(t_i) = [s_1(t_i), s_2(t_i)]^T$ is a 2×1 vector composed of coherently received source signals and $s_2(t_i) = \alpha s_1(t_i)$ where $\alpha = e^{j\varphi}$ represents the delay between $s_1(t_i)$ and $s_2(t_i)$. Then the array covariance matrix becomes

$$\mathbf{R}_y = \frac{1}{T}\sum_{i=1}^{T} \mathbf{y}(t_i)\mathbf{y}^H(t_i) = \mathbf{A}(\Theta)\mathbf{R}_s\mathbf{A}^H(\Theta) + \mathbf{R}_e \tag{2.17}$$

where $\mathbf{R}_s$ is the signal covariance matrix and rank$\{\mathbf{R}_s\} = 1$ while there are K source DOA angles to be estimated. Due to the rank-deficiency of array covariance matrix, the eigenstructure-based algorithm such as MUSIC [3] and ESPRIT [41] fail to determine the DOA's of K sources. Therefore, multipath is one of the major error sources in DF applications.

CHAPTER 3

CALIBRATION OF ANTENNA ARRAYS FOR AERONAUTICAL VEHICLES ON GROUND

Antenna arrays mounted on platforms require calibration in order to function appropriately. In this chapter, a new method for the calibration of a DF array mounted in front of a UH-60 helicopter is presented. The proposed method is advantageous for its accuracy, simplicity and cost effectiveness.

3.1 Introduction

Calibration of antennas mounted on aircrafts is a challenging task. Antenna arrays for direction finding (DF) are usually designed and tested in isolated environments such as the anechoic chambers [68]. When these arrays are placed on platforms like UAVs (Unmanned Aerial Vehicle), planes or helicopters, scattering, reflection and diffraction from the platform change the response of the antenna array for the incoming source signal [69]. Therefore antenna array should be calibrated while it is mounted on the platform. This task is a nontrivial, time consuming, sensitive and costly process. The motivation of this study is to propose a method to simplify this procedure decreasing the cost and time duration as well as increasing the accuracy.

There are two major ways of calibration for the antenna arrays mounted on aeronautical platforms. In the first approach, calibration is performed when the platform is on the air [56] flying over a predetermined course. The standard approach for on-the-air calibration is to fly the vehicle in a circle above a transmitting antenna with a low depression angle and collect the calibration data for every five degrees and for a

range of frequencies. This process has several limitations since the airplane cannot keep a steady depression angle and flying course due to several factors such as meteorological conditions and dynamics of the flight. This is also a very costly and time consuming process.

The second approach for calibration is to use an anechoic chamber where the aircraft is placed together with a transmitting antenna positioned away from the aircraft as far as possible [68]. This approach has also serious limitations. It is costly and difficult to build such an anechoic chamber which should have a large volume to take an aircraft inside. In fact, there are only a few examples of such chambers. Furthermore, these sites cannot be used for accurate characterization of platform effects on the antenna array especially for low frequencies. An alternative to anechoic chamber is to use an open field [70]. In this case, there are strong multipaths from the ground plane. Electromagnetic absorbers can be used to decrease ground reflections [71]. This also has limitations since absorbers designed for a large frequency span (i.e. 50MHz-1GHz) are difficult to construct and they are costly.

An alternative approach to inside the anechoic chamber calibration is to use a scaled mock-up for the aircraft and install the antenna array on this structure [72]. This approach has certain limitations as well. The antenna array mounted to the mock-up should also be scaled appropriately and manufactured with high precision. Otherwise, the measurements do not completely reflect the practical case. One of the most convenient and cost effective analysis technique for installed antenna performance prediction is to use numerical electromagnetic simulation tools [73].

Calibration of antenna arrays for direction finding purpose is investigated for airborne platforms in the literature. The performance of the DF antennas is investigated in [57] and [58] without considering the multipath from the ground which causes large errors. In [57], DF performance is evaluated for antenna array mounted on a UAV. In [58], calibration is directly performed by using the comparison of the measured data and the simulation results which include the platform effects and mutual coupling. Ground reflection is an important source of error in calibration. The effect of ground plane is investigated in [74] for monopole antenna arrays.

In this part of the thesis, a new method is proposed to calibrate the DF antenna ar-

rays on ground for the aeronautical vehicles. Ground reflections are removed from the calibration data using a time-gating approach. While time-gating is a well-known method for antenna measurements [75], it has not been used for DF array calibration mounted on aeronautical vehicles before. Calibration process is implemented on a facility where the vehicle is elevated over the ground plane and the transmitting antenna is placed on an appropriate distance from the vehicle. The selection of this distance and vehicle height becomes important factors as it is expressed in the following parts of this chapter. The main problem of over-the-ground calibration is the ground reflections. These reflections alter the received signal significantly and the collected data is usually useless without appropriate corrections. When time-gating method is used, reflection-free calibration data is obtained for direction finding. The proposed method is evaluated using a numerical electromagnetic simulation tool, FEKO [76] where a DF array mounted on a UH-60 helicopter is considered. The platform effects are considered and a composite calibration matrix is used for direction finding. The results show that the proposed approach is very effective. It presents several advantages compared to previous approaches. The cost of the proposed approach is significantly lower since the method is performed in an open field. The size of the aircraft does not pose a major problem in general. The time and manual labor involved is lower than the alternatives especially over-the-air calibration. The method also allows the correct characterization of platform effects on the DF array since the transmit antenna can be positioned at a large distance. The method is essentially performed in time and the calibration data for any frequency can be obtained easily. Overall accuracy of the method is good which leads to an effective calibration technique in practice.

3.2 Test Setup and The Problem Description

In this chapter, offline calibration of a DF antenna array mounted on an aeronautical vehicle is considered. More specifically, a UH-60 helicopter is selected as the platform. A four element dipole antenna array is mounted in front of the helicopter as shown in Fig. 3.1. The array is a UCA with the antenna and array dimensions are given in Table 3.1. The target is to obtain the calibration data for the antenna array so that the DF algorithms work with good accuracy.
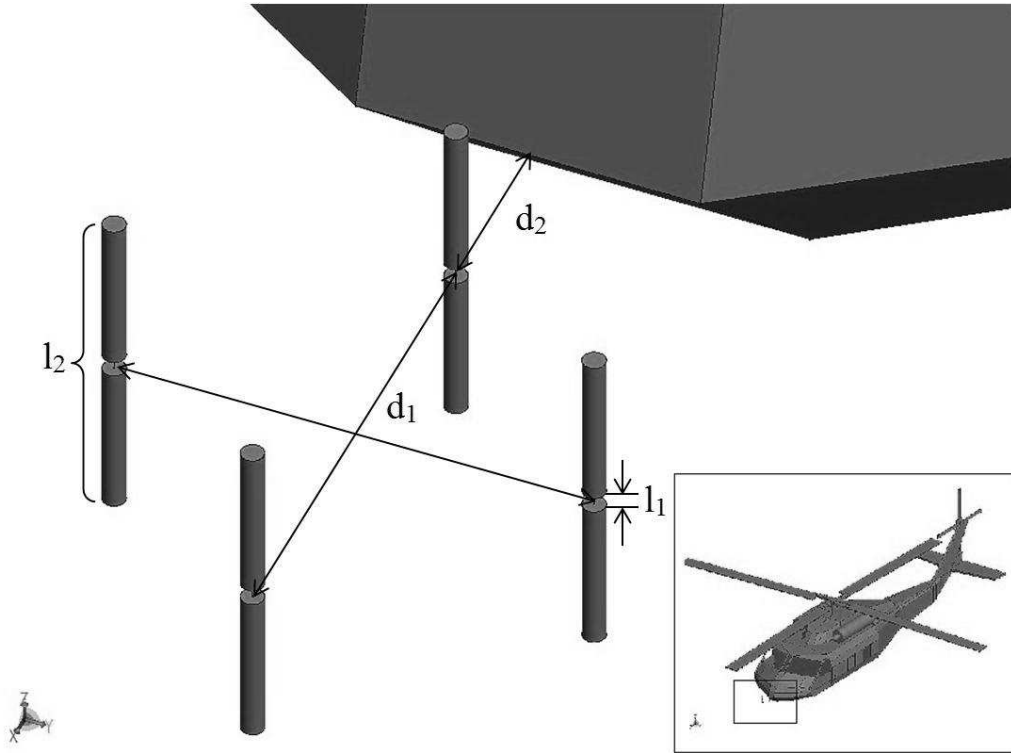
Figure 3.1: The antenna array is composed of four dipoles mounted in front of a UH-60 helicopter.

The open-field test area and the platform placement is shown in Fig. 3.2. Test facility is considered as a 200m × 200m open-field with a flat ground plane. It is assumed that there is no obstacle in the near vicinity of the test field which may cause additional disturbances. The helicopter is elevated above the ground and flipped upside down so that a similar condition for a source emitting from the ground to the airborne vehicle is generated. The transmitting antenna is elevated to a height so that sufficient elevation for the calibration is obtained. The transmit antenna is identical to the array antennas and the parameters for the test field are given in Table 3.2.

Table 3.1: Antenna array dimensions.

Array diameter	d_1	0.4242m
Distance from the platform	d_2	0.1m
Gap for the dipole	l_1	0.05m
Length of the dipole	l_2	0.3m
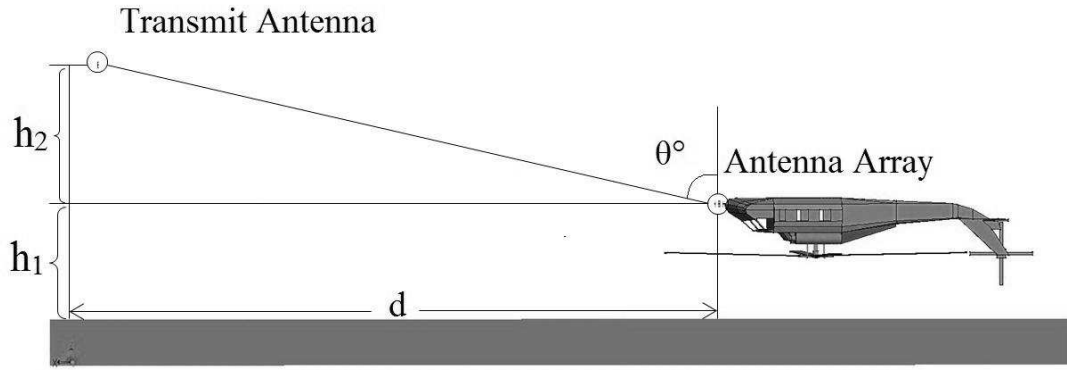
Figure 3.2: The open-field test area and platform placement.

Table 3.2: Calibration and test setup parameters.

Height of the helicopter over the ground	h_1	16m
Height of the transmitter	h_2	24m
Horizontal distance of transmitter	d	100m
Elevation angle	θ	76.5°

3.2.1 Problem Description and The Model

The problem is the calibration of the DF system mounted on a UH-60 helicopter as shown in Fig. 3.1 and Fig. 3.2. The MUSIC algorithm [3] is selected as the DF algorithm. It is known that the MUSIC algorithm approaches to the optimum solution asymptotically under ideal conditions [77].

There are two problems that should be solved for a satisfactory DF performance. The first and the most important problem is the ground reflections. Ground reflections corrupt the data collected by the DF antennas. The effect of these reflections decreases as the operating frequency increases. Nevertheless, ground reflections are the major sources of error especially in the VHF/UHF (30MHz-1000MHz) range. The second problem is the multipath components due to the platform as shown in Fig. 3.3. The MUSIC algorithm does not perform well for the antenna arrays mounted on platforms like the one in Fig. 3.3 due to the reflections from the ground and the platform.

In time domain, the output of the ith antenna $y_i(t)$ can be expressed as the convolution of the antenna impulse response and the source signal, i.e.,

$$y_i(t) = h_{i,eff}(p_i, t, \Theta) * x(t - \tau_i) + e_i(t) \qquad (3.1)$$
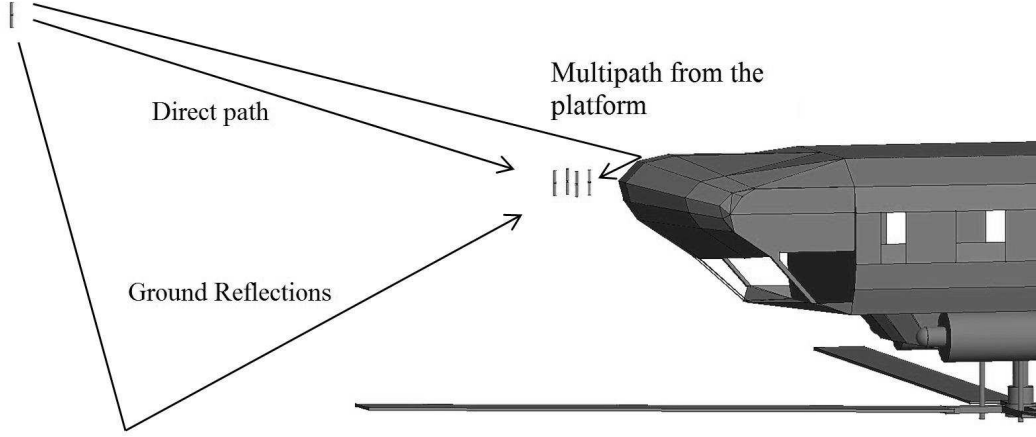
Figure 3.3: Direct path and the reflections from the ground and the platform.

where $p_i = (x_i, y_i, z_i)$ is the position of the ith antenna and the DOA of the source is $\Theta = (\phi, \theta)$ where ϕ and θ denotes the azimuth and elevation angles respectively. $x(t) = Re\{s(t)e^{j\omega_c t}\}$ is the source signal, ω_c is the center frequency and $s(t)$ is the complex baseband signal. τ_i is the time delay with respect to a reference point in the coordinate system. $e_i(t)$ is zero-mean spatially and temporarily white Gaussian noise in the ith antenna. In this study, a single source is assumed during the calibration process. For simplicity, the parameters are taken as $\Psi_i = (p_i, t, \Theta)$. The ith antenna impulse response, $h_{i,eff}(\Psi_i)$, for the system in Fig. 3.3 can be written as

$$h_{i,eff}(\Psi_i) = h_{i,c}(\Psi_i) + h_{i,gnd}(\Psi_i). \tag{3.2}$$

Here $h_{i,gnd}(\Psi_i)$ is the component due to ground reflections and $h_{i,c}(\Psi_i)$ is the desired component which includes the platform effects. When (3.1) and (3.2) are combined, i.e.,

$$y_i(t) = y_{i,direct}(t) + y_{i,gnd}(t) + e_i(t) \tag{3.3}$$

is obtained, where

$$y_{i,direct}(t) = h_{i,c}(\Psi_i) * x(t - \tau_i) \tag{3.4}$$

$$y_{i,gnd}(t) = h_{i,gnd}(\Psi_i) * x(t - \tau_i)$$

If $y_{i,direct}(t)$ and $y_{i,gnd}(t)$ do not overlap in time, they can be effectively separated in time domain by time-gating. In order to separate the ground reflections from the desired component, test field parameters in Table 3.2 and Fig. 3.2 should be selected appropriately. As the distance between the transmit antenna and the platform, d, increases, $y_{i,direct}(t)$ and $y_{i,gnd}(t)$ start to overlap in time. This is due to the fact that

24

the path length difference between the ground and direct path decreases. Therefore ground and direct path waves reach to the antenna array about the same time. Fig. 3.4a shows the path length difference as h_1 and d change when $h_2 = 24m$ is fixed. Fig. 3.4b is obtained by changing h_2 and d when $h_1 = 16m$. The effect of h_1 and h_2 on the path length difference is seen in Fig. 3.4c when $d = 100m$. As it is seen from these figures, path length difference increases as h_1 and h_2 increase. d is desired to be small for a better time separation. On the other hand, multipath effects due to the platform change as the transmitter approaches to the platform. Therefore the transmitter is desired to be as far away as possible from the platform to obtain calibration data corresponding to a far-field transmitting source. This trade-off can be solved with a trial and error approach since an analytical expression cannot be found for such a complex scenario. The parameters for the calibration setup are shown in Fig. 3.2 and the parameter vector is $\mathbf{q} = [h_1, h_2, d, \theta]^T$. In order to select suitable values for these parameters, θ is fixed initially. Then h_1 is selected by considering the practical conditions such as the size of the platform. h_2 is chosen similarly for the transmit antenna by considering the possible antenna tower height and elevation angle. A trial and error approach is considered using numerical electromagnetic simulations and suitable d value is selected such that the direct path and the multipath signal from ground do not overlap. Table 3.2 shows the set of suitable test field parameters obtained in this work using the above procedure.

Once the ground reflections in (3.2) are eliminated, the array output can be written in Fourier Domain using the narrowband model [11], i.e.,

$$\mathbf{Y}(\omega) = \mathbf{M}(\omega, \Theta)\mathbf{a}(\omega, \Theta)\mathbf{S}(\omega) + \mathbf{E}(\omega) \tag{3.5}$$

where $\mathbf{Y}(\omega) = [\ Y_1(\omega)\ \ Y_2(\omega)\ \ \cdots\ \ Y_M(\omega)\ ]^T$, $\mathbf{S}(\omega)$ is the baseband source spectrum and M is the number of antennas. $\mathbf{a}(\omega, \Theta) = [\ a_1(\omega, \Theta)\ \ \cdots\ \ a_M(\omega, \Theta))\ ]^T$ is the nominal steering vector composed of a single source component, i.e.,

$$a_i(\omega, \Theta) = \exp\left\{ j\frac{2\pi}{\lambda(\omega)}\mathbf{r}^T\mathbf{p_i} \right\} \qquad i = 1, 2, \dots, M \tag{3.6}$$

where $\lambda(\omega)$ is the wavelength at frequency ω, $\mathbf{r} = [\cos\phi\sin\theta, \sin\phi\sin\theta, \cos\theta]^T$ and $\mathbf{p}_i = [x_i, y_i, z_i]^T$ is the antenna positions. $\mathbf{M}(\omega, \Theta)$ is a composite matrix defined as

$$\mathbf{M}(\omega, \Theta) = \mathbf{C}(\omega)\mathbf{\Gamma}(\omega, \Theta) \tag{3.7}$$

25
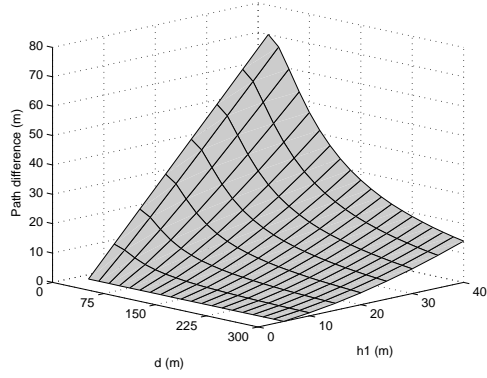
(a)
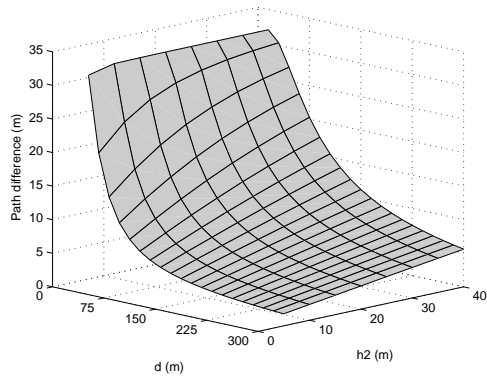
(b)
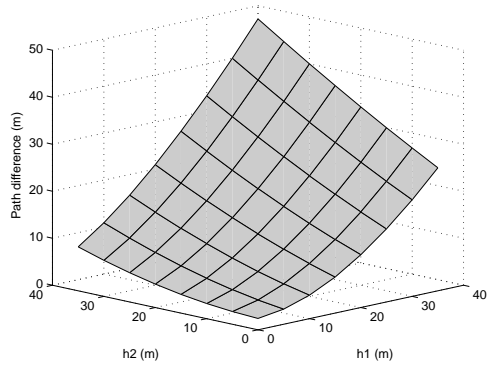
(c)

Figure 3.4: Path length difference variation for (a) h_1 and d are changed ($h_2 = 24m$), (b) h_2 and d are changed ($h_1 = 16m$), (c) h_1 and h_2 are changed ($d = 100m$).

where $\mathbf{C}(\omega)$ is the direction independent $M \times M$ mutual coupling matrix (MCM). $\mathbf{\Gamma}(\omega, \Theta)$ is a diagonal matrix which is both frequency and direction dependent. Note that $\mathbf{\Gamma}(\omega, \Theta)$ includes the channel effects [11]. While $\mathbf{\Gamma}(\omega, \Theta)$ is different for different Θ directions, it can be assumed to remain approximately the same for small angular

26

sectors covering the range of angles between $(\phi - \phi_\epsilon, \theta - \theta_\epsilon)$ and $(\phi + \phi_\epsilon, \theta + \theta_\epsilon)$ where $(\phi_\epsilon \; \theta_\epsilon)$ defines the sector extension. Once the ground reflections are eliminated and mutual coupling is removed, the actual steering vector $\bar{\mathbf{a}}(\omega, \Theta)$ and the nominal steering vector $\mathbf{a}(\omega, \Theta)$ are related as

$$\bar{\mathbf{a}}(\omega, \Theta) = \mathbf{\Gamma}(\omega, \Theta)\mathbf{a}(\omega, \Theta) \qquad (3.8)$$

$$\mathbf{\Gamma}(\omega, \Theta) = diag(\gamma_1, \gamma_2, \ldots, \gamma_M). \qquad (3.9)$$

Then, the ith element of this diagonal matrix is obtained from the ith element of the steering vectors as

$$\gamma_i = \frac{\bar{a}_i(\omega, \Theta)}{a_i(\omega, \Theta)} \qquad (3.10)$$

The calibration for the MUSIC algorithm requires both $\mathbf{C}(\omega)$ and $\mathbf{\Gamma}(\omega, \Theta)$. The MCM, $\mathbf{C}(\omega)$, is found for each frequency using the method described in [78] before the array is mounted on the platform.

3.2.2 Mutual Coupling Matrix

Mutual coupling among the antennas in the array causes a DF error. Moreover this error is frequency dependent and should be corrected for the operating frequency. MCM is found for the frequency range of $f \in [150MHz - 450MHz]$. Mutual coupling matrix for a UCA composed of identical antennas is direction independent and has circulant structure. As it is described in [78], mutual coupling matrix can be found easily by using a system theoretic approach where the coupled voltages are mapped to the uncoupled voltages through the inverse of MCM. MCM is found independent of the platform effects when the array is placed on an idealistic environment such as an anechoic chamber. In our case, FEKO and numerical electromagnetic simulations are used to collect the data and compute the MCM. The coupled and the uncoupled voltages are measured. The coupled voltages are obtained by using a single plane wave source placed in $\Theta_k = (\phi_k, 90°)$ where ϕ_k changes between 0 and 350 degrees in 10 degrees resolution while all the antennas in the array do exist. The uncoupled voltages are obtained by considering the antennas one-by-one separately while all the other antennas are removed for the same plane wave source. The coupled voltages

for $K = 36$ measurement directions $\{\Theta_k\}_{k=1}^{K}$ are stacked in the matrix $\mathbf{V}_c$ as

$$\mathbf{V}_c(\omega) = [\ \mathbf{v}_c(\omega, \Theta_1) \quad \mathbf{v}_c(\omega, \Theta_2) \quad \dots \quad \mathbf{v}_c(\omega, \Theta_K) \ ] \tag{3.11}$$

where

$$\mathbf{v}_c(\omega, \Theta_k) = [\ v_1^c(\omega, \Theta_k) \quad v_2^c(\omega, \Theta_k) \quad \dots \quad v_M^c(\omega, \Theta_k) \ ]^T \tag{3.12}$$

and the uncoupled voltage matrix $\mathbf{V}_{uc}(\omega)$ is obtained as

$$\mathbf{V}_{uc}(\omega) = [\ \mathbf{v}_{uc}(\omega, \Theta_1) \quad \mathbf{v}_{uc}(\omega, \Theta_2) \quad \dots \quad \mathbf{v}_{uc}(\omega, \Theta_K) \ ] \tag{3.13}$$

where

$$\mathbf{v}_{uc}(\omega, \Theta_k) = [\ v_1^{uc}(\omega, \Theta_k) \quad v_2^{uc}(\omega, \Theta_k) \quad \dots \quad v_M^{uc}(\omega, \Theta_k) \ ]^T \tag{3.14}$$

Note that $\{v_m^{uc}(\omega, \Theta_k)\}_{m=1}^{M}$'s are found separately in this process. Then the transformation between the coupled and the uncoupled matrix is obtained by a transformation matrix $\mathbf{T}(\omega)$ as

$$\mathbf{T}(\omega)\mathbf{V}_c(\omega) = \mathbf{V}_{uc}(\omega) \tag{3.15}$$

and the MCM is found as

$$\mathbf{C}(\omega) = \mathbf{T}^{-1}(\omega). \tag{3.16}$$

3.2.3 Sampling in Frequency

The impulse response of a linear time invariant (LTI) system can be found both in time and frequency. In this study, the impulse response of the DF antenna system mounted to a platform is obtained in frequency domain. This is due to the fact that FEKO can perform electromagnetic simulations in frequency more effectively.

Nyquist Sampling Theorem (in frequency) [79]:

Assume that $Y(\omega)$ corresponds to a time-limited signal with

$$y(t) = 0, \quad for \ t \geq T_a \ and \ t < 0 \tag{3.17}$$

Then $Y(\omega)$ can be uniquely determined by its samples

$$Y[k] = Y(k\Delta_\omega), \quad k = 0, 1, \dots, N, \ k \in Z^+ \tag{3.18}$$

if the following condition is satisfied

$$T_s = \frac{2\pi}{\Delta_\omega} \geq T_a \qquad (3.19)$$

A time-limited signal is not bandlimited. Ideally, infinitely many frequency samples are needed for such signals. However similar to time-domain sampling [80], either the signal is assumed to be bandlimited or anti-aliasing filters can be used. Note that any practical antenna impulse response can be assumed to be time-limited [81]. In this study, frequency domain sampling is used in order to obtain the discrete-time impulse response of the DF antenna array mounted on the platform as shown in Fig. 3.1. $N =$2000 uniform samples in frequency are taken. The frequency step is selected as $\Delta_f = 500kHz$ where $\Delta_\omega = 2\pi\Delta_f$. Note that $T_a \leq 2\mu s$ for this case. The samples are taken in $f \in [500kHz, 1GHz]$ range. Limiting the largest frequency of samples f_{max} corresponds to windowing in frequency domain. This is a convolution with a sinc function in time which generates ringing in time waveform. Unfortunately this ringing cannot be corrected after sampling. The best way to deal with it is to select f_{max} sufficiently large. The DC component of the samples at f=0 Hz is not taken for the simulation process since the sample magnitude at this frequency is zero.

Sampling in frequency is realized using FEKO simulations. Transmitting antenna in Fig. 3.2 is positioned at a selected azimuth angle ϕ_i and at a fixed elevation angle $\theta_i = 76.5°$. In our case, we have considered only a single elevation angle for simplicity. Additional elevation angles can be considered for a more detailed calibration procedure. A sinusoidal wave is transmitted with a frequency ω. Here ω is changed uniformly in discrete steps and 2000 samples in 1GHz band are taken. The numerical electromagnetic simulation results for each frequency are recorded for further processing in MATLAB. The recorded data is composed of the complex values of currents observed at each DF antenna for the excitation wave. The current values have contributions due to both ground reflections and multipath components from the platform as well as the direct path as shown in Fig. 3.3.

3.3 Time-Gating Method

Time-gating is a well-known approach in different fields including antenna measurements [75]. The idea in time-gating is to multiply a time signal with a window in time to extract only the intended part of the signal. Time-gating is used to find the antenna factor [82] and near-field to far-field conversions [83]. In this study, time-gating is applied to remove the ground reflections from the array signals. Transmitted signal should be a pulse with a short duration so that the ground reflection does not overlap with the useful part of the signal in time. Ideally, an impulse will be the best choice. While it is not possible to generate an impulse in continuous-time, Discrete Fourier Transform (DFT) property can be used to obtain discrete-time impulse or unit sample function, i.e.,

$$DFT_N\{\delta[n]\} = 1, \quad \forall \omega_k, \omega_k = \frac{2\pi k}{N} \ k = 1, 2, \ldots, N \tag{3.20}$$

where DFT_N stands for the $N-$point DFT. $\mathbf{S}(\omega) = 1$ is assumed for equation (3.5). Note that when DFT_N and inverse DFT_N are used to relate the time and frequency response, $\Delta_f = 500kHz$ leads to a sampling step of $\Delta_t = \frac{1}{2N\Delta_f} = 0.5ns$ in time domain.

Numerical electromagnetic simulations are performed in FEKO [76] using the Geometrical Optics (GO) approach. The model is built using the real dimensions of a Sikorsky UH-60 helicopter. The ground plane is simulated with a dielectric material which has the loss tangent of 0.04. The simulations are repeated for $f \in[500\text{kHz},$ 1GHz]. At each frequency, transmit antenna is used to transmit a sinusoidal plane wave. The magnitude and the phase of the observed excitation at each element of the UCA are recorded. Therefore the impulse response of the antenna array in (3.1) is obtained in the frequency domain. In order to obtain the time domain samples, $2N-$point inverse DFT is used. This is done by generating the additional $N-$point data in frequency through complex conjugation since DFT of a real signal is conjugate symmetric.

In Fig. 3.5, the magnitude of the currents are shown for different frequencies at each antenna in the array. Note that the DFT of a real signal has conjugate symmetry as shown in Fig. 3.5. Fig. 3.6 shows the time domain waveforms obtained through

the inverse DFT. As it is seen from Fig. 3.6, ground reflections are separate from the useful part of the waveform and time-gating can be used to eliminate the ground reflections. The small amplitude of the ground reflection is due to the attenuation of the reflected wave.

When time-gating is applied, the time domain response in Fig. 3.7 is obtained. The frequency domain responses after time-gating process are given in Fig. 3.8. Once the array output in Fourier domain is obtained as in Fig. 3.8, actual array steering vector $\bar{\mathbf{a}}(\omega, \Theta)$ is constructed by stacking the antenna responses in a vector for a given frequency ω.
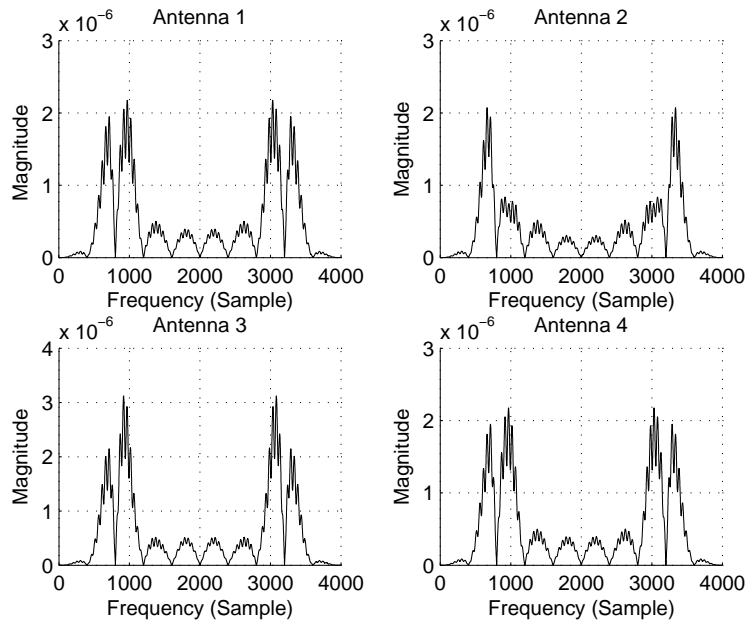
Figure 3.5: The signal waveforms in frequency domain before the time-gating for each antenna for the DOA $(0°, 76.5°)$.

3.4 Calibration Data and DF Test

The steps for the calibration procedure are given in Fig. 3.9. During the calibration procedure, calibration data is collected by turning the transmit antenna around the antenna array and the platform in 360 degrees in the azimuth plane. Usually uniform discrete angular steps are used. The simulations for a single direction Θ_i, take about 10 hours for the selected platform. Therefore, non-uniform angular steps are used

31
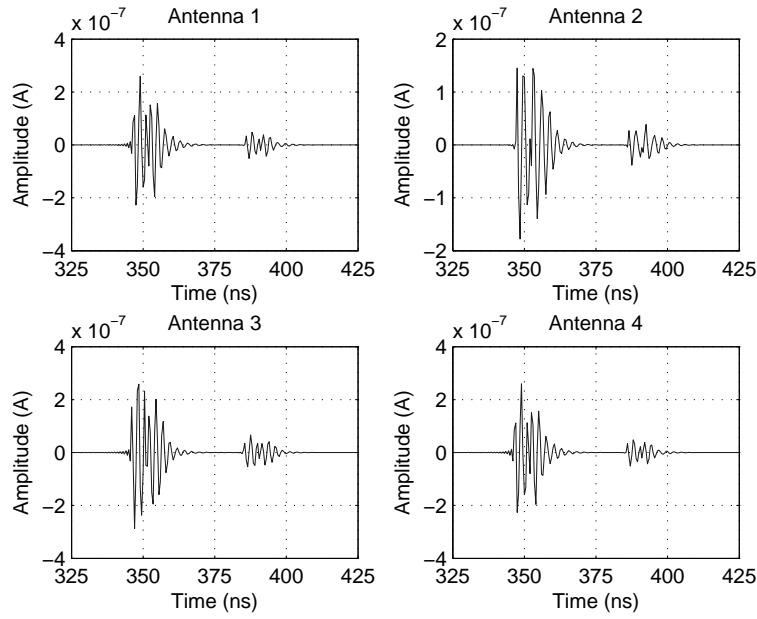
Figure 3.6: The signal waveforms in time domain before the time-gating for each antenna for the DOA $(0°, 76.5°)$.
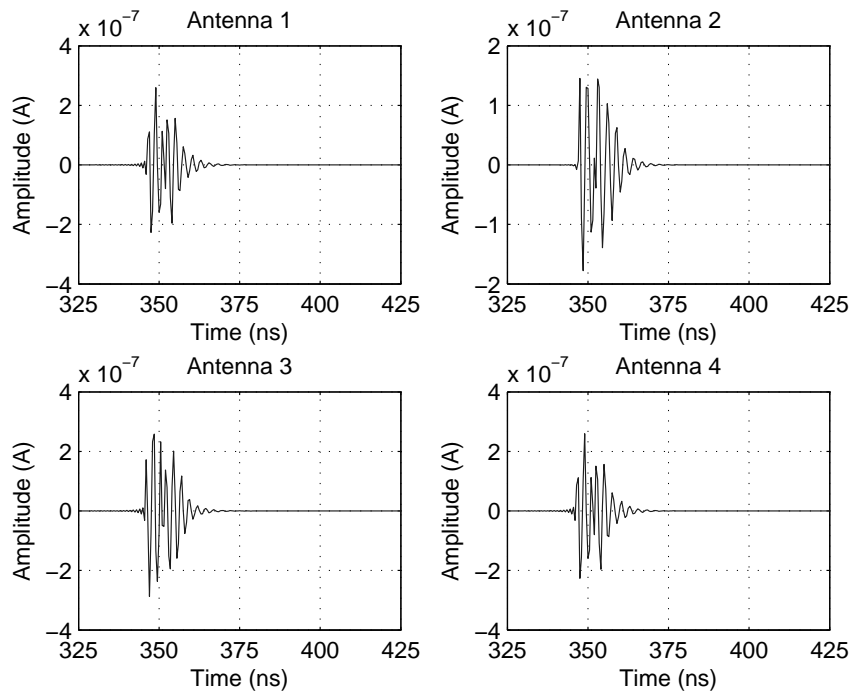
Figure 3.7: The signal waveforms in time domain after the time-gating for each antenna for the DOA $(0°, 76.5°)$.

to decrease the computational load and obtain a reasonably good overall DF performance. There are 36 azimuth angles where the calibration is performed. They are

32
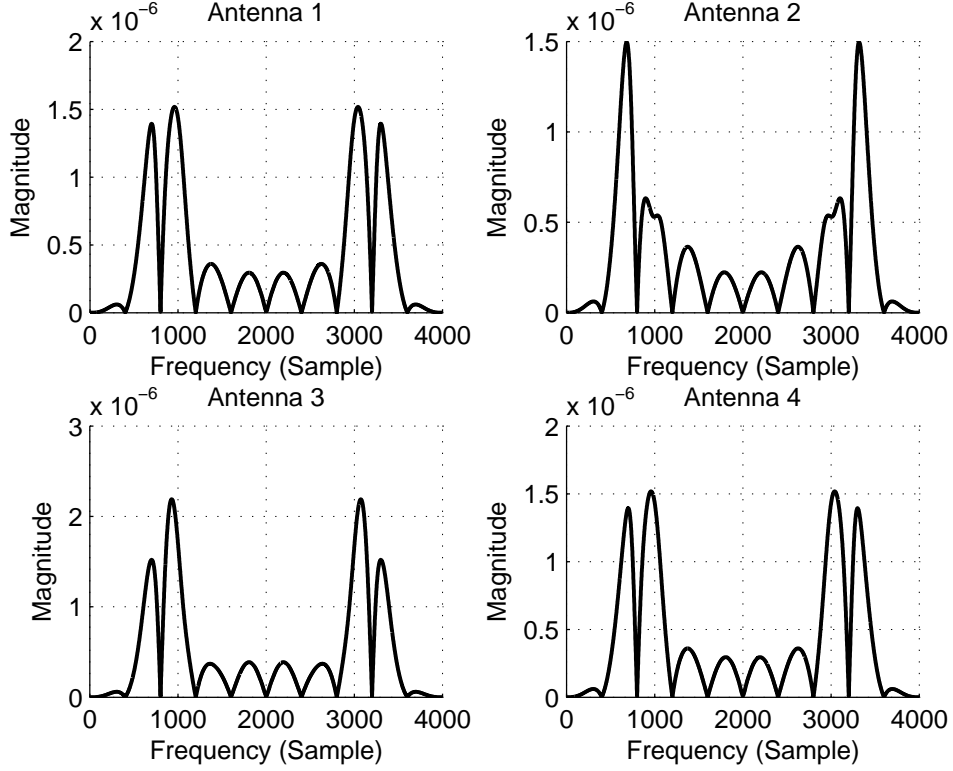
Figure 3.8: The signal waveforms in frequency domain after the time-gating for each antenna for the DOA $(0°, 76.5°)$.

listed in degrees as shown below

$$\phi \in [0\ 3\ 10\ 20\ 40\ 60\ 80\ 88\ 100\ 108\ 114\ 120\ 128\ 134\ 140\ 144\ 150\ 160\ 170\ 180\ 189$$
$$210\ 250\ 263\ 273\ 280\ 290\ 297\ 300\ 307\ 323\ 330\ 335\ 340\ 350\ 359]^{T}.$$

The above calibration angles are selected in an ad-hoc manner to decrease the DF error below 3 degrees. Elevation angle is fixed as $\theta = 76.5°$ as shown in Fig. 3.2. The actual steering vector $\bar{\mathbf{a}}(\omega, \Theta)$ is used to calibrate the corresponding DOA angle Θ as well as its neighborhood such that the average RMS (root mean square) error in the neighborhood of the DOA angle Θ is small. The calibration data is composed of the mutual coupling matrix $\mathbf{C}(\omega)$ and $\mathbf{\Gamma}(\omega, \Theta)$ which are obtained in 3.10 and 3.16.

The test for the evaluation of the calibration process is done as follows. DF array mounted on UH-60 helicopter is modeled in FEKO when the UH-60 is on the air and there is no ground plane. A plane wave with a frequency ω is transmitted from the direction $\Theta_i = (\phi_i, 103.5°)$, $\phi_i \in [0°, 359°]$ and the array response $\mathbf{Y}(\omega)$ is obtained.
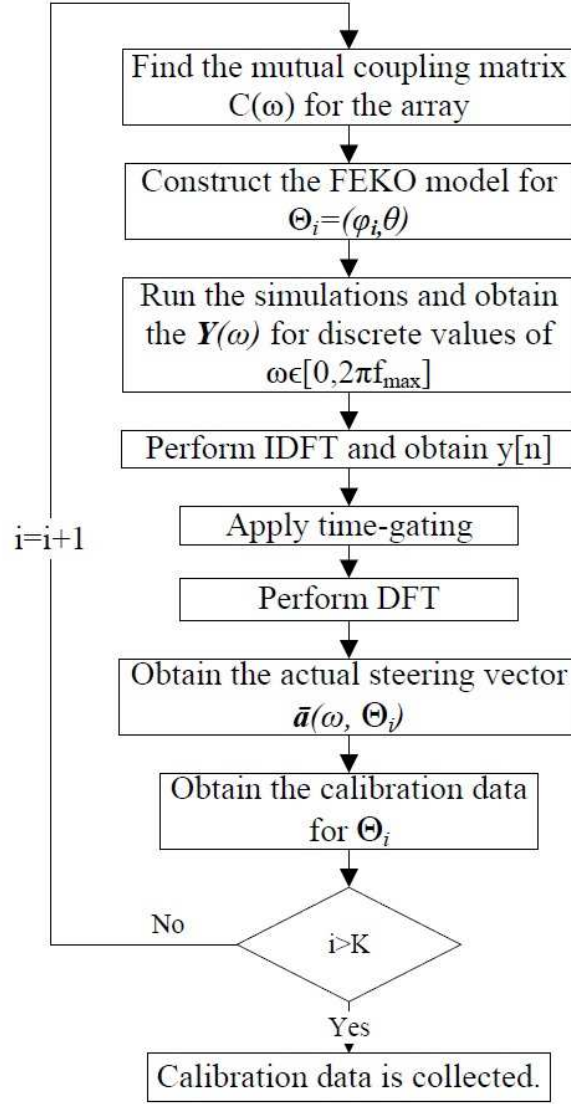
Figure 3.9: The calibration procedure.

The estimate for the composite matrix $\mathbf{M}(\omega, \Theta)$ in (3.7) is obtained as it is described in Sec. 3.2.2. The covariance matrix estimate $\hat{\mathbf{R}} = \mathbf{Y}(\omega)\mathbf{Y}(\omega)^H = \hat{\mathbf{U}}\Lambda\hat{\mathbf{U}}^H$ and the eigenvector matrix $\hat{\mathbf{G}}$ corresponding to the noise subspace eigenvectors is computed [3]. Then the classical MUSIC pseudo-spectrum $P(\Theta_i)$ is evaluated [8] as

$$P(\Theta_i) = \frac{1}{\mathbf{a}^H(\omega, \Theta_i)\mathbf{M}^H(\omega, \Theta_i)\hat{\mathbf{G}}\hat{\mathbf{G}}^H\mathbf{M}(\omega, \Theta_i)\mathbf{a}(\omega, \Theta_i)}. \tag{3.21}$$

The peak in $P(\Theta_i)$ corresponds to the source direction.

3.5 Simulation Results

In this section, DF performance for the proposed offline calibration method is evaluated by using both the MUSIC [3] and correlative interferometer algorithms [84]. Both of the algorithms use the same calibration data. A single source is assumed while the UH-60 is on air. Noise-free observations are used. There is only a single snapshot since FEKO results only a single observation for a given frequency. Note that this is sufficient for a single source scenario. Simulations are performed in MATLAB and both calibrated and uncalibrated DF performances are evaluated.

The test source is placed in $\Theta_i = (\phi_i, 103.5°)$ where ϕ_i is changed between 0 and 359 degrees in one degree resolution. Note that UH-60 is now assumed to be airborne and DF array does see the transmitter with an elevation angle of $\theta = 180° - 76.5° = 103.5°$. The DF performances for different frequency bands are obtained. In Fig. 3.10, the azimuth DOA performance for 150MHz is shown when the helicopter is on the air and there is no calibration. This figure shows the importance of the platform effects. The DF performance is poor since the antenna array response changes when the array is mounted on a platform like the UH-60 helicopter. Therefore, calibration should take into account the platform effects.

In Fig. 3.11a and Fig 3.11b, the DOA estimation results are presented for 150MHz and 450MHz respectively when the proposed calibration technique is applied. Note that while the calibration data is generated when UH-60 is over the ground, test data is obtained when the helicopter is on the air. The calibration angles are given in Sec. 3.4. CAL-MUSIC and CAL-CI are the calibrated MUSIC and correlative interferometer algorithms respectively. NO CAL-MUSIC corresponds to the direct application of the MUSIC algorithm without calibration. As it is seen from this figure, the performance of the proposed approach at the calibration angles is very good which means that the ground reflections are eliminated effectively and the platform effects are calibrated appropriately. Correlative interferometer has slightly worse performance. Even though there is interpolation between the calibration points, the calibration data is not sufficient to model the nearby angular characteristics for the interferometer algorithm. The direct application of the MUSIC algorithm without calibration results very large errors. The estimation errors are not symmetric with respect to zero degrees
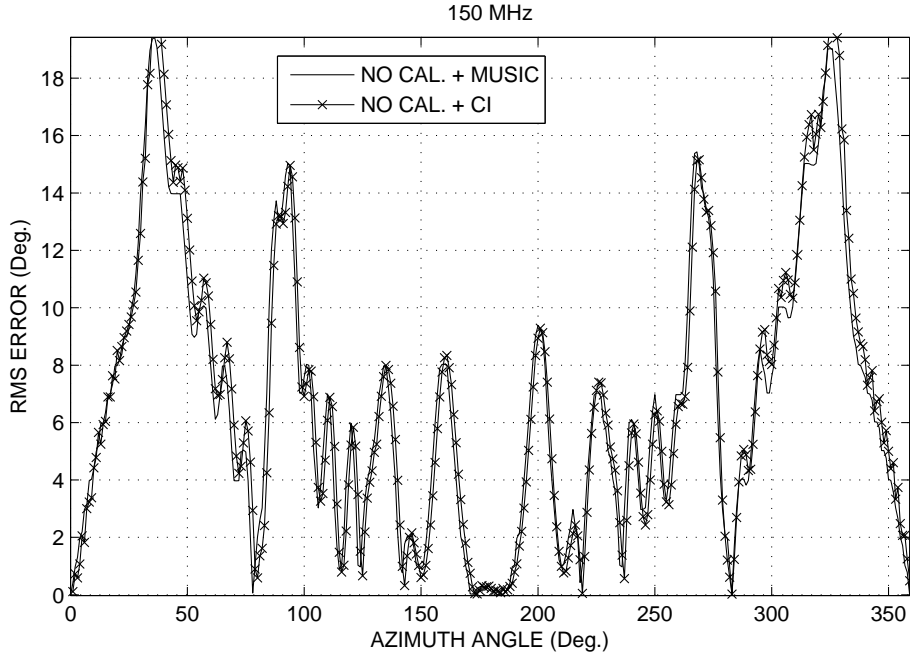
Figure 3.10: The effect of helicopter platform on the azimuth DOA performance at 150 MHz when the aircraft is positioned on air with no ground reflections. There is no calibration for the platform effects. Elevation angle is $\theta = 103.5°$.

which corresponds to the bore-sight or nose of the helicopter. This is due to the fact that UH-60 is not symmetric and its tail blades generate an asymmetry. Therefore, calibration data should be collected in 360 degrees for a better DF performance.

3.6 The advantages of The Proposed Calibration Technique

The advantages of the proposed calibration technique are as follows:

- The proposed method is implemented when the vehicle is on the ground and it does not require anechoic chambers or radiation absorbing materials. Therefore, it is not costly.

- Accurate calibration data can be obtained since the vehicle and the transmitter antenna are steady during the calibration process.

- Since the calibration data is obtained in time domain, it can be used for a large range of frequencies. This reduces the labor and time.

36

150MHz

(a)
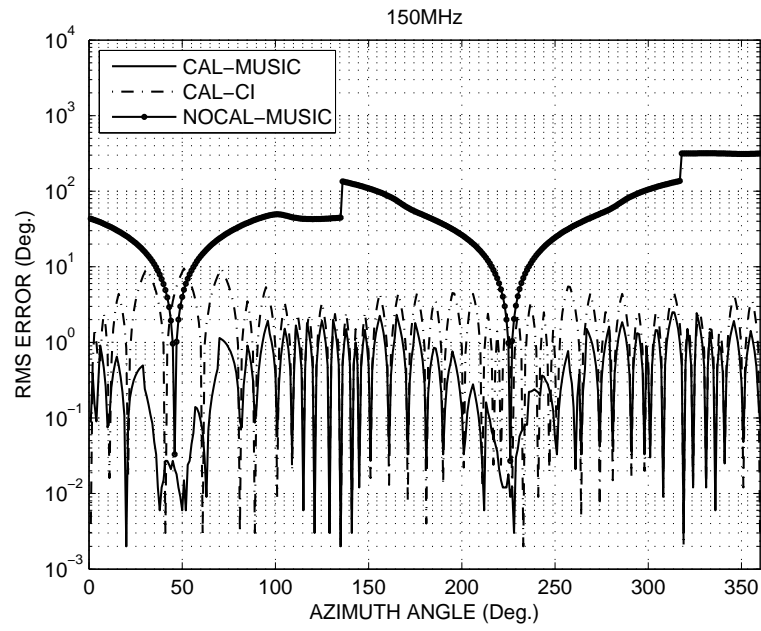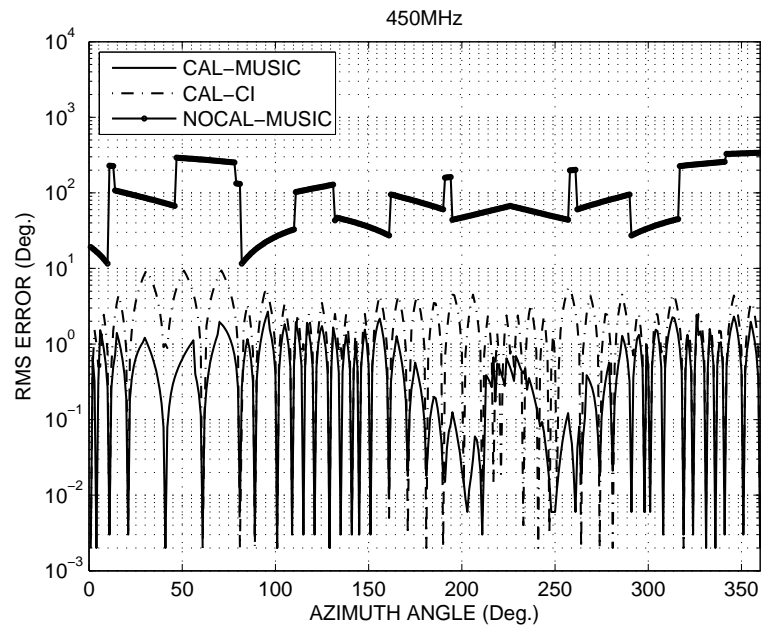
450MHz

(b)

Figure 3.11: Proposed calibration technique is applied when the UH-60 is on the ground. Azimuth DOA performance at 150 MHz (a) and 450MHz (b), $\theta = 103.5°$.

CHAPTER 4

FAR-FIELD DOA ESTIMATION AND NEAR-FIELD LOCALIZATION FOR MULTIPATH SIGNALS

In practical direction-finding (DF) applications, multipath signals are important source of error for parameter estimation. When the antenna arrays receive multipath reflections which are coherent with the far-field line-of-sight signal, estimating the far- and near-field components becomes an important problem. In this chapter, a new method is proposed to estimate the direction-of-arrival (DOA) of the far-field source and to localize its near-field multipaths.

4.1 Introduction

Multipath distortion is the main source of error in many applications including direction finding (DF). While error sources like gain/phase mismatch [2], mutual coupling [78] between antennas also have an impact on the DF accuracy, multipath results in gross errors. Multipath components of a far-field source are generated by reflection, diffraction and scattering in the region between the transmitter and receiving antenna array. Far-field multipath components are observed from the structures close to the transmitter. When the distance between the transmitter and DF array is large, the contribution of these components to DF error is limited. Hence gross errors are observed mostly due to the near-field multipath components.

In this study, DOA estimation problem is considered for a single far-field source with its near-field multipath reflections. In the literature, there are several works on the localization of the mixed far- and near-field sources. Most of these studies use the

39

assumption of independent source signals. However this assumption is not valid in practical applications [34–38]. Another disadvantages of these methods is that they use an approximate near-field model [66, 67] which deviates significantly from the exact near-field model as the range becomes smaller (e.g. $< 0.62\sqrt{\frac{D^3}{\lambda}}$ where D is the array aperture). In this study, exact near-field model is employed in order to model the near-field multipaths more accurately and a new method is proposed for direction finding and localization. The proposed method finds the 2-D DOA angles for the far-field source and azimuth and range estimates for the near-field sources. Far-field source DOA estimate is found using calibration and the MUSIC algorithm. In a scenario where the DF array is placed in an arbitrary and irregular terrain, calibration is essential for parameter estimation where some of the unknowns are direction dependent. The need for calibration for the MUSIC algorithm is observed previously in [85] where the gain-phase mismatch of antennas is corrected by using a fixed, direction-independent calibration matrix with an assumption of ideal white noise. In our case, we treat the problem for multipath case [28] where the calibration is used to compensate for directional dependency as well. In addition, an optimum diagonal calibration matrix is used by employing known transmit signals.

In order to estimate the near-field DOA angles, a near-field to far-field transformation (NFT) is proposed. In [86] and [87], NFT is applied to array data where the correlated near-field signals are treated. In our case, we consider mixed signals involving both near- and far-field signals. Furthermore we consider the virtual array concept in order to use circular array to obtain omni-directional DF performance. Hence our NFT approach has two functions, namely, near-to-far and circular-to-linear array mapping. The NFT matrix is used to map uniform circular array (UCA) output to a virtual uniform linear array (ULA) in order to use forward-backward spatial smoothing (FBSS) [88]. It is shown that such a synthetic transformation matrix leads to sufficiently good results even for close-to-real world scenarios. The accuracy of the NFT matrix can be attributed to the use of exact near-field model as well as the model differences between near- and far-field sources. In order to estimate the near-field range parameters, a compressive sensing technique [53, 54] is used. A convex optimization problem for the near-field range parameter estimation is outlined. A dictionary matrix generated using the far- and near-field DOA angle estimates is used in this convex problem.

The proposed method is evaluated using two data sets. One set of data is generated in accordance with the array models where the method is based on. The other data set is obtained from the electromagnetic simulation tool, Wireless Insite [89] using a realistic scenario in an irregular terrain.

4.2   Problem Description and Array Model

In HF DF applications, the task is to find the HF transmitter DOA angle when both the transmitter and receive array are placed in an irregular terrain. In HF, multipaths have significant effects compared to Very High/Ultra High Frequency (VHF/UHF) bands. Usually there is a single source [65] in a given frequency band. The array receives several multipaths from the near-field terrain. Hence the main problem is to find the DOA of the far-field source under the existence of coherent near-field multipaths. In addition, the direction of the near-field multipaths as well as their ranges are desired to be found. While far-field multipath components such as reflections from the iono-sphere affect the DF accuracy, these are ignored in this work. Note that while such far-field components decrease the accuracy, near-field multipath components have much larger impact on the DF accuracy.

In this study, a single far-field source with multiple near-field multipaths is assumed. The source signal is narrowband. Noise is assumed to be temporally and spatially white, zero-mean Gaussian. The array consists of M antennas and there are N sources where $N-1$ of these are near-field multipaths. The signal model can be given as

$$\mathbf{y}(t) = \alpha_1 \mathbf{a}(\Theta_1) s(t) + \sum_{i=2}^{N} \alpha_i \tilde{\mathbf{a}}(\Theta_i, d_i) s(t) + \mathbf{e}(t), \ t = 1, \ldots, T \qquad (4.1)$$

where T is the number of snapshots, $s(t)$ is the far-field source signal and $\mathbf{e}(t)$ is the noise vector. $\Theta_i = (\phi_i, \theta_i)$ denotes azimuth ϕ_i and elevation angles θ_i respectively. d_i is the range of the ith near-field source. α_i is a positive scalar and represents the signal amplitude. $\mathbf{a}(\Theta_1)$ is $M \times 1$ array steering vector for the far-field source and its mth element is given by

$$a_m(\Theta_1) = \exp\{j\frac{2\pi}{\lambda}\mathbf{r}^T \mathbf{p}_m\} \qquad (4.2)$$

41

where λ is the wavelength and $\mathbf{r}$ is given as

$$\mathbf{r} = [\cos(\phi_i)\sin(\theta_i), \; \sin(\phi_i)\sin(\theta_i), \; \cos(\theta_i)]^T. \tag{4.3}$$

$\mathbf{p}_m = [x_m \; y_m \; z_m]^T$ is the antenna positions. $\tilde{\mathbf{a}}(\Theta_i, d_i)$ is the steering vector defined for the ith near-field source and its mth element $\tilde{a}_m(\Theta_i, d_i)$ is defined with exact near-field model as

$$\tilde{a}_m(\Theta_i, d_i) = \exp\left\{ -j\frac{2\pi}{\lambda}d_i\left(\sqrt{1 - \frac{2}{d_i}\mathbf{r}^T\mathbf{p}_m + \frac{\mathbf{p}_m^T\mathbf{p}_m}{d_i^2}} - 1\right)\right\}. \tag{4.4}$$

In the literature, approximate array steering vector formulations [66] are given. A commonly used approximate expression is

$$\tilde{a}_m^{ap}(\Theta_i, d_i) = \exp\left\{ j\frac{2\pi}{\lambda}[\mathbf{r}^T\mathbf{p}_m - \frac{1}{2d_i}\tilde{\mathbf{r}}^T\tilde{\mathbf{p}}_m]\right\} \tag{4.5}$$

where

$$\tilde{\mathbf{r}} = [1 - \cos^2(\phi_i)\sin^2(\theta_i), \; 1 - \sin^2(\phi_i)\sin^2(\theta_i), \; 1 - \cos^2(\theta_i)]^T \tag{4.6}$$

and $\tilde{\mathbf{p}}_m = [x_m^2, \; y_m^2, \; z_m^2]^T$. The difference between $\tilde{a}_m(\Theta_i, d_i)$ and $\tilde{a}_m^{ap}(\Theta_i, d_i)$ becomes large especially when d_i is small. Therefore exact near-field model and steering vector in (4.4) is used in this study.

4.3 Direction Finding for A Far-Field Source With Multipath Components

In this part, far-field source DOA is estimated by using a calibration operation in order to model the array imperfections. In DF applications, where multipath distortion is dominant, calibration is required to generate a priori information without which DF problem is very hard to solve if it is not impossible [28]. In this study, multipath signals are modeled in the far-field array model by using a calibration matrix. The array model in (4.1) can be written for the mth antenna as

$$y_m(t) = \alpha_1 a_m(\Theta_1)s(t) + \sum_{i=2}^{N} \alpha_i \tilde{a}_m(\Theta_i, d_i)s(t) + e_m(t) \tag{4.7}$$

which can always be written as

$$y_m(t) = \alpha_1 a_m(\Theta_1)s(t)(1 + \beta_{m2} + \beta_{m3} + \cdots + \beta_{mN}) + e_m(t) \tag{4.8}$$

42

where β_{mi} is a complex direction-dependent coefficient. Then the array model for far-field sources can be given as

$$\mathbf{y}(t) = \mathbf{\Gamma}(\Theta)\mathbf{a}(\Theta)s(t) + \mathbf{e}(t), \ t = 1, \ldots, T \qquad (4.9)$$

where $\mathbf{\Gamma}(\Theta)$ is a direction-dependent diagonal matrix and it represents the effect of near-field multipaths on far-field source as well as the mutual coupling [61] between the antennas and gain/phase mismatch errors. Note that the model in (4.9) has a single far-field source and the artifacts from near-field sources are represented by $\mathbf{\Gamma}(\Theta)$. Hence, it is always possible to use the MUSIC algorithm to find Θ as long as $\mathbf{\Gamma}(\Theta)$ is known even if the near-field and far-field sources are coherent. Here, $\mathbf{\Gamma}(\Theta)$ is found by the calibration operation [28]. While a full matrix for better performance and modeling accuracy may be preferred, the coefficients of this matrix cannot be found from the calibration since there are more unknowns than the known terms in our case. Let $\bar{\mathbf{a}}(\Theta_i)$ be the calibration measurement obtained for the far-field source in $\Theta_i = (\phi_i, \theta_i)$ angle. A number of calibration measurements should be collected for a good DF performance. While DF performance improves as the number of measurements increases, the cost, duration and labor involved in the calibration usually limit these measurements. Let $\bar{\mathbf{A}} = [\bar{\mathbf{a}}(\Theta_1), \bar{\mathbf{a}}(\Theta_2), \ldots, \bar{\mathbf{a}}(\Theta_P)]$ be the set of measurements collected during the calibration for different azimuth and elevation angles in a given operating frequency. The data is collected uniformly in δ_ϕ and δ_θ steps for the azimuth and elevation angles respectively. Assuming that $s(t)$ is known during calibration, an estimate of $\bar{\mathbf{a}}(\Theta)$ can be found as [2]

$$\hat{\bar{\mathbf{a}}}(\Theta) = \frac{\sum_{t=1}^{T} \bar{\mathbf{y}}(t)s^*(t)}{\sum_{t=1}^{T} |s(t)|^2}. \qquad (4.10)$$

Then the elements of $\mathbf{\Gamma}(\Theta_i) = diag(\gamma_1, \ldots, \gamma_M)$ can be found as

$$\gamma_{im} = \frac{\hat{\bar{a}}_m(\Theta_i)}{a_m(\Theta_i)} \qquad (4.11)$$

where $\hat{\bar{a}}_m(\Theta_i)$ in (4.10) and $a_m(\Theta_i)$ in (4.9) are the mth elements of the estimated real steering vector and the nominal steering vector respectively. It is possible to choose $\delta_\phi = 5°$ and $\delta_\theta = 5°$ and the calibration data can be interpolated to obtain total angular coverage.

Once the calibration matrices $\mathbf{\Gamma}(\Theta_i)$, $i = 1, \ldots, P$ are found, DOA angle for the far-field source can be found using the MUSIC algorithm where pseudo-spectrum is

given as

$$\mathbf{P}(\Theta_p) = \frac{1}{\mathbf{a}^H(\Theta_p)\mathbf{\Gamma}^H(\Theta_p)\hat{\mathbf{G}}\hat{\mathbf{G}}^H\mathbf{\Gamma}(\Theta_p)\mathbf{a}(\Theta_p)}. \tag{4.12}$$

$\hat{\mathbf{G}}$ is a $M \times M - 1$ matrix corresponding to the noise subspace eigenvectors of the covariance matrix

$$\hat{\mathbf{R}} = \frac{1}{T}\sum_{t=1}^{T}\bar{\mathbf{y}}(t)\bar{\mathbf{y}}^H(t). \tag{4.13}$$

The MUSIC algorithm with calibration for a fixed elevation angle works as follows (Cal-MUSIC):

1. Start with $p = 0$ and $\phi_p = 0°$.

2. Find the calibration angle ϕ_i, $i = 1, \ldots, P$, which is closest to the search angle ϕ_p, i.e. $|\phi_i - \phi_p|$ is minimum and select the corresponding calibration matrix $\mathbf{\Gamma}(\phi_i)$ and set $\mathbf{\Gamma}(\phi_p) = \mathbf{\Gamma}(\phi_i)$.

3. Compute the pseudo-spectrum $\mathbf{P}(\phi_p)$.

4. Take $\phi_{p+1} = \phi_p + \delta_\phi$ and if $p + 1 = P$, stop; otherwise continue from Step 2.

The above procedure is repeated for different elevation angles. The largest peak in the $\mathbf{P}(\Theta_p)$ spectrum corresponds to the far-field source DOA angle (ϕ_1, θ_1).

4.4 Near-field Source Localization

In this part, near-field source DOA's and ranges are found given the observed array output which includes both far- and near-field sources.

The idea in the proposed approach is to use near-field to far-field transformation (NFT) matrix which maps the near-field steering vectors to far-field steering vectors. Fortunately, such a transformation distributes the power of the far-field component throughout the MUSIC pseudo-spectrum. Consequently, the far-field component becomes interference with a limited power for the transformed near-field observations. Since the far-field and multipath components are coherent, the FBSS should be used before the MUSIC algorithm to improve the rank of the covariance matrix.
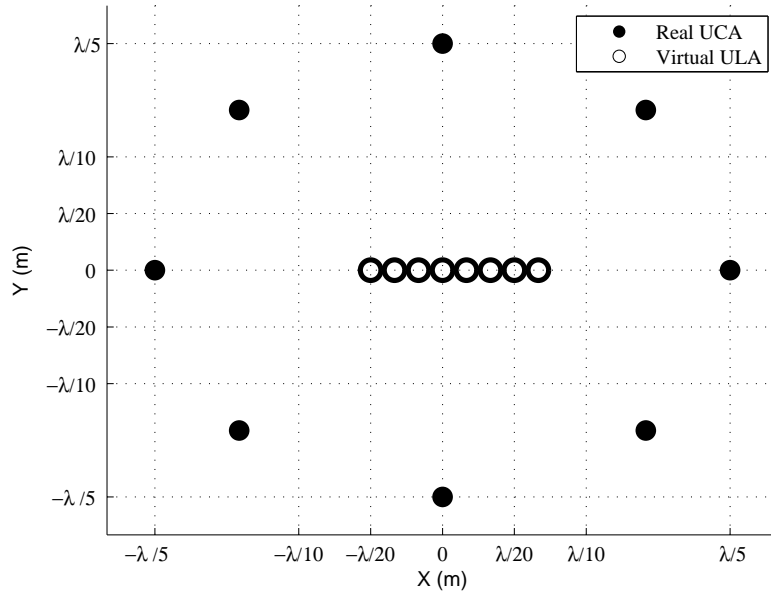
Figure 4.1: Placement of the real DF array (UCA) and virtually generated ULA for near-field source localization.

The NFT matrix $\mathbf{T}$ has two functions. It converts the near-field sources to far-field and maps from a real array to a virtual ULA as shown in Fig. 4.1.

$\mathbf{T}$ should be constructed off-line before any DF estimation. The main advantage of the proposed approach is the generation of $\mathbf{T}$ using virtual data in a computer. In other words, there is no need for actual data collection which may be a prohibitively hard task. Another advantage is to select the best inter-element spacing of the virtually generated ULA for the array transformation and near-field DOA angle estimation with a sufficient accuracy. The selection of the virtual ULA is described in Sec. 4.4.1.

The NFT matrix is constructed by generating two data sets, namely, far-field data set for ULA and near-field data set for virtual UCA. Far-field data set is generated from (4.2) and (4.9) using the artificial far-field sources placed at $\Theta_{kl} = (\phi_k, \theta_l)$ where ϕ_k changes between $0°$ and $360°$ in Δ_ϕ degrees resolution. $\theta_l \in [\hat{\theta} - \Delta_\theta, \ \hat{\theta} + \Delta_\theta]$ and $\hat{\theta}$ is the estimated elevation angle of the far-field source in (4.12). Δ_θ is the range in elevation angle. Near-field data set uses (4.4) for the same DOA set of $\Theta_{kl} = (\phi_k, \theta_l)$ and the range is $\bar{d}_j = j\Delta_d, \ j = 1, \ldots, J$ with Δ_d grid size. The grid size for angle and range is problem dependent. As a rule of thumb, 5 degrees for Δ_ϕ and 0.5 meters for Δ_d give satisfactory results in general. The transformation matrix is constructed

45

for K azimuth, L elevation angles and J ranges. The near-field steering vectors are stacked in a $M \times KLJ$ matrix $\mathbf{U}$ as follows

$$\mathbf{U} = [\mathbf{U}_1, \ldots, \mathbf{U}_j, \ldots, \mathbf{U}_J] \tag{4.14}$$

where

$$\mathbf{U}_j = [\tilde{\mathbf{a}}(\Theta_{11}, \bar{d}_j), \ldots, \tilde{\mathbf{a}}(\Theta_{K1}, \bar{d}_j), \tilde{\mathbf{a}}(\Theta_{12}, \bar{d}_j), \ldots, \tilde{\mathbf{a}}(\Theta_{KL}, \bar{d}_j)] \tag{4.15}$$

and $\tilde{\mathbf{a}}(\Theta_{kl}, \bar{d}_j)$ is the steering vector generated for the UCA using the near-field model in (4.4). $M \times KLJ$ far-field data set $\mathbf{V}$ is constructed by concatenating J many $M \times KL$ matrix $\mathbf{V}_j$ as $\mathbf{V} = [\mathbf{V}_1, \ldots, \mathbf{V}_j, \ldots, \mathbf{V}_J]$ where $\mathbf{V}_j$ which is constructed as

$$\mathbf{V}_j = [\mathbf{a}(\Theta_{11}), \ldots, \mathbf{a}(\Theta_{K1}), \mathbf{a}(\Theta_{12}), \ldots, \mathbf{a}(\Theta_{KL})] \tag{4.16}$$

using the steering vectors as in (4.9) which have no range dependency, hence $\mathbf{V}_1 = \mathbf{V}_2 = \cdots = \mathbf{V}_j = \cdots = \mathbf{V}_J$. Finally, the relation between near-field and far-field data gives the transformation matrix $\mathbf{T}$ as

$$\mathbf{V} = \mathbf{T}\mathbf{U}. \tag{4.17}$$

The least-squares solution for $\mathbf{T}$ is given as

$$\mathbf{T} = \mathbf{V}\mathbf{U}^\dagger \tag{4.18}$$

where $\dagger$ denotes the Moore-Penrose pseudo-inverse.

The observed data obtained from UCA consists of far-field and near-field components. The near-field components of the observation can be multipaths which are coherent. In this case, the MUSIC algorithm fails since the signal subspace is not orthogonal to noise subspace. In order to overcome this problem, UCA data is mapped to a virtual ULA by using the NFT and then FBSS is employed. Since elevation angle cannot be found for one dimensional arrays, elevation angle for multipaths are set as $90°$ for simplicity.

4.4.1 Selection of The Virtual Array Spacing

In order to estimate the near-field parameters accurately, the choice of the virtual array spacing l becomes an important issue. The output of the circular array with $\lambda/5$ radius
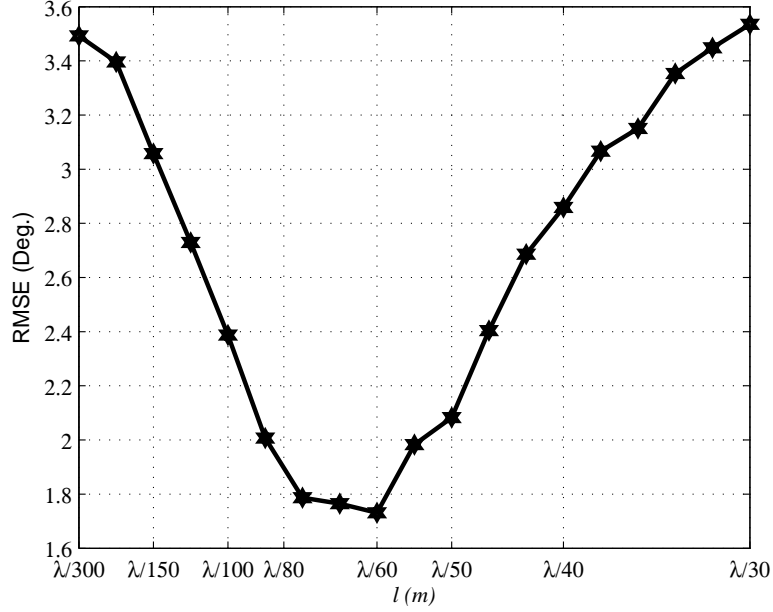
Figure 4.2: RMSE for azimuth angle estimation vs virtual ULA inter-element distance, l, for the virtual array transformation.

is mapped to a virtual ULA which is shown in Fig. 4.1 with inter-element spacing l. This value affects the accuracy of the DOA estimation. In Fig. 4.2, RMSE for azimuth angle estimation is shown for inter-element spacing l from $\lambda/300$ to $\lambda/30$. The RMSE definition is given in detail in Appendix A. As it is seen from this figure, DF accuracy has a "V" shaped characteristics. Therefore a reasonable choice for l can be obtained from Fig. 4.2. In our case, $l = \lambda/60$ seems a good choice for the near-field localization with the NFT.

4.4.2 DOA Estimation for Near-Field Sources

Once the far-field source DOA is estimated as in (4.12), the next step is to find the DOA angles for the near-field sources. The transformed array output can be written as

$$\tilde{\mathbf{y}}(t) = \mathbf{T}\,\mathbf{y}(t) = \mathbf{T}\alpha_1\mathbf{a}(\Theta_1)s(t) + \sum_{i=2}^{N}\mathbf{T}\alpha_i\tilde{\mathbf{a}}(\Theta_i, d_i)s(t) + \mathbf{T}\mathbf{e}(t). \qquad (4.19)$$

In (4.19), the far-field component of $\mathbf{y}(t)$ is suppressed. $\tilde{\mathbf{y}}(t)$ includes the near-field source parameters in the far-field model and it can be used in the FBSS algorithm to

47

estimate the near-field source DOAs $\{\hat{\Theta}_i\}_{i=2}^N$.

Sample covariance matrix of the transformed array output

$$\tilde{\mathbf{R}} = \frac{1}{T} \sum_{t=1}^{T} \tilde{\mathbf{y}}(t)\tilde{\mathbf{y}}^H(t) \tag{4.20}$$

is used and the FBSS is applied to obtain the smoothed $\bar{M} \times \bar{M}$ covariance matrix $\bar{\mathbf{R}}$. Here, $\bar{M}$ is the number of antennas in the subarrays of the virtual ULA and $\tilde{M} \geq \lfloor \frac{3}{2}(N-1) \rfloor$ where $\lfloor . \rfloor$ is the rounding operation. Then, the MUSIC algorithm can be employed to compute the near-field source azimuth angles. The MUSIC pseudo-spectrum can be computed as

$$\tilde{\mathbf{P}}(\phi) = \frac{1}{\mathbf{a}^H(\phi)\bar{\mathbf{G}}\bar{\mathbf{G}}^H\mathbf{a}(\phi)} \tag{4.21}$$

where $\bar{\mathbf{G}}$ is composed of the noise space eigenvectors of $\bar{\mathbf{R}}$. Since 1-D array is used, elevation angle cannot be found. $\{\hat{\theta}_i\}_{i=2}^N = 90°$ is selected for simplicity.

4.4.3 Range Estimation With Compressive Sensing

Compressive sensing (CS) is a very popular technique used in parameter estimation for the signals having sparsity property [90, 91]. The compressive sensing theory addresses the following problem

$$\mathbf{y} = \mathbf{\Phi}\mathbf{x} + \boldsymbol{\zeta} \tag{4.22}$$

where $\mathbf{\Phi}$ is $M \times \bar{N}$ sensing matrix with $M \ll \bar{N}$ and $\boldsymbol{\zeta}$ is the white Gaussian noise vector. The aim of the CS theory is to recover the signal $\mathbf{x}$ from the observation vector $\mathbf{y}$. According to the CS theory, the signal $\mathbf{x}$ can be recovered if it is compressible or sparse [92]. In other words, $\mathbf{x}$ is said to be S-sparse for the sparsity rate S, if the observations of the sensing matrix $\mathbf{\Phi}$ obey $M \geq C \cdot S \cdot log(\bar{N})$ for some constant C [53]. Then $\mathbf{x}$ can be represented as

$$\mathbf{x} = \mathbf{\Psi}\mathbf{s} \tag{4.23}$$

where $\mathbf{\Psi} \in \mathbb{C}^{\bar{N} \times \bar{N}}$ is the sparsity basis and $\mathbf{s}$ is $\bar{N} \times 1$ vector with $S \ll \bar{N}$ non-zero entries. The compressed signal can be written as

$$\mathbf{y} = \mathbf{\Phi}\mathbf{x} = \mathbf{\Phi}\mathbf{\Psi}\mathbf{s}. \tag{4.24}$$

The columns of the sensing matrix $\boldsymbol{\Phi}$ should be incoherent where coherence for $\boldsymbol{\Phi}$ is defined based on its column vectors $\boldsymbol{\phi}_k$, i.e.,

$$\mu(\boldsymbol{\Phi}) = \max_{1 \le k \ne l \le \bar{N}} \frac{|<\boldsymbol{\phi}_k, \boldsymbol{\phi}_l>|}{||\boldsymbol{\phi}_k||_2 \cdot ||\boldsymbol{\phi}_l||_2}. \tag{4.25}$$

The lower bound for $\mu(\boldsymbol{\Phi})$ is $1/\sqrt{M}$ for $M \ll \bar{N}$ [93].

In this study, compressive sensing is used to estimate the ranges of the near-field sources with the following convex optimization problem

$$\arg \min_{\mathbf{x} \in \mathbb{C}^{\bar{N}}} ||\mathbf{x}||_1 \quad \text{subject to } ||\mathbf{y} - \boldsymbol{\Phi}\mathbf{x}||_2^2 \le \epsilon \tag{4.26}$$

where the power of the residual $\boldsymbol{\zeta} = \mathbf{y} - \boldsymbol{\Phi}\mathbf{x}$ is bounded by ϵ [52]. Since the observation vector is composed of the far- and near-field components, the sensing matrix is generated with both far- and near-field components. The sensing matrix (or dictionary) is constructed using the DOA angle estimates found in Sec. 4.3 and Sec. 4.4.2. First, the far-field steering vector $\mathbf{a}(\hat{\Theta}_1)$ is generated. Then the near-field steering vectors $\tilde{\mathbf{a}}(\hat{\Theta}_i, d_i)$ are generated for a set of ranges, namely, $\bar{d}_j = j\Delta_d$, $j = 1, \ldots, J$ is the range set where Δ_d is the grid size in meters. Finally, the far- and near-field steering vectors are stacked into $M \times J(N-1) + 1$ sensing matrix as follows

$$\boldsymbol{\Phi} = [\mathbf{a}(\hat{\Theta}_1), \tilde{\mathbf{a}}(\hat{\Theta}_2, \bar{d}_1), \ldots, \tilde{\mathbf{a}}(\hat{\Theta}_2, \bar{d}_J), \ldots, \tilde{\mathbf{a}}(\hat{\Theta}_N, \bar{d}_J)]. \tag{4.27}$$

In the solution of the CS problem in (4.26), N most significant elements of $\hat{\mathbf{x}}$ correspond to the far- and near-field components of the observation. Here, $N \ll \bar{N}$ for $M \times \bar{N}$ sensing matrix where $\bar{N} = J(N-1)+1$. Since $\mathbf{y}$ is composed of a single far-field and $N - 1$ near-field source components, sparsity property is satisfied. Another property to satisfy is the incoherency of the measurement basis in the sensing matrix, $\boldsymbol{\Phi}$. In our case, $\boldsymbol{\Phi}$ is composed of a single far-field and several near-field steering vectors with different ranges. Hence each of these vectors are linearly independent and it can be shown to satisfy the incoherency property similar to [94]. The algorithm steps for the range estimation with compressive sensing are as follows:

1. Construct the far (4.2) and near-field (4.4) steering vectors $\mathbf{a}(\hat{\Theta}_1)$ and $\tilde{\mathbf{a}}(\hat{\Theta}_i, \bar{d}_j)$ for $\{\Theta_i\}_{i=2}^{N}$ and $j = 1, \ldots, J$. Obtain the sensing matrix $\boldsymbol{\Phi}$ by stacking the steering vectors as in (4.27).

2. Solve the convex problem in (4.26) for $\hat{\mathbf{x}}$. The $N - 1$ most significant terms in the $J(N - 1) + 1 \times 1$ vector $\hat{\mathbf{x}}$ excluding the far-field component are the signal amplitudes which correspond to the near-field source ranges $\{\hat{d}_i\}_{i=2}^{N}$.

4.5 Simulation Results

In this section, the performance of the proposed DF method is evaluated. The algorithmic steps for the proposed approach can be outlined in Fig. 4.3. The proposed method is evaluated in three experiments. In the first experiment, only the far-field DOA estimation is considered. Array output in (4.1) and calibration data are generated in MATLAB and DOA estimation performance is evaluated for a far-field source with near-field multipaths. Only the far-field DOA estimation performance is evaluated in this experiment. In the second experiment, far and near field source DOA's as well as near-field source ranges are estimated. DOA angle of the far-field source is estimated using the calibration technique. The NFT matrix is found in order to estimate the near-field azimuth angles for $(K, L, J) = (72, 3, 500)$ with $(\Delta_\phi, \Delta_\theta, \Delta_d) = (5°, 5°, 0.1m)$. Then the CS algorithm is used to estimate the near-field source ranges and amplitudes. These two experiments are presented to show the performance of the proposed method in accordance with the ideal array model given in (4.1) and (4.4).

In the third experiment, the array output and calibration data are obtained using a numerical electromagnetic simulation tool, Wireless Insite [89]. DF array and the transmitter are placed in an irregular terrain area and the ray paths are observed after the simulation. The experiment is performed at 100 MHz since this is the lowest frequency to obtain a valid response for Wireless Insite. However, we have used the scaling property of the electromagnetic theory [62] in order to observe the results for 3 MHz HF scenario as well. The setup parameters are given in Table 4.1. Note that UCA radius is selected as $\lambda/5$ in accordance with the radius in 3MHz to conform to the physical area limits which is usually the case. The DF array is positioned in an irregular terrain and DOA angles of the far-field emitter source as well as the near-field multipath reflection locations are estimated. This experiment shows the performance of the proposed approach for a close-to-real world scenario.
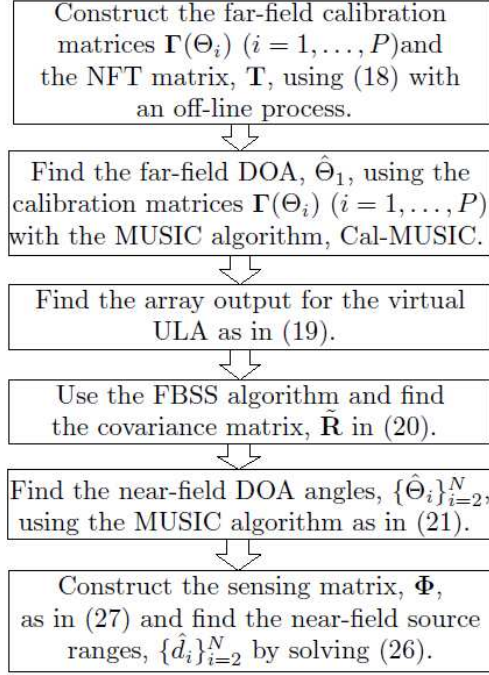
Figure 4.3: The algorithm steps for the proposed approach.

Table 4.1: The setup parameters used in the irregular terrain model.

Frequency (MHz):	3
Antenna length (m):	9
Antenna height from ground (m):	0.3
Array radius (m):	20
Conductivity of earth (S/m):	0.02

4.5.1 Experiment 1

In this experiment, far-field DOA estimation performance of the proposed method is evaluated for the whole azimuth range. The DF array is an UCA composed of $M = 8$ monopole antennas with $\lambda/5$ radius. The test data is generated in four sectors $[0°,\ 90°]$, $[90°,\ 180°]$, $[180°,\ 270°]$ and $[270°,\ 360°]$ respectively. In each sector, there are two fixed near-field sources while far-field source changes with $1°$ azimuth angle step and at fixed elevation angle $\theta = 88°$. Calibration data for the far-field DOA estimation is collected in 360 degrees with $5°$ azimuth angle step. The data is collected for the elevation angles $85°$, $90°$ and $95°$ respectively. Calibration data is interpolated to obtain $1°$ resolution in azimuth.

The performance of the proposed method for estimating the azimuth angle of a far-

51
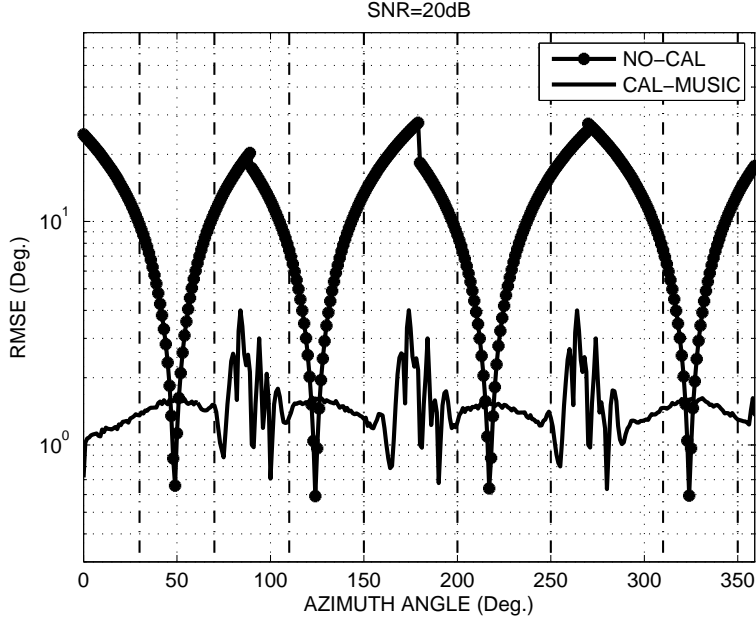
Figure 4.4: Performance of azimuth angle estimation of the proposed method when the elevation angle is set at $\theta = 88°$. Vertical lines correspond to the fixed near-field sources.

field source is given in Fig. 4.4 for SNR=20dB and 500 Monte Carlo trials. Here, the azimuth angles of fixed near-field sources are shown with vertical lines whose elevation angles are $90°$. As it is seen, when there is no calibration, DF accuracy is unacceptable due to the near-field sources. After calibration, maximum DF error is approximately $4°$ and average value is about $1.5°$. This is quite acceptable in practice [95] and a significant improvement compared to the uncalibrated performance. The DF performance on elevation angle is presented in Fig. 4.5. The same observations can be made for the elevation DF performance as well. Note that the elevation angle to be estimated is the same in each trial which is $88°$.

4.5.2 Experiment 2

In this experiment, a far-field source with two near-field multipath components is considered. In order to estimate the far-field DOA angle, calibration data is constructed as explained in the first experiment. In order to estimate the near-field sources, the NFT matrix **T** is computed and the virtual ULA output is obtained for the inter-element spacing $l = \lambda/60$. Then, the DOA angle of the near-field sources are estimated using
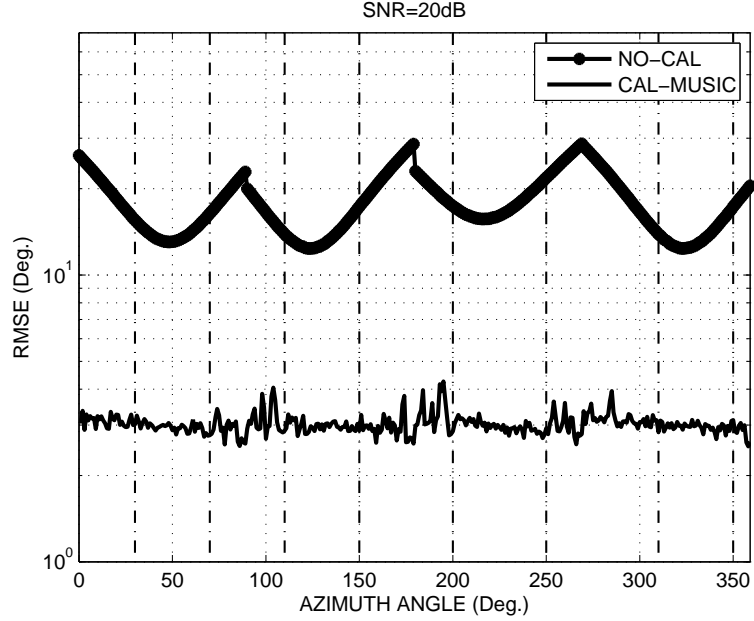
Figure 4.5: Performance of the fixed elevation angle ($\theta = 88°$) estimation of the proposed method. Vertical lines correspond to the fixed near-field sources.

the MUSIC algorithm and FBSS method. The simulations are run for 500 Monte Carlo trials at SNR =20dB and the root-mean-square (RMS) of the estimated parameters are obtained. The result for the far-field source DOA is shown in Fig. 4.6a. As it is seen from this figure, far-field source DOA is found accurately when calibration is used. The result for direct application of the MUSIC algorithm is not satisfactory. Three degrees azimuth error and two degrees elevation error are considered to be very good in practice by [95]. The sensing matrix Φ is constructed for a range set using the far and near-field DOA angle estimates. Note that the solution of the CS problem considers only the ranges of the near-field sources with pre-estimated DOA angles which reduces the computational complexity. Fig. 4.6.b-c and Table 4.2.a show the DF performance for the near-field sources. As it is seen, the parameters of the near-field sources are estimated with high accuracy implying that the proposed approach is very effective to estimate the azimuth angles, range and amplitudes of the near-field sources.

53
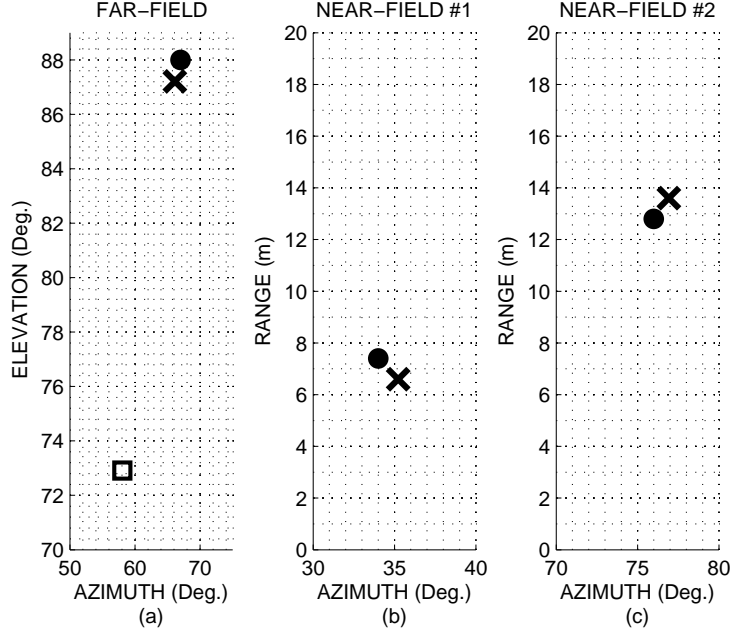
Figure 4.6: DF performance of the proposed method for the far-field and near-field sources on azimuth, elevation and ranges. Dot: True position; Square: Uncalibrated; Cross: With calibration.

Table 4.2: Amplitude estimation of the near-field sources for the experiment 2 and 3. Note that the near-field amplitude estimates are normalized with the far-field source amplitude.

(a)	Estimated	True	Error percentage (%)
Near-field #1:	0.65	0.70	6.78
Near-field #2:	0.62	0.50	25.52
(b)	Estimated	True	Error percentage (%)
Near-field #1 :	0.48	0.72	33.42

4.5.3 Experiment 3

In this experiment, the proposed method is evaluated by using a more realistic data generated by Wireless Insite employing Full-3D propagation model. The DF array in Table 4.1 with $M = 8$ antennas in a circular geometry is placed in an irregular terrain area as shown in Fig. 4.7. Monopole antennas are used and a single far-field transmit antenna is placed about 3.6 km (before scaling) away from the DF array as shown in Fig. 4.7. The direct and reflected ray paths of the transmitted signal can be seen from the figure. In this scenario, the terrain in the near vicinity of the DF array generate multipaths. In this case, there is only one near-field multipath component. A detailed

54
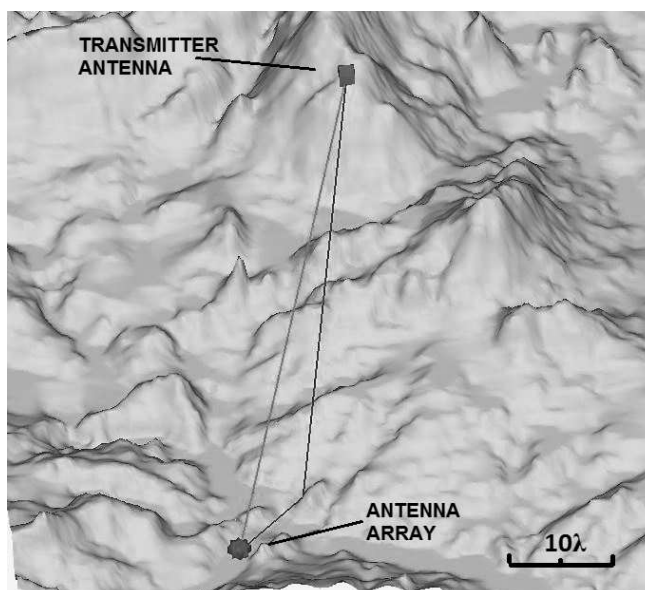
Figure 4.7: The placement of the DF array and transmitter antenna over the irregular terrain area.

demonstration of the direct and multipath components is presented in Fig. 4.8.
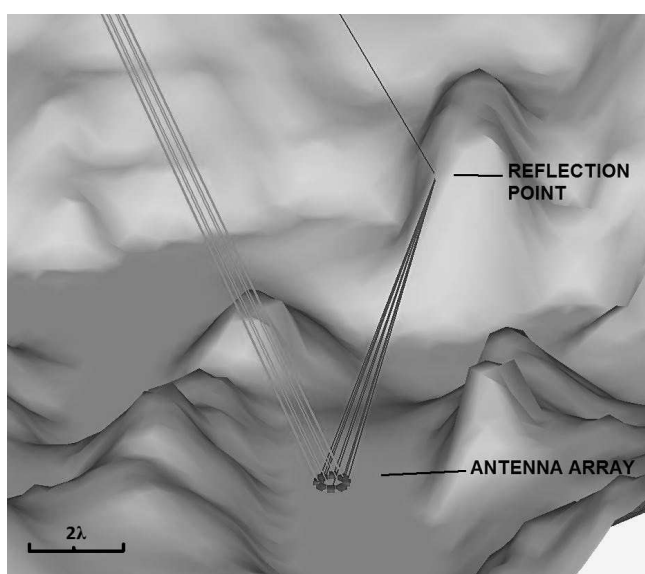
Figure 4.8: The direct and reflecting ray paths arriving the antenna array.

In order to estimate the far-field source DOA angle, calibration data is collected by placing the calibration transmitters uniformly on the circumference of a circle with 50m radius as shown in Fig. 4.9 at 100MHz. Note that $\lambda = 3$ meters for $f = 100$MHz and 50m$>10\lambda$ satisfies the far-field condition. The calibration data is collected with $5°$ azimuth angle step starting from $2°$ to $357°$ at a fixed elevation angle of $69.1°$ whereas the elevation angle of the far-field source is $\theta_1 = 67.9°$. Calibration data

55
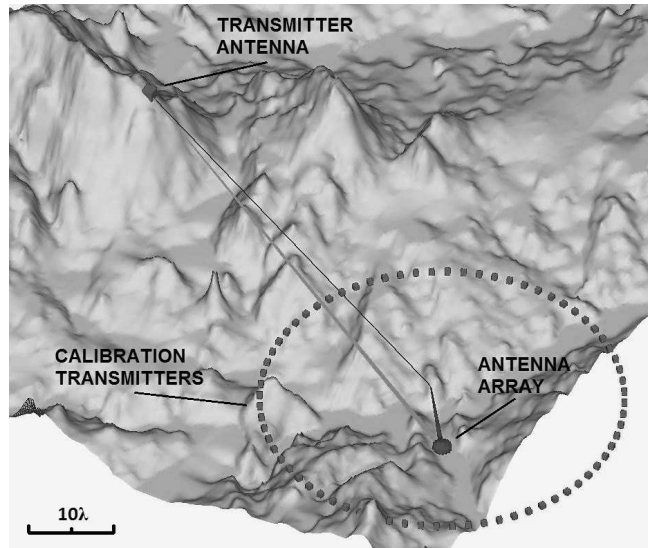
Figure 4.9: The placement of the transmitters for the array calibration.

is then interpolated to obtain $1°$ resolution in azimuth. Fig. 4.10.a shows the far-field 2-D DOA estimates before and after the calibration. As it is seen, calibration improves the DF accuracy and mitigates the errors due to near-field multipaths. The estimated azimuth angle, range and amplitude parameters for the near-field source are given in Fig. 4.10.b and Table 4.2.b. The error in azimuth angle of the near-field multipath is about 0.5 degrees which can be seen as a very good result. The range and the amplitude of the near-field multipath reflection is also estimated with sufficiently good accuracy.
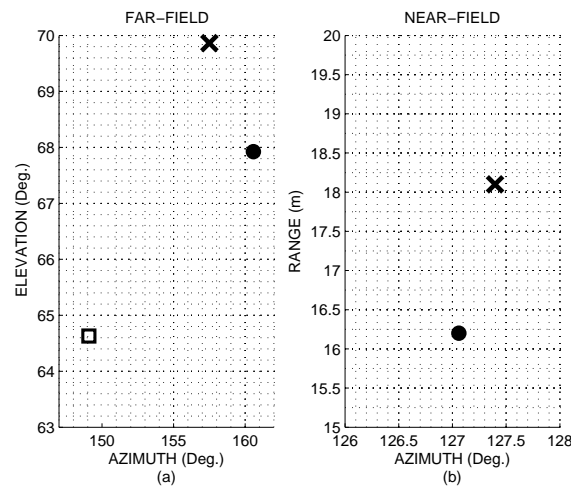
Figure 4.10: Estimation results of the proposed method for a scenario simulated in Wireless Insite. Dot: True position; Square: Uncalibrated; Cross: With calibration.

4.6 The advantages of The Proposed Method

The advantages of the proposed method are as follows:

- The proposed method works well in multipath scenario since it is not based on the independence assumption.

- The proposed method can be used in HF DF applications where the near-field multipaths are major distortions.

- The proposed method can be used for uniform circular arrays whereas most of the algorithms use linear antenna arrays where 2-D parameter estimation is not possible.

CHAPTER 5

2-D DOA AND MUTUAL COUPLING COEFFICIENT
ESTIMATION FOR ARBITRARY ARRAY STRUCTURES
WITH A SINGLE AND MULTIPLE SNAPSHOTS

Direction-of-arrival (DOA) estimation for arbitrary array structures in the presence of mutual coupling (MC) is an important problem for antenna arrays. Previous methods in the literature are usually proposed for certain array geometries and show limited performance at low SNR or for small number of snapshots. In this chapter, a new method is used to estimate both DOA and MC coefficients with a single and multiple snapshots for an unstructured array where the antennas are placed arbitrarily in space. The proposed method can effectively estimate both source DOA angles and MC coefficients for any type of array geometries.

5.1   Introduction

Direction-of-arrival (DOA) estimation of the plane waves impinging on antenna arrays is an important problem in a variety of fields including, radar, sonar, acoustics and communications [1, 96]. Several high resolution methods are proposed to estimate the DOA angles of unknown source signals [3], [97], [41]. Most of these methods perform well in ideal scenarios. In practical antenna array applications, received signal is usually affected by mutual coupling (MC) generating distortions in the array model [4], [5].

There are several methods in the literature which estimate DOA angles in antenna

59

arrays with MC [6, 21–24]. Most of these methods are based on the eigenstructure of the array covariance matrix and require uniform array structure. These methods are based on the special MC matrix structures and applicable only for uniform arrays. Since arbitrary array geometries are considered in this part of the thesis, above methods cannot be applied for our case.

While there are different methods for DOA estimation with arbitrary array structures [48–50], MC effect is considered in only limited number of works [32]. In [32], online MC calibration with randomly placed array is considered for DOA estimation using techniques based-on higher order statistics. [32] employs the array covariance matrix which is estimated by assuming that the source signals are independent. This assumption is not valid for finite length signals especially when the number of snapshots is small. Hence, its performance is not acceptable at low SNR and for small number of snapshots. Moreover, sources and the antenna array are assumed to be in the same plane leading to only 1-D (azimuth) DOA estimation. In this work, in addition to 1-D scenario, 2-D (azimuth and elevation) DOA estimation is considered for source localization where sources are distributed in 3-D space with different elevation angles.

DOA estimation with a single snapshot is an important problem especially when there is only a single observation or when the system parameters change in time [6]. Therefore, MC should be estimated online without interrupting the ongoing DOA estimation. Single snapshot DOA estimation without MC is considered in [98] using sparse recovery algorithms. The effect of MC in DOA estimation with single snapshot is investigated in [99] and [100]. In [99], a semicircular array is considered with known source DOA angles in the presence of MC and near-field scatterers. Numerical electromagnetic simulations are performed and a transformation-based approach is proposed. In [100], an iterative minimization approach is proposed for L-shaped array in case of unknown MC. This method is based on the special structure of the MC matrix. When the antenna array has arbitrary structure, this method also fails to estimate the MC.

Recently, compressed sensing (CS) is presented as an effective method for different problems [51, 52, 101–103]. CS theory deals with the recovery of sparse signals from

overcomplete and underdetermined linear measurements. Most of the CS algorithms consider the direction-finding (DF) problem with only external noise [59,60,104,105] as an error source and the effect of MC is usually ignored. Hence the conventional CS algorithms fail in case of MC [106]. MC should be modeled appropriately for a proper DOA estimation. DOA estimation under unknown MC is studied in [107] and [108] using sparse recovery techniques. In particular, [107] considers multiple snapshots with ULA geometry and proposes an l_1-SVD-like [105] algorithm. This method discards some of the array information in order to decrease the effect of MC which leads to "array shrinkage" [20]. In [108], Sparse Bayesian Array Calibration (SBAC) is proposed for ULA using expected-maximization under unknown MC. These methods also fail in case of randomly placed arrays.

In [106] and [33], DOA estimation with a single snapshot is considered for UCA geometry. In [33], a single far-field source and near-field multipath reflections are considered. In [106], single snapshot DOA estimation problem is considered for UCA in case of MC and a joint-sparse recovery (JSR) algorithm is proposed to estimate both DOA angles of the unknown source locations and MC coefficients. In this part of the thesis, the JSR approach proposed in [106] is extended to the case of arbitrary array structures in the presence of MC. Furthermore, both single and multiple snapshot cases are considered for DOA and MC coefficient estimation.

While the sparsity of a vector and matrix is well-known in the literature, joint-sparsity is recently used to exploit the special sparsity patterns in vector and matrices for DOA estimation [59, 60]. In [59], it is assumed that a vector is joint-sparse if all the subblocks are constructed from the same sparsity basis. In this case, subblocks share the same sparsity pattern. In [60], a matrix is said to be joint-sparse if all the columns of the matrix have the same sparsity level with the same row indices. In this study, both of above structures are used to exploit the joint-sparsity. In addition, joint-block sparse matrix is defined. Therefore, three different joint-sparsity structures are considered and they are outlined below.

1. Joint-sparse vectors [59]: $l_{2,0}$-norm is used to define the joint-sparsity for a vector whose subblocks share the same sparsity basis (See Def. 1).

2. Joint-sparse matrix [60]: $l_{2,0}$-norm is used to define joint-sparsity for a matrix

whose columns share the same sparsity pattern (See Def. 3).

3. Joint-block-sparse matrix: New mixed norms, i.e., $l_{2,2,0}$-norm and $l_{2,2,1}$-norm are defined to employ joint-block-sparsity for matrices whose subblocks and columns share the same sparsity pattern (See Def. 4).

The JSR problem is laid out in a form such that the source DOA angles and MC coefficients can be recovered using convex optimization techniques. In JSR, joint-sparsity property is considered instead of sparsity used in conventional techniques and the spatial source directions and coupling coefficients are embedded into a joint-sparse vector. A new dictionary matrix is defined in accordance with the symmetricity of the MC matrix. Since the construction of the MC matrix is general, the proposed method is suitable for recovering the support set of any array structure.

Once the JSR problem is solved, the source DOA angles are obtained from the support set. The recovered joint-sparse signal includes both coupling coefficients and the source directions. MC coefficients are estimated with a least square method by minimizing a cost function employing the known DOA angles [109]. In case of multiple snapshots, a quadratic minimization problem is treated and a closed form solution is obtained similar to [6].

5.2 Signal Model and Problem Formulation

DOA estimation in case of MC is considered where there are K narrowband, far-field source signals impinging on M-element randomly placed array. The MC matrix is denoted by $\mathbf{C} \in \mathbb{C}^{M \times M}$ which is direction independent and symmetric [6]. The array output can be written as follows

$$\mathbf{y}(t_i) = \mathbf{C}\bar{\mathbf{A}}\bar{\mathbf{s}}(t_i) + \mathbf{e}(t_i), \quad i = 1, \ldots, T \tag{5.1}$$

where T is the number of snapshots, $\mathbf{e}$ is the spatially and temporarily white, zero mean Gaussian noise with variance σ_N^2. $\bar{\mathbf{s}}(t_i) = [\bar{s}_1(t_i), \bar{s}_2(t_i), \ldots, \bar{s}_K(t_i)]^T$ is a $K \times 1$ vector composed of source signals. $\bar{\mathbf{A}}$ is $M \times K$ nominal array steering matrix and defined as

$$\bar{\mathbf{A}} = [\mathbf{a}(\bar{\Theta}_1), \mathbf{a}(\bar{\Theta}_2), \ldots, \mathbf{a}(\bar{\Theta}_K)] \tag{5.2}$$

where $\bar{\Theta}_k = (\bar{\phi}_k, \bar{\theta}_k)$ represents the azimuth and elevation angles of the kth source respectively. The mth element of the array steering vector $\mathbf{a}(\bar{\Theta}_k)$ is given as

$$a_m(\bar{\Theta}_k) = \exp\left\{ j\frac{2\pi}{\lambda}\mathbf{r}_k^T \mathbf{p}_m \right\} \tag{5.3}$$

where $\mathbf{r}_k = [\cos(\bar{\phi}_k)\sin(\bar{\theta}_k) \; \sin(\bar{\phi}_k)\sin(\bar{\theta}_k) \; \cos(\bar{\theta}_k)]^T$, λ is the wavelength and $\mathbf{p}_m = [x_m \; y_m \; z_m]^T$ is the mth antenna position. The form of the MC matrix $\mathbf{C}$ for arbitrary array structure is given as

$$\mathbf{C} = \begin{pmatrix} c_1 & c_2 & c_3 & \dots & c_M \\ c_2 & c_1 & c_{M+1} & \dots & c_{2M-2} \\ c_3 & c_{M+1} & \ddots & \ddots & \vdots \\ \vdots & \ddots & \ddots & c_1 & c_{\bar{M}} \\ c_M & c_{2M-2} & \dots & c_{\bar{M}} & c_1 \end{pmatrix}. \tag{5.4}$$

The relation between the indices of $\mathbf{C}$ and the coupling coefficients is given explicitly as

$$\mathbf{C}(i,j) = c_m, \; \text{ for } m = \left(M - \frac{1}{2}\right)i - \frac{i^2}{2} + j - M + 1 \tag{5.5}$$

for $i = 1, \dots, M$ and $j = i + 1, \dots, M$. The first coupling coefficient $c_1 = 1$ is assumed without loss of generality [6]. $\{c_m\}_{m=1}^{\bar{M}}$ is the set of distinct MC coefficients and $\bar{M} = \frac{M(M-1)}{2} + 1$.

The effect of MC decreases as the distance between the antenna pairs increases [18]. When this distance is sufficiently large ($d_m > \lambda$ for $m = 2, \dots, \bar{M}$) the effect of MC can be ignored [16, 17]. Here d_m is the inter-element distance for the mth antenna pair. In this study, the coupling coefficients of the antenna pairs with inter-element distance larger than a wavelength are assumed to be zero and only the coefficients of the antenna pairs with $d_m < \lambda$ are considered.

The problem in this study can be described as follows. Given the array output $\mathbf{y}(t_i)$ for $i = 1, \dots, T$, the sensor positions $\mathbf{p}_m$ for $m = 1, \dots, M$ and the number of sources K, the source DOA angles $\{\bar{\Theta}_k\}_{k=1}^K$ and the coupling coefficients $\{c_m\}_{m=2}^{\bar{M}}$ are to be estimated.

In this study, both single and multiple snapshot cases are considered in sequel in the following parts.

5.3 Joint-Sparse Recovery For A Single Snapshot With MC

In this section, the proposed method JSR-SS is introduced for a single snapshot.

5.3.1 DOA Estimation For A Single Snapshot With JSR-SS

The signal model in (5.1) can be written for noise-free case with a single snapshot as

$$\mathbf{y} = \mathbf{CAs} \tag{5.6}$$

where $\mathbf{s} \in \mathbb{R}^N$ is a K-sparse vector, namely, all entries of $\mathbf{s}$ but K are zero. The non-zero entries of $\mathbf{s}$ are equal to $s_k(t_T)$ in (5.1) for $k = 1, \ldots, K$ and $T = 1$. $\mathbf{A} \in \mathbb{C}^{M \times N}$ is the dictionary matrix defined as

$$\mathbf{A} = [\mathbf{A}(\theta_1), \mathbf{A}(\theta_2), \ldots, \mathbf{A}(\theta_{N_\theta})]. \tag{5.7}$$

The number of columns of the dictionary is $N = N_\phi N_\theta$ and $\mathbf{A}(\theta_j)$ is the dictionary matrix for θ_j which is defined as

$$\mathbf{A}(\theta_j) = [\mathbf{a}(\phi_1, \theta_j), \mathbf{a}(\phi_2, \theta_j), \ldots, \mathbf{a}(\phi_{N_\phi}, \theta_j)] \tag{5.8}$$

and $j = 1, \ldots, N_\theta$. The dictionary resolution for azimuth and elevation is $|\phi_i - \phi_{i+1}| = \Delta_\phi$ and $|\theta_j - \theta_{j+1}| = \Delta_\theta$ for $i = 1, \ldots, N_\phi - 1$ and $j = 1, \ldots, N_\theta - 1$ respectively. In order to find $\mathbf{s}$ and $\mathbf{C}$, the following minimization problem can be considered

$$(P_1) \quad \min_{\mathbf{s} \in \mathbb{R}^N, \mathbf{C} \in \mathbb{C}^{M \times M}} ||\mathbf{s}||_0 \ s.t. \ \mathbf{y} = \mathbf{CAs} \tag{5.9}$$

where $||\mathbf{s}||_0 = |\{i : s_i \neq 0\}|$ is the l_0-norm which denotes the number of nonzero elements of $\mathbf{s}$, namely, the support of $\mathbf{s}$. Since the problem P_1 is non-linear due to $\mathbf{CAs}$ which includes both of the unknowns $\mathbf{s}$ and $\mathbf{C}$, it should be modified for an effective solution. In the following part, P_1 is converted to a JSR problem which can be written in linear form. We introduce a joint-sparse vector composed of both signal vector $\mathbf{s}$ and MC coefficients. Furthermore, a new dictionary matrix is defined using the symmetricity of the MC matrix $\mathbf{C}$.

As the first step, $\mathbf{C}$ is written as

$$\mathbf{C} = \sum_{m=1}^{\bar{M}} c_m \mathbf{J}_m \tag{5.10}$$

where $\mathbf{J}_m$ is $M \times M$ matrix whose $(i,j)^{th}$ entry is given as

$$\mathbf{J}_m(i,j) = \begin{cases} 1, & \text{if } \mathbf{C}(i,j) = c_m, \ m = 1,2,\ldots,\bar{M}. \\ 0, & \text{otherwise.} \end{cases} \tag{5.11}$$

Then, $M \times \bar{M}N$ dictionary matrix $\mathbf{D}$ can be defined by stacking $\mathbf{A}$ as

$$\mathbf{D} = [\mathbf{J}_1\mathbf{A}, \mathbf{J}_2\mathbf{A}, \ldots, \mathbf{J}_{\bar{M}}\mathbf{A}]. \tag{5.12}$$

Using (5.11) and (5.12), P_1 can be written in the following form, i.e.,

$$(P_2) \quad \min_{\mathbf{x} \in \mathbb{C}^{\bar{M}N}} ||\mathbf{x}||_0 \ s.t. \ \mathbf{y} = \mathbf{D}\mathbf{x} \tag{5.13}$$

where $\mathbf{x}$ is an $\bar{M}K$-sparse $\bar{M}N \times 1$ vector and

$$\mathbf{x} = \mathbf{c} \otimes \mathbf{s} = [c_1\mathbf{s}^T, c_2\mathbf{s}^T, \ldots, c_{\bar{M}}\mathbf{s}^T]^T = \left[\mathbf{x}^{(1)^T}, \mathbf{x}^{(2)^T}, \ldots, \mathbf{x}^{(\bar{M})^T}\right]^T. \tag{5.14}$$

$\mathbf{c} = [c_1, \ldots, c_{\bar{M}}]^T$ and $\otimes$ denotes the Kronecker product. Since $\mathbf{x}$ is composed of $\bar{M}$ subblocks sharing the same sparsity pattern, (5.13) can be solved effectively by employing joint-sparsity [59]. In this study, $\mathbf{x}$ is said to be K-joint-sparse if $||\mathbf{x}||_{2,0} = K$ where $||\cdot||_{2,0}$ is defined for a vector quantity as follows.

Definition 1 $l_{2,0}$-norm of a *joint-sparse vector* $\mathbf{x}$, which is composed of equal size subblocks $\mathbf{x}^{(m)}$, is defined as

$$||\mathbf{x}||_{2,0} = \sum_{i=1}^{N} \mathcal{I}(||\mathbf{X}[i,:]||_2) \tag{5.15}$$

where $\mathbf{X}[i,:]$ denotes the ith row of $\mathbf{X}$ and $\mathbf{X} = \left[\mathbf{x}^{(1)}, \mathbf{x}^{(2)}, \ldots, \mathbf{x}^{(\bar{M})}\right]$ is an $N \times \bar{M}$ matrix. $\mathcal{I}(\cdot)$ is an indicator function and it is defined as

$$\mathcal{I}(\alpha) = \begin{cases} 0, & \text{if } \alpha = 0 \\ 1, & \text{otherwise.} \end{cases} \tag{5.16}$$

Example 1 Let $\boldsymbol{p} = [p_1, 0, p_2, 0, p_3, 0, p_4, 0, p_5, 0, p_6, 0]^T$ be composed of $\bar{M} = 3$ blocks of size $N = 4$ and $p_i \neq 0$ for $i = 1, \ldots, 6$. Then $\boldsymbol{p}^{(1)} = [p_1, 0, p_2, 0]^T$, $\boldsymbol{p}^{(2)} = [p_3, 0, p_4, 0]^T$, $\boldsymbol{p}^{(3)} = [p_5, 0, p_6, 0]^T$ and $||\boldsymbol{p}||_{2,0}$ is given as

$$||\boldsymbol{p}||_{2,0} = || \left[\sqrt{p_1^2 + p_3^2 + p_5^2}, 0, \sqrt{p_2^2 + p_4^2 + p_6^2}, 0\right]^T ||_0 = 2 \tag{5.17}$$

while $||\boldsymbol{p}||_0 = 6$ since there are two non-zero entries in each subblocks sharing the same index.

Using joint-sparsity, (5.13) can be rewritten as follows

$$(JSP_1) \quad \min_{\mathbf{x} \in \mathbb{C}^{\bar{M}N}} ||\mathbf{x}||_{2,0} \ s.t. \ \mathbf{y} = \mathbf{Dx} \qquad (5.18)$$

where JSP stands for Joint-Sparse Problem. Since the computation of l_0-norm is NP-Hard combinatorial, l_1-norm is usually employed for an equivalent formulation [90]. Hence, $l_{2,0}$-norm is relaxed with $l_{2,1}$-norm. The mixed $l_{2,1}$-norm is defined below.

Definition 2 The mixed $l_{2,1}$-norm considers $\bar{M}$ subblocks of size $N \times 1$ under l_1-norm in a vector of $\bar{M}N \times 1$. Then $||\mathbf{x}||_{2,1}$ is defined as

$$||\mathbf{x}||_{2,1} = \sum_{i=1}^{N} \left(\sum_{m=1}^{\bar{M}} |x_{N(m-1)+i}|^2 \right)^{1/2}. \qquad (5.19)$$

Example 2 *Consider the 12×1 vector $\boldsymbol{p}$ given in the previous example for $\bar{M} = 3$ and $N = 4$. Then $||\boldsymbol{p}||_{2,1}$ is given as*

$$||\boldsymbol{p}||_{2,1} = \sqrt{|p_1|^2 + |p_3|^2 + |p_5|^2} + \sqrt{|p_2|^2 + |p_4|^2 + |p_6|^2}.$$

For noisy observations, joint-sparse recovery problem can be expressed as

$$(JSP_2) \quad \min_{\mathbf{x} \in \mathbb{C}^{\bar{M}N}} ||\mathbf{x}||_{2,1} \ s.t. \ ||\mathbf{y} - \mathbf{Dx}||_2^2 \leq \epsilon^2 \qquad (5.20)$$

where $\mathbf{y} = \mathbf{CAs} + \mathbf{e}$ and the residual is bounded by $\epsilon = \sigma_N \sqrt{M + \gamma \sqrt{2M}}$ [52]. γ is an adjustable parameter which controls the noise power $||\mathbf{e}||_2^2$. Then $||\mathbf{x}||_{2,1}$ can be explicitly given in terms of $\mathbf{s}$ and $\mathbf{c}$ as

$$||\mathbf{x}||_{2,1} = \sum_{i=1}^{N} \left(\sum_{m=1}^{\bar{M}} |c_m s_i|^2 \right)^{1/2}. \qquad (5.21)$$

JSP_2 can be further modified to a more convenient form by moving the inequality constraint to the objective function and the final form of JSR-SS is given as

$$(JSP_3) \quad \min_{\mathbf{x} \in \mathbb{C}^{\bar{M}N}} \mu_S ||\mathbf{x}||_{2,1} + \frac{1}{2} ||\mathbf{y} - \mathbf{Dx}||_2^2 \qquad (5.22)$$

where μ_S is the penalty term which determines the trade-off between the two terms in the problem. A large regularization parameter μ_S enforces the sparsity (i.e. the $l_{2,1}$-norm term) which may lead to wrong estimation results. Similarly, a small value of μ_S

emphasizes the effect of l_2-norm term which may result large number of peaks in the sparse vector. A suitable value for the penalty term is $\sigma_N \sqrt{2 \log \bar{M} N}$ in accordance with [110, Sec. 5.2]. JSP_3 is a convex problem and can be solved effectively by using standard techniques [111]. Once it is solved, the $N \times \bar{M}$ matrix $\hat{\mathbf{X}}$ can be constructed as in Def. 1. Then the $N \times 1$ indicator vector $\tilde{\mathbf{s}}$ can be found as $\tilde{\mathbf{s}} = \mathcal{P}\{\hat{\mathbf{X}}\hat{\mathbf{X}}^H\}$ where $\mathcal{P}\{\cdot\}$ denotes the principal eigenvector operation. Then we can find the source DOA angles from the dictionary terms in $\mathbf{A}$ that correspond to the non-zero entries of $\tilde{\mathbf{s}}$.

5.3.2   Estimation of MC Coefficients From A Single Snapshot

Once the convex problem in (5.22) is solved, the coupling coefficients can be found as $c_m = x_{N(m-1)+i}/s_i$ for $m = 1, \ldots, \bar{M}$ and $i \in \mathbb{I}_{\mathbf{x}}$ which is the set of indices of non-zero elements in $\mathbf{x}$. This is a suboptimum method for finding the coupling coefficients since there exist K many solutions of c_m for $i \in \mathbb{I}_{\mathbf{x}}$. An alternative and better solution is to find $\hat{\mathbf{x}}$ and $\hat{\mathbf{s}}$ from (5.22), then obtain a least-square solution of $\mathbf{c}$ from a cost function. In this case, $\mathbf{c}$ is found by minimizing the cost function $J(\mathbf{c})$, i.e.,

$$J(\mathbf{c}) = ||\mathbf{y} - \sum_{m=1}^{\bar{M}} c_m \mathbf{J}_m \mathbf{A}\hat{\mathbf{s}}||_2^2 = \mathbf{y}^H \mathbf{y}$$

$$-\mathbf{y}^H \sum_{m_1=1}^{\bar{M}} c_{m_1} \mathbf{J}_{m_1} \mathbf{A}\hat{\mathbf{s}} - \sum_{m_2=1}^{\bar{M}} c_{m_2}^* \hat{\mathbf{s}}^H \mathbf{A}^H \mathbf{J}_{m_2}^H \mathbf{y}$$

$$+ \sum_{m_1=1}^{\bar{M}} \sum_{m_2=1}^{\bar{M}} c_{m_1} c_{m_2}^* \hat{\mathbf{s}}^H \mathbf{A}^H \mathbf{J}_{m_2}^H \mathbf{J}_{m_1} \mathbf{A}\hat{\mathbf{s}}. \tag{5.23}$$

If the derivative of $J(\mathbf{c})$ with respect to $c_{m_2}^*$ is considered and equated to zero, the following expression is obtained, i.e.,

$$\sum_{m_1=1}^{\bar{M}} \sum_{m_2=1}^{\bar{M}} c_{m_1} \hat{\mathbf{s}}^H \mathbf{A}^H \mathbf{J}_{m_2}^H \mathbf{J}_{m_1} \mathbf{A}\hat{\mathbf{s}} = \sum_{m_2=1}^{\bar{M}} \hat{\mathbf{s}}^H \mathbf{A}^H \mathbf{J}_{m_2}^H \mathbf{y}. \tag{5.24}$$

Above equation can be written as a linear set of equations, i.e.,

$$\mathbf{A}_c \mathbf{c} = \mathbf{b}_c \tag{5.25}$$

where the elements of $\mathbf{A}_c \in \mathbb{C}^{\bar{M} \times \bar{M}}$ and $\mathbf{b}_c \in \mathbb{C}^{\bar{M}}$ are known and expressed as

$$
\begin{aligned}
A_c(m_2, m_1) &= \hat{\mathbf{s}}^H \mathbf{A}^H \mathbf{J}_{m_2}^H \mathbf{J}_{m_1} \mathbf{A} \hat{\mathbf{s}} \\
b_c(m_2) &= \hat{\mathbf{s}}^H \mathbf{A}^H \mathbf{J}_{m_2}^H \mathbf{y}, \quad m_1, m_2 = 1, \ldots, \bar{M}.
\end{aligned}
\tag{5.26}
$$

Then the MC coefficients can be found as $\mathbf{c} = \mathbf{A}_c^{-1} \mathbf{b}_c$.

5.4 Joint-Sparse Recovery For Multiple Snapshots With MC

In this part, the problem defined in Sec. 5.3 is solved for multiple snapshots. When there are multiple noisy snapshots, (5.6) can be written in matrix form as

$$
\mathbf{Y} = \mathbf{CAS} + \mathbf{E}
\tag{5.27}
$$

where $\mathbf{Y} = [\mathbf{y}(t_1), \mathbf{y}(t_2), \ldots, \mathbf{y}(t_T)]$ is the $M \times T$ observation matrix and T is the number of snapshots. $\mathbf{S} = [\mathbf{s}(t_1), \mathbf{s}(t_2), \ldots, \mathbf{s}(t_T)]$ is an $N \times T$ matrix and $\mathbf{E} = [\mathbf{e}(t_1), \mathbf{e}(t_2), \ldots, \mathbf{e}(t_T)]$.

Since $\mathbf{s}(t_i)$ is a K-sparse vector for $i = 1, \ldots, T$, there are KT non-zero entries of $\mathbf{S}$. The number of non-zero elements of a matrix is obtained by l_0-norm as $||\mathbf{S}||_0 = |\{i, j : S_{i,j} \neq 0\}|$. Note that only K rows of $\mathbf{S}$ are non-zero. This property is used to exploit the joint-sparsity of $\mathbf{S}$. $\mathbf{S}$ is said to be K-joint-sparse matrix if $||\mathbf{S}||_{2,0} = K$. The definition of $l_{2,0}$-norm for a matrix is given below [60].

Definition 3 $l_{2,0}$-norm of an $N \times T$ *joint-sparse matrix* $\mathbf{S}$ is defined as

$$
||\mathbf{S}||_{2,0} = \sum_{i=1}^{N} \mathcal{I}(||\mathbf{S}[i, :]||_2)
\tag{5.28}
$$

where $\mathbf{S}[i, :]$ denotes the ith row of $\mathbf{S}$ and $\mathcal{I}(\cdot)$ is as defined in 5.16.

Example 3 *Consider a 6×3 matrix $\boldsymbol{P}$ as*

$$\boldsymbol{P} = \begin{bmatrix} a_1 & a_2 & a_3 \\ b_1 & b_2 & b_3 \\ c_1 & c_2 & c_3 \\ d_1 & d_2 & d_3 \\ e_1 & e_2 & e_3 \\ f_1 & f_2 & f_3 \end{bmatrix} \tag{5.29}$$

where $\{a_i, b_i, d_i, f_i\}_{i=1}^3 \neq 0$ and $\{c_i, e_i\}_{i=1}^3 = 0$. Then $||\boldsymbol{P}||_{2,0} = 4$ whereas $||\boldsymbol{P}||_0 = 12$.

When the joint-sparsity is considered, the optimization problem can be written as follows

$$(JSP_4) \quad \min_{\mathbf{S} \in \mathbb{R}^{N \times T}, \mathbf{C} \in \mathbb{C}^{M \times M}} ||\mathbf{S}||_{2,0} \ s.t. \ ||\mathbf{Y} - \mathbf{CAS}||_F^2 \leq \bar{\epsilon}^2.$$

In JSP_4, the constraint is non-linear and $l_{2,0}$-norm is not convex. Furthermore, computational complexity increases with T. It is possible to decrease the computational complexity through singular value decomposition (SVD) [105]. Hence we first express the problem in an efficient form. Then DOA and MC parameters are considered in a composite matrix and $l_{2,0}$-norm is relaxed to obtain an effective solution. Therefore we first consider the SVD of $\mathbf{Y}$ as

$$\mathbf{Y} = \mathbf{U\Sigma V}^H \tag{5.30}$$

where $\mathbf{U}$ and $\mathbf{V}$ are the left and right singular vector matrices of $\mathbf{Y}$ respectively. $\mathbf{\Sigma}$ is an $M \times T$ matrix composed of the singular values of $\mathbf{Y}$. Since the first K singular values are dominant in $\mathbf{\Sigma}$, the $M \times K$ reduced matrix $\mathbf{Y}_{SV}$ is defined as

$$\mathbf{Y}_{SV} = \mathbf{U\Sigma L} = \mathbf{YVL} \tag{5.31}$$

where $\mathbf{L}$ is a $T \times K$ matrix and defined as $\mathbf{L} = [\mathbf{I}_K \ \mathbf{0}]^T$. $\mathbf{I}_K$ is $K \times K$ identity matrix and $\mathbf{0}$ is $(T - K) \times K$ matrix of zeros. Then $\mathbf{Y}_{SV}$ is given as

$$\mathbf{Y}_{SV} = \mathbf{CAS}_{SV} + \mathbf{E}_{SV} \tag{5.32}$$

where $\mathbf{S}_{SV} = \mathbf{SVL}$ and $\mathbf{E}_{SV} = \mathbf{EVL}$. Note that $\mathbf{S}_{SV}$ and $\mathbf{S}$ have the same joint-sparsity.

The l_1-SVD method proposed in [105] considers the sparse recovery problem when there is no MC in the array model, i.e., $\mathbf{Y}_{SV} = \mathbf{A}\mathbf{S}_{SV} + \mathbf{E}_{SV}$. In the following part, we will develop a JSR algorithm to solve the problem in case of multiple snapshots and MC.

5.4.1 DOA Estimation For Multiple Snapshots With JSR-MS

In this section, a similar approach as in JSR-SS is followed and a JSR algorithm is presented for multiple snapshots. In order to write JSP_4 in linear form, (5.32) is rewritten in the following form using joint-sparsity, i.e.,

$$\mathbf{Y}_{SV} = \mathbf{D}\mathbf{X}_{SV} + \mathbf{E}_{SV} \tag{5.33}$$

where $\mathbf{D}$ is the same dictionary matrix as in (5.12). $\mathbf{X}_{SV}$ is an $\bar{M}N \times K$ joint-block-sparse matrix defined as

$$\mathbf{X}_{SV} = \mathbf{c} \otimes \mathbf{S}_{SV} = \begin{bmatrix} c_1\mathbf{S}_{SV} \\ c_2\mathbf{S}_{SV} \\ \vdots \\ c_{\bar{M}}\mathbf{S}_{SV} \end{bmatrix} = \begin{bmatrix} \mathbf{X}_{SV}^{(1)} \\ \mathbf{X}_{SV}^{(2)} \\ \vdots \\ \mathbf{X}_{SV}^{(\bar{M})} \end{bmatrix}. \tag{5.34}$$

Note that $\mathbf{X}_{SV}$ is composed of $\bar{M}$ subblock matrices. In Sec. 5.3.1, joint-sparsity is employed for vector quantities which are composed of subblocks with the same sparsity pattern. In this part, we define joint-block-sparsity for $\mathbf{X}_{SV}$ using triple mixed $l_{2,2,0}$-norm which exploits the joint-sparsity in both subblocks and columns of matrix $\mathbf{X}_{SV}$. In other words, $l_{2,2,0}$-norm is the mixture of $l_{2,0}$-norms defined for both vector and matrix quantities. The definition of $l_{2,2,0}$-norm is given as follows.

Definition 4 $l_{2,2,0}$-norm of an $\bar{M}N \times K$ *joint-block-sparse* matrix $\mathbf{X}_{SV}$, composed of $\bar{M}$ subblocks of size $N \times K$, is defined as

$$||\mathbf{X}_{SV}||_{2,2,0} = \sum_{i=1}^{N} \mathcal{I}(||\bar{\mathbf{X}}_{SV}[i,:]||_2) \tag{5.35}$$

where $\bar{\mathbf{X}}_{SV} = \left[\mathbf{X}_{SV}^{(1)}, \mathbf{X}_{SV}^{(2)}, \ldots, \mathbf{X}_{SV}^{(\bar{M})}\right]$ is an $N \times \bar{M}K$ matrix composed of the subblocks of $\mathbf{X}_{SV}$.

70

Example 4 *Consider the matrix $\boldsymbol{P}$ in Example 3 for $\{a_i, c_i, e_i\}_{i=1}^3 \neq 0$ and $\{b_i, d_i, f_i\}_{i=1}^3 = 0$ with $\bar{M} = 3$ and $N = 2$. Then $||\boldsymbol{P}||_{2,2,0} = 1$ while $||\boldsymbol{P}||_{2,0} = 3$ and $||\boldsymbol{P}||_0 = 9$.*

In order to solve the problem in JSP_4 using joint-block-sparsity, $l_{2,2,0}$-norm should be used. Since $l_{2,2,0}$-norm is not convex, it is relaxed to $l_{2,2,1}$-norm which is defined below.

Definition 5 Triple mixed $l_{2,2,1}$-norm considers $\bar{M}$ blocks of $N \times K$ matrices in l_1-norm and $||\mathbf{X}_{SV}||_{2,2,1}$ is defined as

$$||\mathbf{X}_{SV}||_{2,2,1} = \sum_{i=1}^{N} \left(\sum_{m=1}^{\bar{M}} \sum_{k=1}^{K} |\mathbf{X}_{SV}(N(m-1)+i,k)|^2 \right)^{1/2}$$

where $\mathbf{X}_{SV}(i,j)$ is the $(i,j)^{th}$ entry of $\mathbf{X}_{SV}$.

Example 5 *Consider the matrix $\boldsymbol{P}$ in Example 3. Then $l_{2,2,1}$-norm of $\boldsymbol{P}$ for $\bar{M} = 2$ and $N = 3$ is given as*

$$||\boldsymbol{P}||_{2,2,1} = \sqrt{|a_1|^2 + |a_2|^2 + |a_3|^2 + |d_1|^2 + |d_2|^2 + |d_3|^2}$$
$$+\sqrt{|b_1|^2 + |b_2|^2 + |b_3|^2 + |e_1|^2 + |e_2|^2 + |e_3|^2}$$
$$+\sqrt{|c_1|^2 + |c_2|^2 + |c_3|^2 + |f_1|^2 + |f_2|^2 + |f_3|^2}.$$

The final form of the joint DOA and MC estimation problem for multiple snapshots, i.e., JSR-MS, can be written similar to JSP_3 as

$$(JSP_5) \min_{\mathbf{X}_{SV} \in \mathbb{C}^{\bar{M}N \times K}} \mu_M ||\mathbf{X}_{SV}||_{2,2,1} + \frac{1}{2} ||\mathbf{Y}_{SV} - \mathbf{D}\mathbf{X}_{SV}||_F^2$$

where μ_M is the regularization parameter that balances the trade-off between the normed terms. $||\mathbf{X}_{SV}||_{2,2,1}$ is explicitly given as

$$||\mathbf{X}_{SV}||_{2,2,1} = \sum_{i=1}^{N} \left(\sum_{m=1}^{\bar{M}} \sum_{k=1}^{K} |c_m s_i^{SV}(k)|^2 \right)^{1/2}. \tag{5.36}$$

$s_i^{SV}(k)$ is the $(i,k)^{th}$ entry of $N \times K$ matrix $\mathbf{S}_{SV}$.

In JSP_5, joint-sparse recovery problem is given in case of multiple snapshots. JSP_5 is a convex problem and can be solved effectively similar to JSP_3 with convex problem solvers [111]. Once JSP_5 is solved, the $\bar{M}N \times K$ matrix $\hat{\mathbf{X}}_{SV}$ can be obtained.

Then the $N \times \bar{M}K$ matrix $\hat{\bar{\mathbf{X}}}_{SV}$ can be constructed by stacking the subblocks of $\hat{\mathbf{X}}_{SV}$ as in Def. 4. In order to find the DOA angle estimates, the $N \times 1$ indicator vector $\tilde{\mathbf{s}}$ can be found as $\tilde{\mathbf{s}} = \mathcal{P}\{\hat{\bar{\mathbf{X}}}_{SV}\hat{\bar{\mathbf{X}}}_{SV}^H\}$. Then the estimates of the source DOA angles are found from the indices of $M \times N$ dictionary $\mathbf{A}$ corresponding to the non-zero entries of $\tilde{\mathbf{s}}$.

5.4.2 Estimation of MC Coefficients From Multiple Snapshots

In Sec. 5.3.2, MC coefficients are estimated for a single snapshot. In this part, MC coefficients are estimated using multiple snapshots where the array covariance matrix is utilized. The covariance matrix of the array output can be written as

$$\mathbf{R}_y = \mathbf{YY}^H = \mathbf{U\Lambda U}^H. \tag{5.37}$$

$\mathbf{U} = [\mathbf{U}_s \mathbf{U}_n]$ is the eigenvector matrix where $\mathbf{U}_s$ and $\mathbf{U}_n$ are signal and noise subspace eigenvector matrices respectively. $\mathbf{\Lambda}$ is a diagonal matrix composed of the eigenvalues of $\mathbf{R}_y$.

In the presence of mutual coupling, the true steering matrix becomes $\mathbf{C}\bar{\mathbf{A}}$ and the columns of signal subspace eigenvector matrix $\mathbf{U}_s$ span the same space with $\mathbf{Ca}(\bar{\Theta}_k)$ for $k = 1, \ldots, K$. Since the signal and noise subspaces are orthogonal [3], i.e., $||\mathbf{U}_n^H\mathbf{U}_s||_F^2 = 0$, the following can be written, i.e.,

$$||\mathbf{U}_n^H\mathbf{Ca}(\bar{\Theta}_k)||_F^2 = 0, \quad k = 1, \ldots, K. \tag{5.38}$$

In order to estimate the MC coefficients for arbitrary array structure, we first introduce the following lemma.

Lemma 1 Given the $M \times 1$ steering vector $\mathbf{a}(\bar{\Theta}_k)$ of an arbitrary array, the relation between the $M \times M$ symmetric matrix $\mathbf{C}$ and $\bar{M} \times 1$ vector $\mathbf{c}$ is written as

$$\mathbf{T}_k\mathbf{c} = \mathbf{Ca}(\bar{\Theta}_k), \quad k = 1, \ldots, K \tag{5.39}$$

where the transformation matrix $\mathbf{T}_k$ is given as

$$\mathbf{T}_k = [\boldsymbol{\tau}_1^k, \ldots, \boldsymbol{\tau}_{\bar{M}}^k]$$
$$\boldsymbol{\tau}_m^k = \mathbf{J}_m\mathbf{a}(\bar{\Theta}_k), \quad k = 1, \ldots, K \tag{5.40}$$

and $\mathbf{J}_m$ is defined as in (5.11).

Proof: If we consider the expression in (5.10), then the lemma can be easily proven by writing (5.39) as

$$\mathbf{T}_k\mathbf{c} = \sum_{m=1}^{\bar{M}} \mathbf{J}_m c_m \mathbf{a}(\bar{\Theta}_k), \quad k = 1, \ldots, K$$

$$= \left[\mathbf{J}_1\mathbf{a}(\bar{\Theta}_k), \mathbf{J}_2\mathbf{a}(\bar{\Theta}_k), \ldots, \mathbf{J}_{\bar{M}}\mathbf{a}(\bar{\Theta}_k)\right] \begin{bmatrix} c_1 \\ c_2 \\ \vdots \\ c_{\bar{M}} \end{bmatrix}$$

$$= [\boldsymbol{\tau}_1^k, \ldots, \boldsymbol{\tau}_{\bar{M}}^k]\mathbf{c} \tag{5.41}$$

where $\left\{\boldsymbol{\tau}_m^k\right\}_{m=1}^{\bar{M}}$ are the columns of $M \times \bar{M}$ transformation matrix $\mathbf{T}_k$. $\qquad\square$

Once the DOA angle estimates $\{\hat{\Theta}_k\}_{k=1}^K$ are found by solving JSP_5, the transformation matrix defined in (5.40) is used and the following cost function [6] is obtained, i.e.,

$$\bar{J}(\mathbf{c}) = \sum_{k=1}^K \mathbf{a}(\hat{\Theta}_k)^H \mathbf{C}^H \mathbf{U}_n \mathbf{U}_n^H \mathbf{C} \mathbf{a}(\hat{\Theta}_k)$$

$$= \mathbf{c}\left(\sum_{k=1}^K \mathbf{T}_k^H \mathbf{U}_n \mathbf{U}_n^H \mathbf{T}_k\right)\mathbf{c}. \tag{5.42}$$

In order to obtain a nontrivial solution, a constraint $\mathbf{w}^T\mathbf{c} = u$ is added to the problem. Hence the following problem is obtained, i.e.,

$$\min_{\mathbf{c} \in \mathbb{C}^{\bar{M} \times 1}} \bar{J}(\mathbf{c}) \; s.t. \; \mathbf{w}^T\mathbf{c} = u. \tag{5.43}$$

The closed-form solution of $\mathbf{c}$ is given as

$$\hat{\mathbf{c}} = \mathbf{G}^{-1}\mathbf{w}\left(\mathbf{w}^T\mathbf{G}^{-1}\mathbf{w}\right)^{-1}u \tag{5.44}$$

where

$$\mathbf{G} = \sum_{k=1}^K \mathbf{T}_k^H \mathbf{U}_n \mathbf{U}_n^H \mathbf{T}_k \tag{5.45}$$

and $\mathbf{w}^T\mathbf{c} = u$ is the constraint equation. A possible choice for $\mathbf{w} \in \mathbb{C}^{\bar{M} \times 1}$ is $\mathbf{w} = [1, 0, \ldots, 0]^T$ and $u = 1$ [6].

73

5.5 Feasibility of the Problem

In this section, the feasibility conditions of the considered problem are discussed in two parts. Firstly, the uniqueness condition for DOA estimation problem is introduced. Then the MC estimation problem is investigated.

5.5.1 Uniqueness for DOA Estimation Problem

Since the considered problem in (5.13), i.e., $\mathbf{y} = \mathbf{As}$ is underdetermined ($M \ll N$), there are infinitely many solutions in general. However, if the solution of the problem $\mathbf{s}$ is sparse, a unique solution can be obtained. In the following, both sparse and joint-sparse recovery cases are examined in sequel.

5.5.1.1 Sparse Recovery Case

Theorem 1 *If $\mathbf{y} = \mathbf{As}$ has a solution satisfying $||\mathbf{s}||_0 = K < spark(\mathbf{A})/2$, then $\mathbf{s}$ is the unique solution where $spark(\mathbf{A})$ is defined as the minimum number of linearly dependent columns of $\mathbf{A}$.*

Proof: Proof is by contradiction [112, 113]. Firstly, assume that there exists at most one $\mathbf{s}$ where $||\mathbf{s}||_0 = K$ and $spark(\mathbf{A}) \le 2K$. Then suppose that there exists an $\mathbf{h}$ with $||\mathbf{h}||_0 = 2K$ and $\mathbf{h} \in \text{Null}\{\mathbf{A}\}$ i.e. the null space of $\mathbf{A}$. This means that there exist some set of at most $2K$ columns that are linearly dependent. Since $||\mathbf{h}||_0 = 2K$, we can write $\mathbf{h} = \mathbf{s} - \mathbf{s}'$ for $||\mathbf{s}||_0 = ||\mathbf{s}'||_0 = K$ with $\mathbf{s} \ne \mathbf{s}'$. Using $\mathbf{h} \in \text{Null}\{\mathbf{A}\}$, we have $\mathbf{A}(\mathbf{s}-\mathbf{s})'$, in other words, $\mathbf{As} = \mathbf{As}'$. This leads to the fact that there exist two solutions $\mathbf{s}$ and $\mathbf{s}'$. However, this contradicts our assumption that there exists at most one $\mathbf{s}$ with $||\mathbf{s}||_0 = K$. Therefore we must have $spark(\mathbf{A}) > 2K$. Since $spark(\mathbf{A}) \le M + 1$, $K < spark(\mathbf{A})/2$ leads to the final condition $2K < M$. Then we can conclude that the uniqueness condition for sparse recovery is $2K < M$.

5.5.1.2   Joint-sparse Recovery Case

In order to investigate the uniqueness for joint-sparsity, we first define the isometry principle for the considered problem. The restricted isometry property for joint-sparse case (JS-RIP) is investigated in [59] for $2K$-sparse signals. In this study, $\bar{M}K$-sparse signal $\mathbf{x}$ is said to be K-joint-sparse if $||\mathbf{x}||_{2,0} = K$. Then JS-RIP is defined as follows.

Definition 6 The dictionary matrix $\mathbf{D}$ is said to obey JS-RIP with joint-sparsity level K, if there exists $\delta_K \in [0, 1)$ for all K-joint-sparse ($\bar{M}K$-sparse) signals $\mathbf{x} \in \mathbb{C}^{\bar{M}N}$ such that

$$(1 - \delta_K)||\mathbf{x}||_2^2 \leq ||\mathbf{Dx}||_2^2 \leq (1 + \delta_K)||\mathbf{x}||_2^2 \tag{5.46}$$

holds for the JS-RIP constant δ_K.

The JS-RIP constant δ_K can be found as follows [114]

$$\min_{\delta_K \in [0,1)} \delta_K \, s.t. \, (1 - \delta_K)||\mathbf{x}||_2^2 \leq ||\mathbf{Dx}||_2^2 \leq (1 + \delta_K)||\mathbf{x}||_2^2 \tag{5.47}$$

The uniqueness of the solution for the problem in JSP_1 can be treated in a similar manner as in [59]. In our case, the problem involves the mixed norms of source vector and MC coefficients and should be treated accordingly. The following theorem describes the uniqueness property.

Theorem 2 Let $\hat{\mathbf{s}}$ and $\hat{\mathbf{c}}$ be the solution to JSP_1 problem. If the matrix $\mathbf{D}$ obeys JS-RIP with $\delta_{2K} < 1$, then the solution is unique.

Proof: Let $\hat{\mathbf{x}}$ be the solution to JSP_1 in (5.18) with

$$\hat{\mathbf{x}} = [\hat{\mathbf{s}}^T, \hat{c}_2\hat{\mathbf{s}}^T, \hat{c}_3\hat{\mathbf{s}}^T, \ldots, \hat{c}_{\bar{M}}\hat{\mathbf{s}}^T]^T \tag{5.48}$$

Then, we can say that $||\hat{\mathbf{x}}||_{2,0} \leq ||\mathbf{x}||_{2,0} \leq K$ since both $\hat{\mathbf{x}}$ and $\mathbf{x}$ are the solution [115]. Using the triangle inequality, the difference is bounded by $2K$ as

$$||\mathbf{x} - \hat{\mathbf{x}}||_{2,0} \leq 2K. \tag{5.49}$$

Since both $\hat{\mathbf{x}}$ and $\mathbf{x}$ solve JSP_1 with equality, then $\mathbf{y} = \mathbf{D}\hat{\mathbf{x}} = \mathbf{D}\mathbf{x}$ which results $\mathbf{D}(\mathbf{x} - \hat{\mathbf{x}}) = 0$. We can use (5.49) in JS-RIP as follows

$$(1 - \delta_{2K})||\mathbf{x} - \hat{\mathbf{x}}||_2^2 \leq ||\mathbf{D}(\mathbf{x} - \hat{\mathbf{x}})||_2^2 = 0. \tag{5.50}$$

Then we can see that $||\mathbf{x} - \hat{\mathbf{x}}||_2^2 = 0$ since $\delta_{2K} < 1$ which concludes the proof. $\qquad\square$

In case of multiple snapshots, JS-RIP can be written as follows

$$(1 - \delta_K^{(M)})||\mathbf{X}||_F^2 \leq ||\mathbf{D}\mathbf{X}||_F^2 \leq (1 + \delta_K^{(M)})||\mathbf{X}||_F^2 \tag{5.51}$$

where $\mathbf{X}$ is a K-joint-block-sparse matrix defined in (5.34). $\delta_K^{(M)}$ is the restricted isometry constant for multiple snapshot case and it can be calculated as in [116]. Further information about the uniqueness of the solution in case of multiple snapshots can be found in the literature for noiseless [117] and noisy scenario [116].

5.5.2 Uniqueness for MC Coefficient Estimation for A Single Snapshot

In case of a single snapshot, the MC coefficients are estimated from a linear set of equations in least-square sense as in (5.26). To obtain a unique solution for MC coefficient estimation, (5.26) should be well-defined. Therefore, the solution is unique if $\bar{M} \leq M$ is satisfied where $\bar{M}$ is the number of coupling coefficients.

5.5.3 Uniqueness for MC Coefficient Estimation for Multiple Snapshots

In order to estimate the MC coefficients in multiple snapshot scenario, the orthogonality of signal and noise subspaces is used as in (5.44). The solution is unique if $\mathbf{G}$ in (5.44) is invertible that is only possible if

$$\text{rank}\{\mathbf{G}\} \leq M - K \tag{5.52}$$

is satisfied where $\text{rank}\{\cdot\}$ is the matrix rank operation. Hence the uniqueness condition is

$$\bar{M} \leq M - K. \tag{5.53}$$

5.6 Performance of The Joint-Sparse Recovery With MC

In this part, the performance bound of the proposed JSR algorithm is given in the following theorem.

Theorem 3 Let $\mathbf{y} = \mathbf{Dx} + \mathbf{e}$ be the noisy measurement of $\bar{M}K$-sparse $\mathbf{x}$, and $\hat{\mathbf{x}}$ is the solution to JSP_2 in (5.20). If $\mathbf{D}$ satisfies JS-RIP with $\delta_{2K} < \sqrt{2} - 1$, then the reconstruction error $||\hat{\mathbf{x}} - \mathbf{x}||_2$ is bounded as follows

$$||\hat{\mathbf{x}} - \mathbf{x}||_2 \leq C_0\epsilon + C_1||\mathbf{x} - (\mathbf{x})_K||_{2,1} \tag{5.54}$$

where $(\mathbf{x})_K$ is the best K-joint-sparse approximation of $\mathbf{x}$ and

$$C_0 = \frac{4\sqrt{1 + \delta_{2K}}}{1 - (1 + \sqrt{2})\delta_{2K}}$$
$$C_1 = \frac{2(1 - \delta_{2K})(\bar{M}K)^{-1/2}}{1 - (1 + \sqrt{2})\delta_{2K}}. \tag{5.55}$$

Proof: The proof is similar to the one presented in [90] where the performance bound is considered for K-sparse vectors. For K-joint-sparse ($\bar{M}K$-sparse) signals that are considered in this work, the bound can be obtained by replacing K with $\bar{M}K$ in [90, Theorem 1.2]. □

5.7 Simulation Results

In this section, the proposed methods, JSR-SS and JSR-MS are evaluated by several experiments. The proposed approaches are compared with both conventional CS methods (Basis Pursuit De-noising (BPDN) [110], Orthogonal Matching Pursuit (OMP) [118], Modified OMP (MOMP) [117], which is the multiple snapshots version of OMP) and subspace-based methods such as the MUSIC [3] algorithm with and without known MC as well as the unconditional Cramer-Rao lower bound (CRB) [6]. Note that the MUSIC algorithm with known MC (MUSIC w/ MC) corresponds to the case that the MC matrix is perfectly known and used in the MUSIC algorithm [28]. In the first part, the simulation results are presented for the scenario where the sources and antenna array are in the same plane in order to have a comparison with
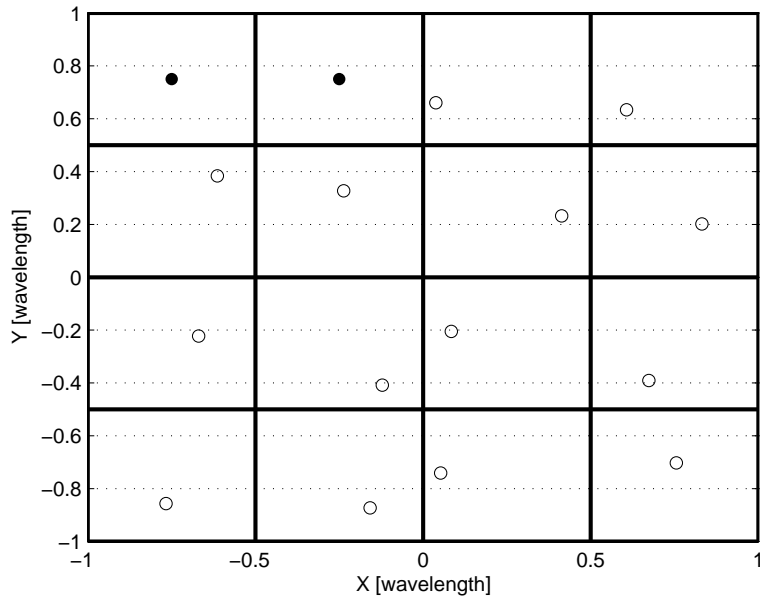
Figure 5.1: The placement of the antennas in the array for a single realization. Dot: the positions of the fixed antennas, Circle: the positions of the randomly changing antennas.

the previous studies [32, 48–50]. These are 1-D DOA and MC coefficient estimation results. In the second part, a DF scenario where the sources are located with different elevation angles is considered. In this case, 2-D DOA and MC coefficient estimation results are presented. In the third scenario, a DF scenario is considered where the array data is corrupted by gain/phase mismatches (GPM) instead of MC. In this scenario, 1-D DOA and GPM parameter estimation results are presented.

Throughout the simulations, three sources located at $32.375°$, $50.714°$ and $75.215°$ in azimuth plane are considered. The elevation angle is assumed to be $90°$ if the sources and the antenna array are located in the same plane. Otherwise, the elevation angles of the sources are selected as $43.251°$, $52.852°$ and $62.734°$ respectively. In order to deal with the off-grid target locations, the dictionary matrix $\mathbf{A}$ is constructed with a coarse resolution, i.e., $\Delta_\phi = 3°$, then multi-resolution grid refinement [105, Sec. 6] is used for all the algorithms. Note that the conventional CS algorithms use the dictionary matrix $\mathbf{A}$ whereas the new dictionary matrix $\mathbf{D}$ is used for the proposed approaches, namely, JSR-SS and JSR-MS respectively. The regularization parameters, μ_S and μ_M are selected as described in [110, Sec. 5.2]. 100 Monte Carlo trials are done for

each experiment. In each trial, the positions of the antennas in the array are updated. There are $M = 16$ antennas positioned randomly in the xy-plane. The positions of the antennas (x_m, y_m) are sampled from a uniform distribution and $x_m \in [-\lambda, \lambda]$, $y_m \in [-\lambda, \lambda]$ and $z_m = 0$ for $m = 1, \ldots, M$. In order to avoid from a dense antenna positioning, each antenna is assumed to be placed randomly in a box in the xy-plane. The xy-plane is divided into $M = 16$ boxes as shown in Fig. 5.1 where a single realization for the positions of the antennas is presented. The position of the first two antennas are fixed with a half wavelength spacing, namely $(x_1, y_1) = (\frac{-3\lambda}{4}, \frac{3\lambda}{4})$ and $(x_2, y_2) = (\frac{-\lambda}{4}, \frac{3\lambda}{4})$. While this is not required for the proposed approaches, this selection is used to avoid spatial aliasing. The other antennas are distributed such that there is a single antenna in each box.

In order to generate the MC matrix, a similar approach in [6] and [50] is followed where MC coefficients are selected randomly based on the distance between antennas. Note that it is assumed that there are at most M unknown coupling coefficients so that the problem in (5.26) is well-posed. The coupling coefficients corresponding to the antenna pairs with $d_m > \lambda$ are assumed to be zero [16, 17]. The gain and the phase terms of MC coefficients are selected as $c_m = c_m^G \exp\left(j c_m^P\right)$ where $c_m^G \sim \mathcal{N}(\frac{\bar{d}_m}{2}, \left(\frac{\bar{d}_m}{20}\right)^2)$ and $c_m^P \sim \mathcal{N}(0, \left(\frac{\pi}{18}\right)^2)$ for $m = 2, \ldots, \bar{M}$ respectively. Note that $c_m^G = 1$ and $c_m^P = 0$ for $m = 1$. $\bar{\mathbf{d}} = [\bar{d}_2, \ldots, \bar{d}_{\bar{M}}] = \frac{\mathbf{d}}{||\mathbf{d}||_\infty}$ is $(\bar{M} - 1) \times 1$ vector composed of the normalized distances. Hence, the coupling coefficient, c_m, will be close to 1 in magnitude as $|\bar{d}_m| \longrightarrow 0$ and it will be close to 0 as $|\bar{d}_m| \longrightarrow 1$.

5.7.1 Scenario 1: 1-D DOA and MC Coefficient Estimation

In this scenario, the sources and antenna array are assumed to be in the same plane. In Fig. 5.2, DOA estimation performance of the algorithms is presented for a single snapshot. As it is seen, JSR-SS asymptotically follows the CRB while the other algorithms do not give accurate estimation results. The MUSIC algorithm also fails due to rank-deficiency. While BPDN and OMP are very effective algorithms for MC-free measurements, their performance is not satisfactory when there is MC.

We present the multiple snapshot DOA estimation performance of the JSR-MS in Fig. 5.3 for different SNR levels. As it is seen, JSR-MS follows the CRB while the
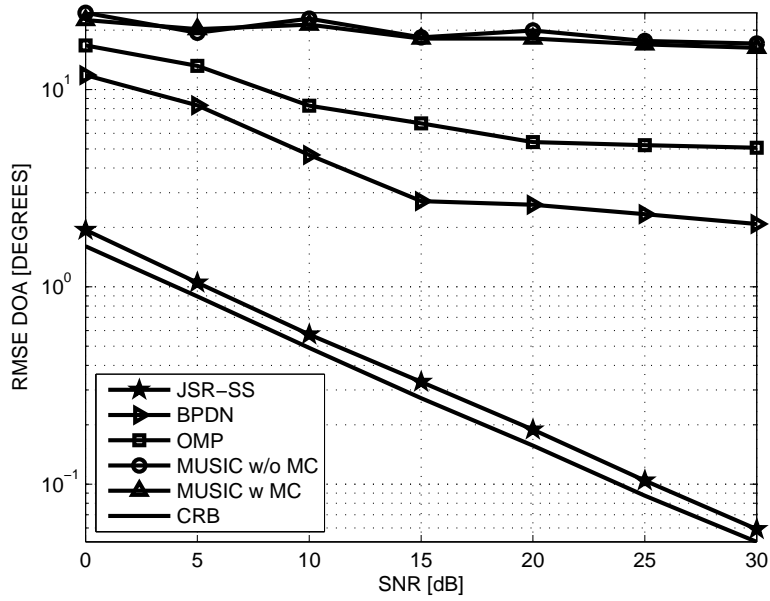
Figure 5.2: 1-D DOA estimation performance for a single snapshot, $T = 1$.
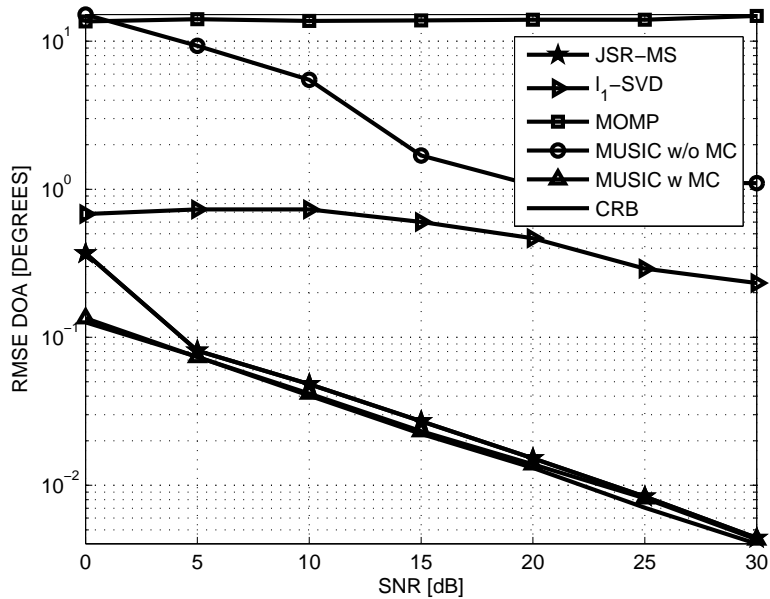
Figure 5.3: 1-D DOA estimation performance for multiple snapshots, $T = 100$.

other algorithms do not perform well except MUSIC with known MC coefficients. When the MC is unknown, MUSIC does not perform well. The other CS algorithms, l_1-SVD and MOMP cannot achieve good performance due to MC.

In Fig. 5.4a, root mean square error (RMSE) for the gain and phase term of the MC coefficients is presented for single snapshot case. Note that the phase estimates

are given in radians. JSR-SS has significantly better performance compared to the alternative methods. While JSR-SS performs better for gain estimates, the margin between JSR-SS and the CRB is larger for phase estimation.

In Fig. 5.4b, RMSE for the gain and the phase term of the MC coefficients is presented for multiple snapshot case. As it is seen, JSR-MS achieves better estimation performance in comparison to the other algorithms.

Since the previous approaches, which involve MC mitigation, require fixed array geometries [15, 107, 108], the proposed method is evaluated in a ULA with $M = 16$ antennas and compared with [107] and [108]. The distance between antennas is $\lambda/2$ and the number of snapshots is $T = 200$. There is a single coupling coefficient and $\bar{M} = 2$. The results are shown in Fig. 5.5. As it is seen, JSR-MS performs better than the other algorithms including the methods in [107] (Dai et.al.) and [108] (SBAC) where MC effect is taken into account. The disadvantage of [107] is array shrinkage where some of the antenna outputs are discarded in order to obtain a special MC matrix in the array model. SBAC is an expectation-maximization algorithm which iteratively estimates the MC coefficients, source signals and noise variance. While SBAC has similar estimation results with JSR-MS for SNR<15dB, it has a certain performance loss after SNR=15dB and its performance gets worse as SNR increases. SBAC algorithm requires noise variance estimate and the accuracy of this estimate degrades as SNR increases.

5.7.2 Scenario 2: 2-D DOA and MC Coefficient Estimation

In the second scenario, it is assumed that the sources have different elevation angles so that 2-D DOA estimation is required to accurately estimate the source locations. In 2-D DOA estimation with sparse recovery, the dictionary matrix should be generated such that it covers both azimuth and elevation planes. Since this task is computationally inefficient, a sequential grid refinement is considered and the following procedure is used.

1. The azimuth and elevation angles of the sources are estimated roughly with a coarse resolution in the dictionary, namely $\Delta_\phi = 3°$ and $\Delta_\theta = 5°$ are selected.

81
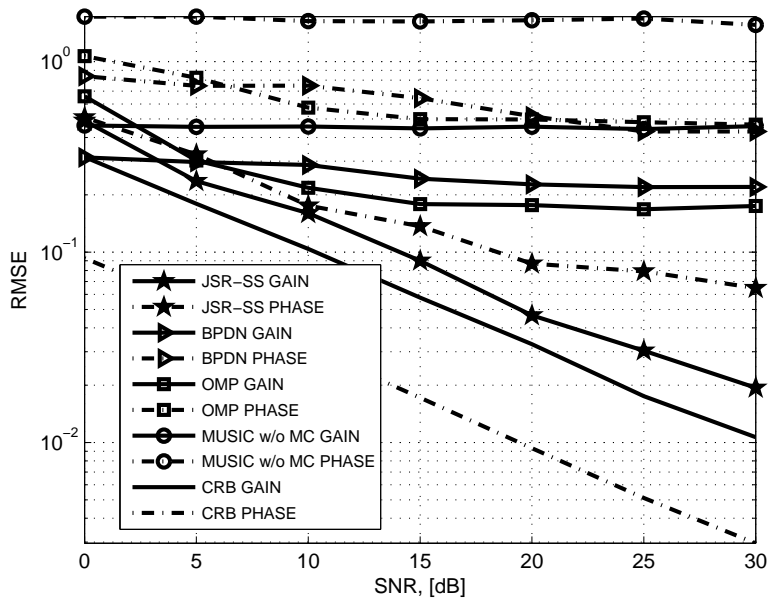
(a)
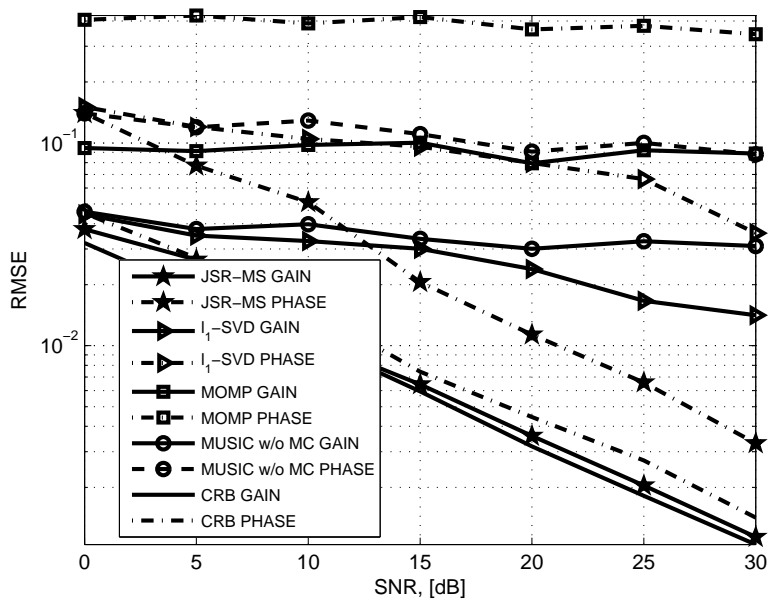
(b)

Figure 5.4: MC gain and phase estimation performance for 1-D scenario with a single (a) and multiple snapshots ($T = 100$) (b). Note that the phase estimates are given in radians. Gain estimation results are denoted with solid lines whereas phase estimates are denoted with dashed lines.
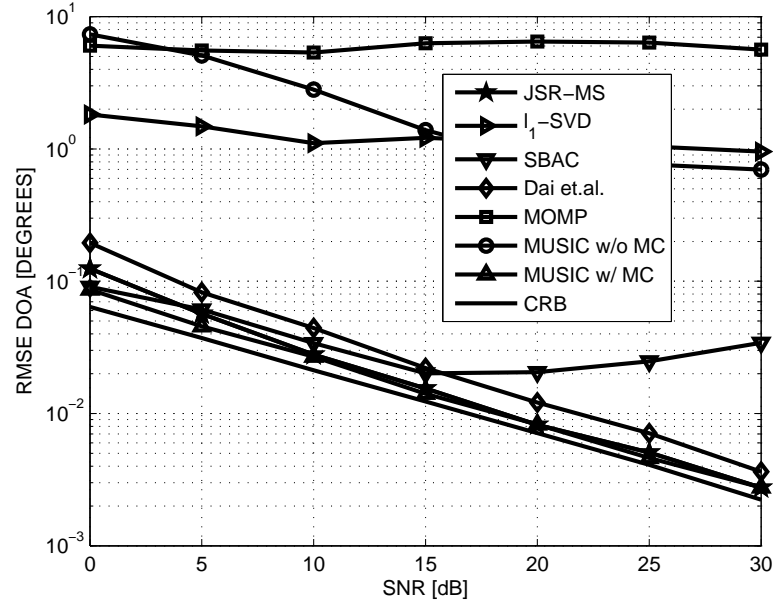
Figure 5.5: 1-D DOA estimation performance vs SNR for ULA when $T = 200$.

2. Then multi-resolution grid refinement is performed in azimuth and elevation dimensions one by one. First, elevation angle is kept fixed and dictionary matrix composed of only the azimuth angles is used. Hence the azimuth angles are found in this step.

3. After the finer azimuth angle estimates are obtained, the azimuth angle is kept fixed and the elevation angles are found.

4. This process is performed until a fine resolution is obtained.

It is observed that the above search procedure has less complexity than the use of a single dictionary matrix with fine resolution in both azimuth and elevation planes.

In Fig. 5.6a and 5.6b, 2-D DOA estimation performance for azimuth and elevation angles is presented for both single and multiple snapshot cases. In Fig. 5.6a, JSR-SS AZ and JSR-SS EL denotes the azimuth and elevation performance of the JSR-SS method respectively. In Fig. 5.6b, JSR-MS AZ and JSR-MS EL stand for the azimuth and elevation performance of JSR-MS method respectively. As it is seen, JSR-SS and JSR-MS perform better than the other algorithms. Note that, in 2-D DOA estimation scenario, the margin between the proposed methods and the CRB gets larger as SNR increases. This is due to the coupling between the azimuth and elevation angles. Fur-

thermore, the proposed methods like the other CS methods produce biased estimates [105].

In Fig. 5.7a and Fig. 5.7b, estimation results for the gain and phase components of coupling coefficients are shown for both single and multiple snapshots respectively. As it is seen, the proposed methods, JSR-SS and JSR-MS provide better results and outperform the other algorithms. When Fig. 5.7a-5.7b are compared with Fig. 5.4a-5.4b where 1-D results are presented, there is a certain performance loss. This is again due to azimuth and elevation coupling and biased estimation.
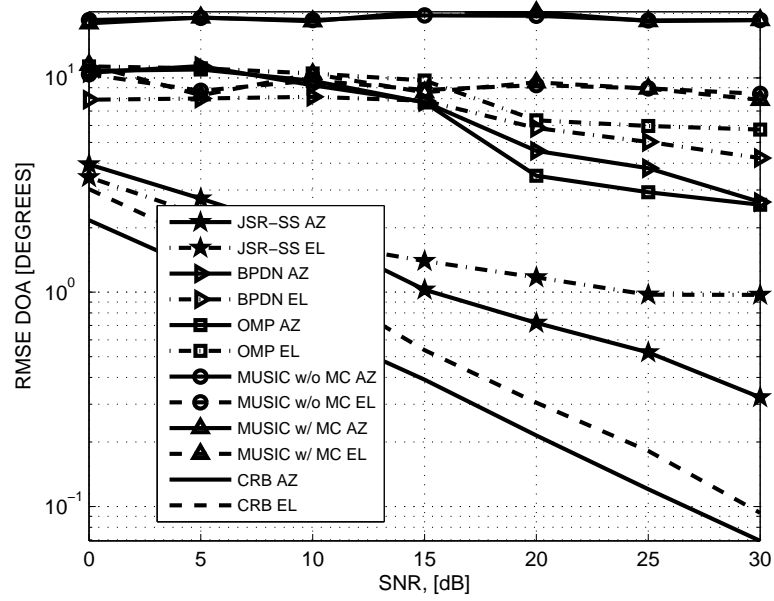
(a)
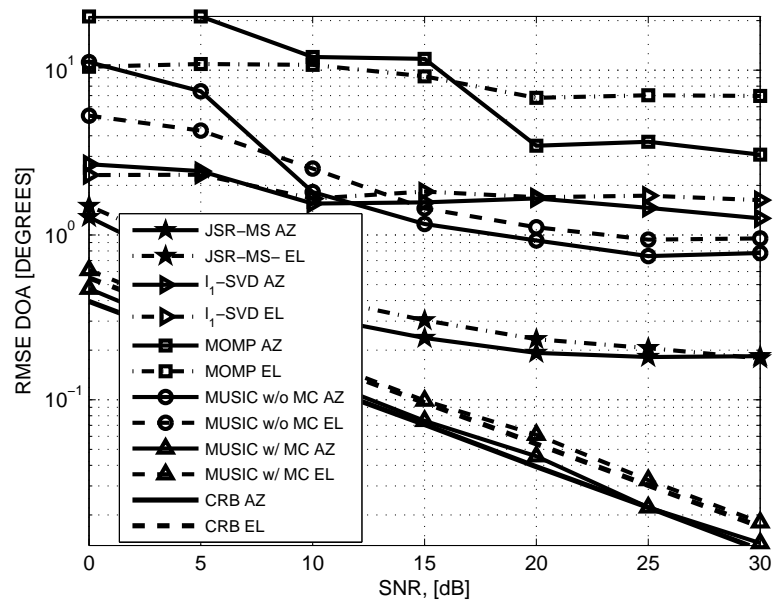
(b)

Figure 5.6: 2-D DOA estimation performance for a single snapshot (a) and multiple snapshots ($T = 30$) (b) respectively. The DOA angles of the sources are $(32.375°, 43.251°)$, $(50.714°, 52.852°)$ and $(75.215°, 62.734°)$. Azimuth estimation results are denoted with solid lines whereas elevation estimates are denoted with dashed lines.
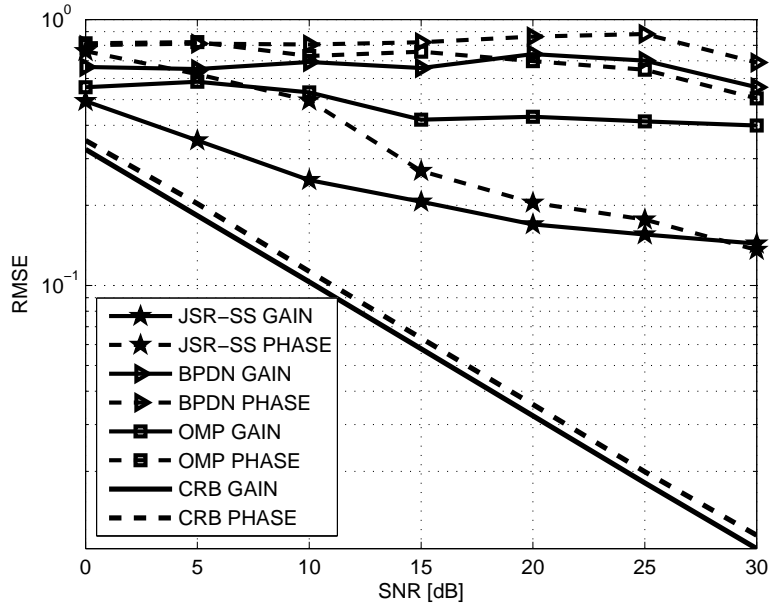
(a)
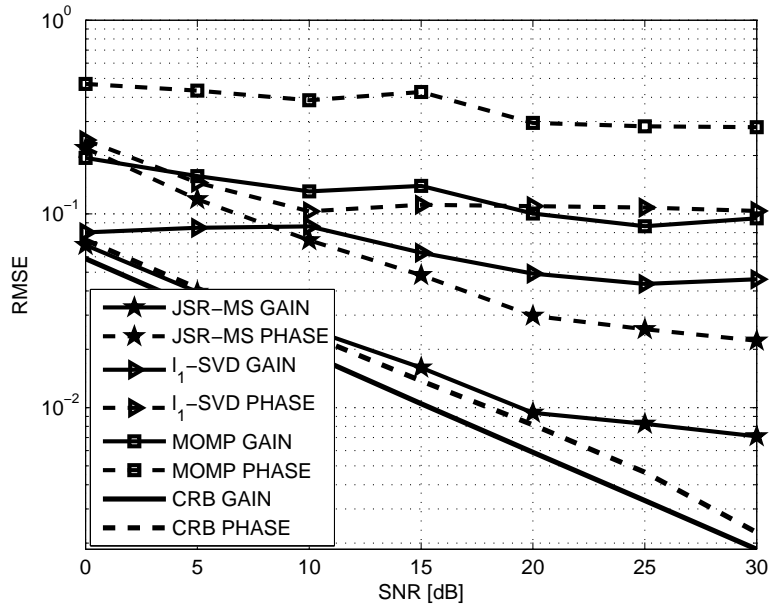
(b)

Figure 5.7: MC gain and phase estimation performance of 2-D scenario for a single snapshot (a) and multiple snapshots ($T = 30$) (b) respectively. Gain estimation results are denoted with solid lines whereas phase estimates are denoted in radians with dashed lines.

5.7.3 Scenario 3: 1-D DOA and Gain/Phase Mismatch Estimation in Multipath Environment

In this part, the performance of the proposed JSR-MS is evaluated in case of gain/phase mismatches and multipath. The signal model and the modifications to JSR-MS method are provided in Appendix B. The selection of the dictionary matrices $\mathbf{A}$ and $\mathbf{D}$ is the same as in the previous scenarios. 100 Monte Carlo trials are run for each experiment. In each trial, the positions of the sensors and the mismatch coefficients are updated. Note that the mismatch parameters are $\gamma_m = \alpha_m e^{j\beta_m}$ for $m = 1, \ldots, M$. The gain and the phase terms of mismatch parameters are selected as $\alpha_m \sim \mathcal{N}(\mu_\alpha, \sigma_\alpha^2)$ and $\beta_m \sim \mathcal{N}(\mu_\beta, \sigma_\beta^2)$ respectively. Here μ_α, μ_β and σ_α^2, σ_β^2 are mean and variances of α_m and β_m respectively.
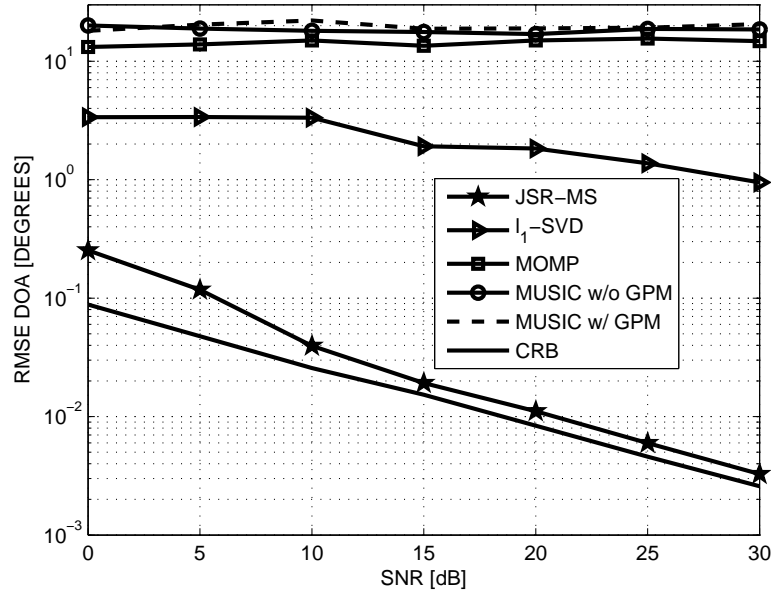
Figure 5.8: DOA estimation performance vs SNR when $T = 100$, $\mu_\alpha = 1$, $\sigma_\alpha = 0.5$ and $\mu_\beta = 0°$, $\sigma_\beta = 20°$.

DOA estimation performance of the proposed method for different SNR levels is presented in Fig. 5.8. As it is seen, JSR-MS closely follows the CRB whereas other algorithms provide large errors. While l_1-SVD and MOMP are effective sparse recovery methods for DOA estimation, they fail in case of array imperfections. The MUSIC algorithm also fails in this scenario since the array covariance matrix is rank-deficient due to coherent source signals. Note that MUSIC w/ GPM and MUSIC w/o

GPM correspond to the MUSIC algorithm with and without known GPM parameters respectively.

In Fig. 5.9, RMSE for the estimation of gain mismatch is shown. As it is seen, JSR-MS performs better than the other algorithms while there is a small gap between JSR-MS and the CRB. In Fig. 5.10, RMSE for the phase term of mismatch coefficients is given. Similar behavior can be observed in this figure in comparison to Fig. 5.9.
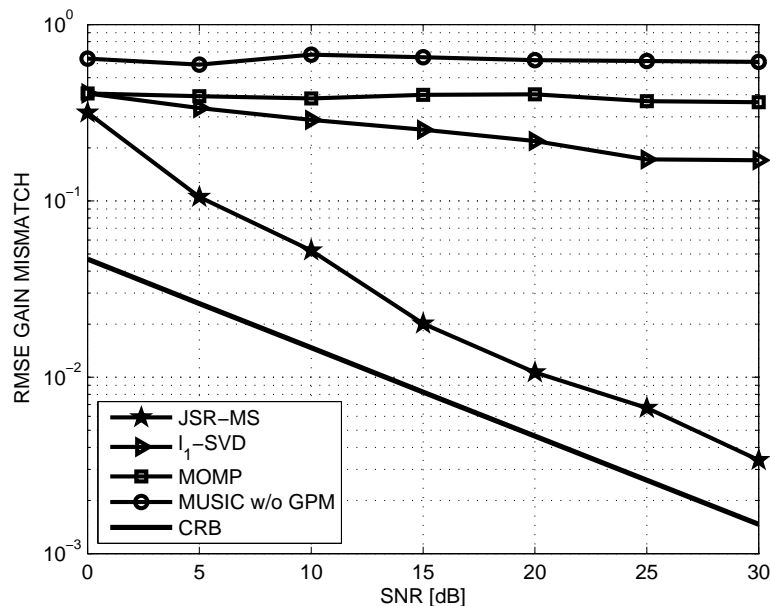
Figure 5.9: RMSE for the gain term of the mismatch coefficients when $T = 100$, $\mu_\alpha = 1$, $\sigma_\alpha = 0.5$ and $\mu_\beta = 0°$, $\sigma_\beta = 20°$.

5.7.4 Performance of JSR-MS For Correlated Source Signals

In this experiment, DOA estimation performance is evaluated when two of the source signals are correlated. The source signals are jointly-Gaussian and selected as $\begin{bmatrix} s_1(t_i) \\ s_2(t_i) \\ s_3(t_i) \end{bmatrix} \sim \mathcal{N} \left(\begin{bmatrix} 0 \\ 0 \\ 0 \end{bmatrix}, \begin{bmatrix} 1 & \rho & 0 \\ \rho & 1 & 0 \\ 0 & 0 & 1 \end{bmatrix} \right)$ for $i = 1, \ldots, T$ where $\rho \in [0, 1]$ is the correlation coefficient. There are $T = 100$ snapshots and SNR = 10dB. The results are shown in Fig. 5.11. The figure shows that the performance of sparsity-based algorithms are not affected much by the correlation between the source signals and
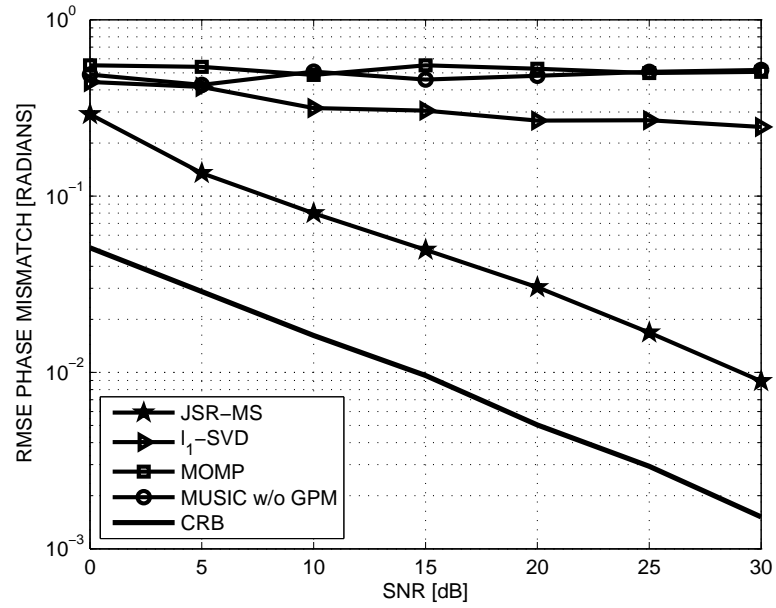
Figure 5.10: RMSE for the phase term of the mismatch coefficients when $T = 100$, $\mu_\alpha = 1$, $\sigma_\alpha = 0.5$ and $\mu_\beta = 0°$, $\sigma_\beta = 20°$.

JSR-MS outperforms the other algorithms. This observation is similar to the results given in [105]. While MUSIC w/o MC provides large errors similar to the results in Fig. 5.3, the performance of MUSIC w/ MC gets worse as $\rho \longrightarrow 1$.
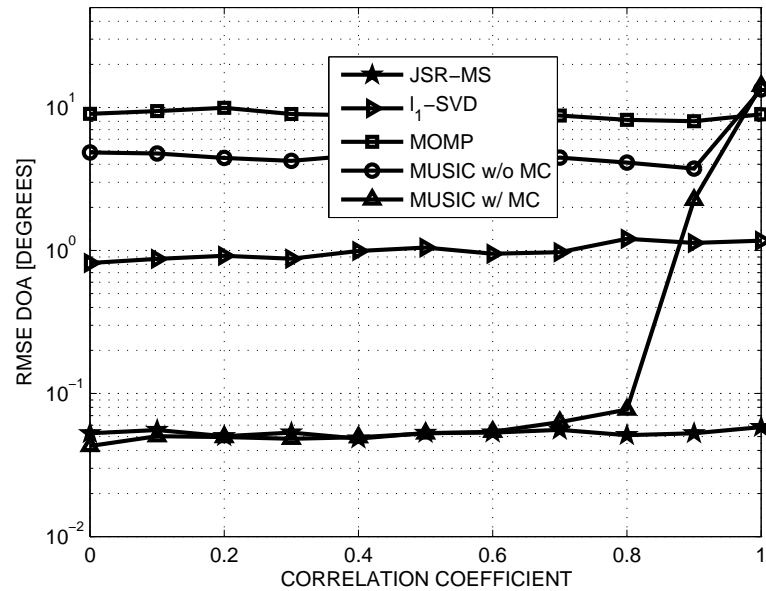
Figure 5.11: 1-D DOA estimation performance for correlated source signals, $T = 100$ and SNR=10dB.

5.7.5 Computational Complexity

In this part, the computational complexities of the proposed methods are compared with the previous methods. The sparse recovery algorithms, l_1-SVD [105] and Basis pursuit [110], have $\mathcal{O}\left((KN_\phi N_\theta)^3\right)$ and $\mathcal{O}\left((N_\phi N_\theta)^3\right)$ complexities respectively for 2-D scenario when there is no mutual coupling. Note that Basis pursuit solves the single snapshot problem while the complexity of l_1-SVD is given for multiple snapshots. The complexity of 2-D MUSIC algorithm is $\mathcal{O}\left(M^3 N_\phi N_\theta\right)$. When MC is taken into consideration, the proposed methods, JSR-SS and JSR-MS have $\mathcal{O}\left((\bar{M} N_\phi N_\theta)^3\right)$ and $\mathcal{O}\left((K\bar{M} N_\phi N_\theta)^3\right)$ complexities respectively. Note that they have the same complexity with Basis pursuit and l_1-SVD when there is no mutual coupling (i.e., $\bar{M} = 1$).

The complexity of the proposed methods is higher than the subspace algorithms such as the MUSIC. However, the MUSIC cannot be used in case of a single snapshot and additional techniques should be employed when there is mutual coupling for multiple snapshots increasing the complexity. In case of arbitrary array geometries, the use of the MUSIC becomes harder for unknown mutual coupling.

5.8   The Advantages of The JSR-SS and JSR-MS

The advantages of the proposed methods are as follows:

- The proposed methods work well in case of mutual coupling for arbitrary structures while most of the algorithms in the literature require fixed and uniform array structures.

- JSR-SS works well when there is only a single snapshot so that it can be used for online array calibration.

- The proposed method can estimate 2-D DOA angles of the unknown source locations with satisfied accuracy.

- The proposed methods are not effected by the correlation between the received source signals. Therefore, they perform well in case of multipath signals.

- The proposed method also woks well in case of gain/phase mismatches and multipath.

CHAPTER 6

CONCLUSIONS

In this thesis, major error sources in DF applications are investigated in detail and three new methods are proposed in order to overcome these distortions and obtain satisfactory DF performance.

In the first problem, an offline calibration technique is proposed for the antenna arrays mounted on aeronautical vehicles. The calibration procedure is performed when the vehicle is on the ground. In this scenario, the reflections from the ground and the platform are the main distortions for DF operation. The scenario is modeled in a numerical electromagnetic simulation tool, FEKO, and the array data is obtained. When the received signals from the antennas are examined, it is observed that they are composed of two parts, namely, the desired signal component and the reflected signal from the ground. In order to mitigate the ground reflections, a time-gating approach is employed using a windowing technique to extract the desired signal component.

In the calibration process, the selection of the setup parameters are very important since their values determine the lengths of the direct path and the ground reflections. These parameters are the heights of the transmitter source and the vehicle as well as the distance between the array and the transmitter. The setup parameters should be selected so that the desired signal and ground reflections can be separated in time by using time-gating. When the desired signal components are gated, sufficiently clean calibration data is obtained. The evaluation of the proposed calibration technique is done by using both correlative interferometer and the MUSIC algorithm.

Since FEKO, the EM simulation tool used to implement the scenario, works in fre-

quency domain, the antenna impulse response is obtained firstly in frequency. Then it is transformed to the time domain for time-gating. In a practical scenario, the proposed method can be applied both in time and frequency domain. In frequency domain application, the calibration data can be collected in the same way as it is obtained in this work. In time domain application, a pulse signal can be transmitted from the transmitter antenna and the array impulse response can be obtained. After time-gating is applied, calibration data is collected in time domain. Then, time-gated signals can be transformed to the frequency domain and the calibration data can be obtained for different frequencies.

The proposed method is simple and time-efficient as compared to other calibration techniques such as the ones performed when the vehicle is airborne. Another advantage of the proposed method is its accuracy. Since the ground reflections and gain/phase mismatches due to the reflections from the platform are effectively eliminated, the DF performance is improved significantly as compared to the uncalibrated scenario. In addition, the proposed calibration technique offers to use the collected calibration data for a wide range of frequencies since the it is performed in time and the calibration data for a certain frequency can easily be obtained by inverse Fourier transform.

In the second problem, far-field DOA estimation and near-field localization of multipath signals is considered. In this scenario, there is a single far-field source with its near-field multipath reflections leading to model mismatches. A new method is proposed for the estimation of DOA angle of the far- and near-field signals and near-field ranges. In order to estimate 2-D DOA angles of the far-field source, a circular array is employed. A calibration technique is used and the collected calibration data is utilized in the MUSIC spectrum for DF operation.

In far-field DOA estimation, calibration data is collected for the elevation interval of $[85°, 95°]$ whereas the effect of multipath differs as the elevation angle of the source changes. Therefore, the calibration data should be collected for a large range of elevation angles in order to obtain satisfactory DF results in a practical scenario.

Once the far-field source parameters are estimated, a near-to-far field transformation is used and it is applied to the array output. This transformation process has two

94

properties. Firstly, it transforms the near-field signal components of the array data to far-field. In this case, the far-field signal components will be suppressed and seen as an interference. Secondly, it transforms the circular array data to virtual array with linear geometry so that spatial smoothing can be applied for accurate DOA estimation of near-field sources. The selection of the inter-element distance of this virtual array is an important issue for accurate parameter estimation. When the distance between the antennas in the virtual array is large, it provides higher DOA estimation accuracy for a narrow angular sector. If the array spacing is small, there is a slight performance loss in DOA accuracy but it is established for a larger angular sector. This trade-off should be solved for a better DF operation. In this study, the selection of the virtual array spacing is examined for $360°$ operation and the best spacing is found by evaluating the possible inter-element spacing in terms of DF accuracy. Once the DOA angles are found, the near-field range parameters are estimated by using a compressed sensing approach. In this case, a dictionary matrix is constructed by stacking the far- and near-field steering vectors with estimated DOA angles.

The performance of the proposed method is evaluated by using numerical electro-magnetic simulation tools and it is shown that parameters of both far- and near-field sources can be accurately estimated. Another advantage of the proposed method is that it has a robust performance in case of multipath.

In the third problem, 2-D DOA and MC coefficient estimation is considered for arbitrary array structures. In this scenario, both single and multiple snapshot cases are investigated and a new method is proposed for parameter estimation. A compressed sensing approach is used where the sparsity of the spatial source directions is utilized together with the MC coefficients. As a result, a joint-sparse recovery algorithm is proposed where both source signals and the MC coefficients are jointly embedded into a joint-sparse vector. This joint-sparse structure is used together with a new dictionary which is constructed by the augmentation of sub-dictionary matrices corresponding to each MC coefficient.

The size of the dictionary matrix is an important issue since it directly affects the computational complexity of the problem. For instance, when an $M \times N$ conventional dictionary matrix which is composed of steering vectors is used, the size of the new

dictionary matrix becomes $M \times \bar{M}N$ for $\bar{M}$ MC coefficients. When a coarse grid is used for the dictionary which reduces the size, the resolution of the solution will be decreased. On the other hand, when a fine dictionary is used, the size of the dictionary and the complexity of the problem will increase significantly. Therefore, selection of the dictionary size is important and designing a dictionary matrix is still an open problem in the literature.

In order to solve the considered problem for multiple snapshots, a new sparsity structure, namely joint-block-sparsity, is introduced to take advantage of the structure in the composite matrix involving both DOA and MC coefficients. In this case, instead of a joint-sparse vector, joint-sparse matrix blocks are utilized. In order to use the joint-block-sparsity in the optimization problem, new norm structures, namely $l_{2,2,0}$- and $l_{2,2,1}$-norms are proposed. In addition to the MC coefficient estimation, joint DOA and gain/phase mismatch estimation is performed in case of multipath.

The proposed method is advantageous since it does not depend on the array structure for joint DOA and MC coefficient estimation. It is shown that the proposed method effectively estimates the DOA angles and mismatch parameters. It can work for both single and multiple snapshot scenarios. The proposed method can ve seen as an on-line calibration technique in the sense that it does not require calibration before DF operation. Moreover, the proposed method can estimate 2-D DOA angles effectively without a pairing problem which exists in parameter estimation problems with arbitrary array structures.

Some of the future works for this research can be summarized as follows:

- In the second problem, only a single far-field source is assumed for DOA estimation. While this is usually the case in HF DF scenarios, the proposed method can be modified for multiple far-field source case.

- In the third problem, the parameter estimation is done by using compressed sensing strategies where a dictionary matrix is used. In the proposed method, an augmented dictionary structure is employed so that the source parameters are estimated with convex optimization. The complexity of these techniques directly depends on the size of the dictionary. Therefore, compact dictionary

structures can be used so that the size of the dictionary and eventually the computational complexity is reduced.

- In the third problem, the antenna patterns of the array elements are assumed to be isotropic which leads to direction-independent MC matrix. In a practical scenario, antennas have directional patters so that the MC matrix becomes direction-dependent. In this case, there are $K\bar{M}$ MC matrix parameters for K sources and $\bar{M}$ unknown parameters in each MC matrix. Hence, there are more unknowns than the number of antennas in the array for arbitrary array structures. However the number of parameters can be reduced for uniform array structures. As a result, a DF scenario in the presence of direction-dependent MC can be considered as a future work.

REFERENCES

[1] H. Krim and M. Viberg. Two decades of array signal processing research: the parametric approach. *Signal Processing Magazine, IEEE*, 13(4):67–94, Jul 1996.

[2] T. Engin Tuncer and Benjamin Friedlander. *Classical and Modern Direction-of-Arrival Estimation*. Academic Press, 2009.

[3] R.O. Schmidt. Multiple emitter location and signal parameter estimation. *Antennas and Propagation, IEEE Transactions on*, 34(3):276–280, Mar 1986.

[4] Bin Liao and Shing-Chow Chan. Adaptive beamforming for uniform linear arrays with unknown mutual coupling. *Antennas and Wireless Propagation Letters, IEEE*, 11:464–467, 2012.

[5] I.J. Gupta and A.A. Ksienski. Effect of mutual coupling on the performance of adaptive arrays. *Antennas and Propagation, IEEE Transactions on*, 31(5):785–791, Sep 1983.

[6] Benjamin Friedlander and A.J. Weiss. Direction finding in the presence of mutual coupling. *Antennas and Propagation, IEEE Transactions on*, 39(3):273–284, Mar 1991.

[7] Boon Poh Ng, Joni Polili Lie, Meng Hwa Er, and Aigang Feng. A practical simple geometry and gain/phase calibration technique for antenna array processing. *Antennas and Propagation, IEEE Transactions on*, 57(7):1963–1972, July 2009.

[8] Lundgren A. Viberg M., Lanne M. Calibration Array Processing. In Tuncer T.E. and Friedlander B., editors, *Classical and Modern Direction-Of-Arrival Estimation*, pages 93–124. Academic Press, 2009.

[9] A. J. Weiss and B. Friedlander. Array shape calibration using sources in unknown locations-a maximum likelihood approach. *IEEE Transactions on Acoustics, Speech, and Signal Processing*, 37(12):1958–1966, Dec 1989.

[10] Y. Rockah and P. Schultheiss. Array shape calibration using sources in unknown locations–part i: Far-field sources. *IEEE Transactions on Acoustics, Speech, and Signal Processing*, 35(3):286–299, Mar 1987.

[11] Stoica P. and Moses R.L. *Spectral Analysis of Signals*. 2005.

[12] N. Yuen and B. Friedlander. Doa estimation in multipath: an approach using fourth-order cumulants. *IEEE Transactions on Signal Processing*, 45(5):1253–1263, May 1997.

[13] Yufeng Zhang, Zhongfu Ye, and Chao Liu. An efficient {DOA} estimation method in multipath environment. *Signal Processing*, 90(2):707 – 713, 2010.

[14] Qiming Bao, C.C. Ko, and Wanjun Zhi. DOA estimation under unknown mutual coupling and multipath. *Aerospace and Electronic Systems, IEEE Transactions on*, 41(2):565–573, April 2005.

[15] Hon Tat Hui. A practical approach to compensate for the mutual coupling effect in an adaptive dipole array. *Antennas and Propagation, IEEE Transactions on*, 52(5):1262–1269, May 2004.

[16] T. Svantesson. Modeling and estimation of mutual coupling in a uniform linear array of dipoles. In *Acoustics, Speech, and Signal Processing, 1999. Proceedings., 1999 IEEE International Conference on*, volume 5, pages 2961–2964 vol.5, 1999.

[17] Zhongfu Ye and Chao Liu. On the Resiliency of MUSIC Direction Finding Against Antenna Sensor Coupling. *Antennas and Propagation, IEEE Transactions on*, 56(2):371–380, Feb 2008.

[18] J. D. Kraus and R. J. Marhefka. *Antennas, Third Edition*. McGraw-Hill, 2002.

[19] J. Dmochowski, J. Benesty, and S. Affes. On spatial aliasing in microphone arrays. *IEEE Transactions on Signal Processing*, 57(4):1383–1395, April 2009.

[20] Zhongfu Ye and Chao Liu. 2-D DOA Estimation in the Presence of Mutual Coupling. *Antennas and Propagation, IEEE Transactions on*, 56(10):3150–3158, Oct 2008.

[21] R. Goossens and H. Rogier. A Hybrid UCA-RARE/Root-MUSIC Approach for 2-D Direction of Arrival Estimation in Uniform Circular Arrays in the Presence of Mutual Coupling. *Antennas and Propagation, IEEE Transactions on*, 55(3):841–849, March 2007.

[22] Jisheng Dai, Xu Bao, Nan Hu, Chunqi Chang, and Weichao Xu. A Recursive RARE Algorithm for DOA Estimation With Unknown Mutual Coupling. *Antennas and Wireless Propagation Letters, IEEE*, 13:1593–1596, 2014.

[23] L. Xiang, Z. Ye, X. Xu, C. Chang, W. Xu, and Y.S. Hung. Direction of arrival estimation for uniform circular array based on fourth-order cumulants in the presence of unknown mutual coupling. *Microwaves, Antennas Propagation, IET*, 2(3):281–287, April 2008.

[24] Kehu Yang, Shu Cai, and Zhi-Quan Luo. Convex relaxation approaches to maximum likelihood DOA estimation in ULA's and UCA's with unknown mutual coupling. In *Acoustics, Speech and Signal Processing (ICASSP), 2011 IEEE International Conference on*, pages 2556–2559, May 2011.

[25] V. Agrawal and Yuen Lo. Mutual coupling in phased arrays of randomly spaced antennas. *Antennas and Propagation, IEEE Transactions on*, 20(3):288–295, May 1972.

[26] Weiping Mao, Guolin Li, Xin Xie, and Qingzhi Yu. DOA Estimation of Coherent Signals Based on Direct Data Domain Under Unknown Mutual Coupling. *Antennas and Wireless Propagation Letters, IEEE*, 13:1525–1528, 2014.

[27] Tansu Filik and T.Engin Tuncer. 2-D DOA estimation in case of unknown mutual coupling for multipath signals. *Multidimensional Systems and Signal Processing*, pages 1–18, 2014.

[28] Ahmet M. Elbir and T. Engin Tuncer. Calibration of antenna arrays for aeronautical vehicles on ground. *Aerospace Science and Technology*, 30(1):18 – 25, 2013.

[29] Chong Meng Samson See and A.B. Gershman. Direction-of-arrival estimation in partly calibrated subarray-based sensor arrays. *Signal Processing, IEEE Transactions on*, 52(2):329–338, Feb 2004.

[30] P. Heidenreich, A.M. Zoubir, and M. Rubsamen. Joint 2-D DOA Estimation and Phase Calibration for Uniform Rectangular Arrays. *Signal Processing, IEEE Transactions on*, 60(9):4683–4693, Sept 2012.

[31] A. Leshem and M. Wax. Array calibration in the presence of multipath. *Signal Processing, IEEE Transactions on*, 48(1):53–59, Jan 2000.

[32] M. Aktas and T. E. Tuncer. HOS based online calibration. In *Signal Processing Conference, 2011 19th European*, pages 604–608, Aug 2011.

[33] Ahmet M. Elbir and T. Engin Tuncer. Far-field DOA estimation and near-field localization for multipath signals. *Radio Science*, 49(9):765–776, 2014.

[34] X. Zeng W. Wang J. Zhang J. Liang, D. Liu and H. Chen. Joint azimuth-elevation/(-range) estimation of mixed near-field and far-field sources using two-stage separated steering vector-based algorithm. *Progress In Electromagnetics Research*, 113:17–46, 2011.

[35] J. Liang and D. Liu. Passive localization of mixed near-field and far-field sources using two-stage music algorithm. *IEEE Transactions on Signal Processing*, 58(1):108–120, Jan 2010.

[36] B. Wang, Y. Zhao, and J. Liu. Mixed-order music algorithm for localization of far-field and near-field sources. *IEEE Signal Processing Letters*, 20(4):311–314, April 2013.

[37] J. He, M. N. S. Swamy, and M. O. Ahmad. Efficient application of music algorithm under the coexistence of far-field and near-field sources. *IEEE Transactions on Signal Processing*, 60(4):2066–2070, April 2012.

[38] J. j. Jiang, F. j. Duan, J. Chen, Y. c. Li, and X. n. Hua. Mixed near-field and far-field sources localization using the uniform linear sensor array. *IEEE Sensors Journal*, 13(8):3136–3143, Aug 2013.

[39] G. Liu and X. Sun. Efficient method of passive localization for mixed far-field and near-field sources. *IEEE Antennas and Wireless Propagation Letters*, 12:902–905, 2013.

[40] F. Wen and W. P. Tay. Localization for mixed near-field and far-field sources using data supported optimization. In *Information Fusion (FUSION), 2012 15th International Conference on*, pages 402–407, July 2012.

[41] R. Roy and T. Kailath. ESPRIT-estimation of signal parameters via rotational invariance techniques. *Acoustics, Speech and Signal Processing, IEEE Transactions on*, 37(7):984–995, Jul 1989.

[42] J. S. Thompson, P. M. Grant, and B. Mulgrew. Performance of spatial smoothing algorithms for correlated sources. *IEEE Transactions on Signal Processing*, 44(4):1040–1046, Apr 1996.

[43] Yih-Min Chen. On spatial smoothing for two-dimensional direction-of-arrival estimation of coherent signals. *IEEE Transactions on Signal Processing*, 45(7):1689–1696, Jul 1997.

[44] Shiwei Ren, Xiaochuan Ma, Shefeng Yan, and Chengpeng Hao. 2-d unitary esprit-like direction-of-arrival (doa) estimation for coherent signals with a uniform rectangular array. *Sensors*, 13(4):4272, 2013.

[45] Pál Turán. *Leopold Fejér Gesammelte Arbeiten I*, chapter Über den Zusammenhang der Extremen von Harmonischen Funktionen mit Ihren Koeffizienten und Über den Picard—Landauschen Satz, pages 693–715. Birkhäuser, Basel, 1970.

[46] Benjamin Friedlander and A.J. Weiss. Direction finding using spatial smoothing with interpolated arrays. *Aerospace and Electronic Systems, IEEE Transactions on*, 28(2):574–587, Apr 1992.

[47] T. E. Tuncer, T. K. Yasar, and B. Friedlander. Direction of arrival estimation for nonuniform linear arrays by using array interpolation. *Radio Science*, 42(4), 2007. RS4002.

[48] F. Belloni, A. Richter, and V. Koivunen. DoA Estimation Via Manifold Separation for Arbitrary Array Structures. *Signal Processing, IEEE Transactions on*, 55(10):4800–4810, Oct 2007.

[49] M. Rubsamen and A.B. Gershman. Direction-of-Arrival Estimation for Nonuniform Sensor Arrays: From Manifold Separation to Fourier Domain MUSIC Methods. *Signal Processing, IEEE Transactions on*, 57(2):588–599, Feb 2009.

[50] M. Aktas and T. E. Tuncer. Iterative HOS-SOS (IHOSS) Algorithm for Direction-of-Arrival Estimation and Sensor Localization. *Signal Processing, IEEE Transactions on*, 58(12):6181–6194, Dec 2010.

[51] E.J. Candès and M.B. Wakin. An Introduction To Compressive Sampling. *Signal Processing Magazine, IEEE*, 25(2):21–30, March 2008.

[52] Emmanuel J. Candès, Justin K. Romberg, and Terence Tao. Stable signal recovery from incomplete and inaccurate measurements. *Communications on Pure and Applied Mathematics*, 59(8):1207–1223, 2006.

[53] Candès E. J. Compressive sampling. In *, In Proceedings of the International Congress of Mathematicians*, pages 1433–1452, Aug 2006.

[54] D. L. Donoho. Compressed sensing. *IEEE Transactions on Information Theory*, 52(4):1289–1306, April 2006.

[55] Ahmet M. Elbir and T. Engin Tuncer. 2-D DOA and Mutual Coupling Coefficient Estimation for Arbitrary Array Structures with Single and Multiple Snapshots. *Digit. Signal Process.*, 54(C):75–86, July 2016.

[56] Paul N.D. Saucier N.E. Deep depression angle calibration of airborne direction finding arrays, US Patent No: 6,806,837, 19 Oct 2004.

[57] L. Dinoi, A. Di Vito, and G. Lubello. Direction finding of ground based emitters from airborne platforms. In *Radar Conference, 2008. RADAR '08. IEEE*, pages 1–6, May 2008.

[58] Anthony Bellion, C. Le Meins, Anne Julien-Vergonjanne, and Thierry Monédière. Calibration of direction finding antennas in complex environment. In *Colloque URSI 2008 (International Unio of Radio Science)*, Chicago, United States.

[59] Zhao Tan, Peng Yang, and A. Nehorai. Joint Sparse Recovery Method for Compressed Sensing With Structured Dictionary Mismatches. *Signal Processing, IEEE Transactions on*, 62(19):4997–5008, Oct 2014.

[60] M.M. Hyder and K. Mahata. Direction-of-Arrival Estimation Using a Mixed $l_{2,0}$-norm Norm Approximation. *Signal Processing, IEEE Transactions on*, 58(9):4646–4655, Sept 2010.

[61] Tansu Filik and T. Engin Tuncer. A fast and automatically paired 2-D direction-of-arrival estimation with and without estimating the mutual coupling coefficients. *Radio Science*, 45(3), 2010. RS3009.

[62] Balanis C.A. *Antenna Theory: Analysis and Design*. Wiley-Interscience. N.J. Prentice Hall, NY, USA., 2005.

[63] S. Das and D. Mandal. Synthesis of broadside uniform circular antenna array with low on-surface scanning. In *Antenna Week (IAW), 2011 Indian*, pages 1–4, Dec 2011.

[64] Ding Wang, Hui Yao, and Ying Wu. Sensor array calibration for uniform rectangular array in presence of mutual coupling and sensor gain-and-phase errors. *Journal of Central South University*, 21(6):2228–2239, 2014.

[65] Sana Salous. *Radio Channel Models*, pages 85–147. John Wiley & Sons, Ltd, 2013.

[66] Y. S. Hsu, K. T. Wong, and L. Yeh. Mismatch of near-field bearing-range spatial geometry in source-localization by a uniform linear array. *IEEE Transactions on Antennas and Propagation*, 59(10):3658–3667, Oct 2011.

[67] M. N. El Korso, A. Renaux, R. Boyer, and S. Marcos. Deterministic performance bounds on the mean square error for near field source localization. *IEEE Transactions on Signal Processing*, 61(4):871–877, Feb 2013.

[68] I Bertino M Bozzetti, G M Ariano and P Galati. A state of the art anechoic cham-ber for air vehicle testing at Alenia Aeronautica. In *International Unionof Radio Science*, pages 175–178, November 2008 2008.

[69] M. S. Reese, C. A. Balanis, C. R. Blncher, and G. C. Barber. Modeling and simulation of a helicopter-mounted satcom antenna array. *IEEE Antennas and Propagation Magazine*, 53(2):51–60, April 2011.

[70] Aubin J.F. and Hartman R.E. Design, calibration and performance of a full-sized aircraft antenna range from 30MHz to 40 GHz. *Technical Paper, Microwave Vision*, Nov. 1981.

[71] T. Umeda, Y. Matsumoto, A. Nishikata, Y. Yamanaka, A. Sugiura, and K. Koike. Emi antenna calibration on an absorber-lined ground plane for measuring free-space antenna factor. In *Electromagnetic Compatibility, 2002. EMC 2002. IEEE International Symposium on*, volume 1, pages 43–48, Aug 2002.

[72] Marcos V.T. Heckler and Achim Dreher. Performance of microstrip antenna arrays installed on aircraft. *Aerospace Science and Technology*, 26(1):235–143, 2013.

[73] R. Bunger, F. Demmel, and J. Ritter. Installed performance analysis of a direction finding system on board of a large aircraft platform. In *Microwave Conference, 2003. 33rd European*, volume 2, pages 695–697 vol.2, Oct 2003.

[74] Warren F. Perger Irfan Ahmed and Seyed A. Zekavat. Effects of Ground Constituent Parameters on Array Mutual Coupling for DOA Estimation. *International Journal of Antennas and Propagation*, 2011(Article ID 425913), 2011.

[75] S. Kashyap and S. R. Mishra. Improvement in antenna factor measurements using time-domain gating. In *Electromagnetic Compatibility, 1988. Symposium Record., IEEE 1988 International Symposium on*, pages 82–86, Aug 1988.

[76] FEKO User's Manual. EM Software and System. 2010.

[77] P. Stoica and A. Nehorai. Music, maximum likelihood, and cramer-rao bound: further results and comparisons. *IEEE Transactions on Acoustics, Speech, and Signal Processing*, 38(12):2140–2150, Dec 1990.

[78] Taylan Aksoy and T. Engin Tuncer. Measurement reduction for mutual coupling calibration in doa estimation. *Radio Science*, 47(3):n/a–n/a, 2012. RS3004.

[79] H. Nyquist. Certain topics in telegraph transmission theory. *Transactions of the American Institute of Electrical Engineers*, 47(2):617–644, April 1928.

[80] Alan V. Oppenheim, Ronald W. Schafer, and John R. Buck. *Discrete-time signal processing*. Prentice Hall signal processing series. Upper Saddle River, N.J. Prentice Hall, 1999.

[81] V. Sipal, B. Allen, and D. Edwards. Effects of antenna impulse response on wideband wireless channel. In *Antennas and Propagation Conference (LAPC), 2010 Loughborough*, pages 129–132, Nov 2010.

[82] D. Camell, R. T. Johnk, D. Novotny, and C. Grosvenor. Free-space antenna factors through the use of time-domain signal processing. In *Electromagnetic Compatibility, 2007. EMC 2007. IEEE International Symposium on*, pages 1–5, July 2007.

[83] R. Rammal, M. Lalande, E. Martinod, N. Feix, M. Jouvet, J. Andrieu, and B. Jecko. Far-Field Reconstruction from Transient Near-Field Measurement Using Cylindrical Modal Development. *International Journal of Antennas and Propagation*, 2009:1–8, 2009.

[84] C. s. Park and D. y. Kim. The fast correlative interferometer direction finder using i/q demodulator. In *Communications, 2006. APCC '06. Asia-Pacific Conference on*, pages 1–5, Aug 2006.

[85] Akimichi Hirota, Takehiro Miyamoto, Masayuki Nakano, and Hiroyuki Arai. Modified calibration method for music method with an array antenna. *Electronics and Communications in Japan (Part I: Communications)*, 90(10):1–13, 2007.

[86] Lena Chang. Signal subspace transformation for direction-of-arrival estimation of wideband sources in near field. *Journal of Marine Science and Technology*, 18(6):830–836, 2010.

[87] De sen Yang, Jie Shi, and Bo sheng Liu. Doa estimation for the near-field correlated sources with interpolated array technique. In *Industrial Electronics and Applications, 2009. ICIEA 2009. 4th IEEE Conference on*, pages 3011–3015, May 2009.

[88] J.S. Thompson, Peter M. Grant, and B. Mulgrew. Performance of spatial smoothing algorithms for correlated sources. *Signal Processing, IEEE Transactions on*, 44(4):1040–1046, Apr 1996.

[89] User's Manual version 2.7 Wireless InSite. Remcom, PA, USA. 2012.

[90] Emmanuel J. Candès. The restricted isometry property and its implications for compressed sensing. *Comptes Rendus Mathematique*, 346(9–10):589 – 592, 2008.

[91] E. J. Candès and T. Tao. Near-optimal signal recovery from random projections: Universal encoding strategies? *IEEE Trans. Inf. Theor.*, 52(12):5406–5425, December 2006.

[92] E. J. Candes, J. Romberg, and T. Tao. Robust uncertainty principles: exact signal reconstruction from highly incomplete frequency information. *IEEE Transactions on Information Theory*, 52(2):489–509, Feb 2006.

[93] M. F. Duarte and Y. C. Eldar. Structured compressed sensing: From theory to applications. *IEEE Transactions on Signal Processing*, 59(9):4053–4085, Sept 2011.

[94] I. Bilik. Spatial compressive sensing for direction-of-arrival estimation of multiple sources using dynamic sensor arrays. *IEEE Transactions on Aerospace and Electronic Systems*, 47(3):1754–1769, July 2011.

[95] ITU-R. *Direction finding and location determination at monitoring stations*. Rec. SM.854-3. Geneva, 2010.

[96] F. Röemer M. Haardt, M. Pesavento and M. N. El Korso. Subspace Methods and Exploitation of Special Array Structures. In *Signal Processing: Array and Statistical Signal Processing*, volume 3, pages 651–717. Elsevier, 2014.

[97] I. Ziskind and M. Wax. Maximum likelihood localization of multiple sources by alternating projection. *Acoustics, Speech and Signal Processing, IEEE Transactions on*, 36(10):1553–1560, Oct 1988.

[98] S. Fortunati, R. Grasso, F. Gini, and M.S. Greco. Single snapshot DOA estimation using compressed sensing. In *Acoustics, Speech and Signal Processing (ICASSP), 2014 IEEE International Conference on*, pages 2297–2301, May 2014.

[99] K. Kim, Tapan Kumar Sarkar, and M.S. Palma. Adaptive processing using a single snapshot for a nonuniformly spaced array in the presence of mutual coupling and near-field scatterers. *Antennas and Propagation, IEEE Transactions on*, 50(5):582–590, May 2002.

[100] Tongyu Zhang Yuguan Hou and Shaochuan Wu. CC-MUSIC: An Optimization Estimator for Mutual Coupling Correction of L-Shaped Nonuniform Array with Single Snapshot. *Mathematical Problems in Engineering*, 2015(Article ID 969042):11, 2015.

[101] Mehdi Banitalebi Dehkordi, Hamid Reza Abutalebi, and Mohammad Reza Taban. Sound source localization using compressive sensing-based feature extraction and spatial sparsity. *Digital Signal Processing*, 23(4):1239 – 1246, 2013.

[102] Richard Porter, Vladislav Tadic, and Alin Achim. Sparse bayesian learning for non-gaussian sources. *Digital Signal Processing*, 45:2 – 12, 2015.

[103] Zhen-Qing He, Zhi-Ping Shi, and Lei Huang. Covariance sparsity-aware DOA estimation for nonuniform noise . *Digital Signal Processing*, 28:75 – 81, 2014.

[104] M. Carlin, P. Rocca, G. Oliveri, F. Viani, and A. Massa. Directions-of-Arrival Estimation Through Bayesian Compressive Sensing Strategies. *Antennas and Propagation, IEEE Transactions on*, 61(7):3828–3838, July 2013.

[105] D. Malioutov, M. Cetin, and A.S. Willsky. A sparse signal reconstruction perspective for source localization with sensor arrays. *Signal Processing, IEEE Transactions on*, 53(8):3010–3022, Aug 2005.

[106] A. M. Elbir and T. E. Tuncer. Sparse Support Recovery For DOA Estimation in the Presence of Mutual Coupling. In *Signal Processing Conference, 2015 23rd European*, Aug 2015.

[107] J. Dai, D. Zhao, and X. Ji. A Sparse Representation Method for DOA Estimation With Unknown Mutual Coupling. *Antennas and Wireless Propagation Letters, IEEE*, 11:1210–1213, 2012.

[108] Zhang-Meng Liu and Yi-Yu Zhou. A Unified Framework and Sparse Bayesian Perspective for Direction-of-Arrival Estimation in the Presence of Array Imperfections. *Signal Processing, IEEE Transactions on*, 61(15):3786–3798, Aug 2013.

[109] T.T. Zhang, Y.L. Lu, and H.T. Hui. Simultaneous estimation of mutual coupling matrix and DOAs for UCA and ULA. In *Electromagnetic Compatibility, 2006. EMC-Zurich 2006. 17th International Zurich Symposium on*, pages 265–268, Feb 2006.

[110] Scott Shaobing Chen, David L. Donoho, and Michael A. Saunders. Atomic decomposition by basis pursuit. *SIAM Journal on Scientific Computing*, 20:33–61, 1998.

[111] Stephen Boyd and Lieven Vandenberghe. *Convex Optimization*. Cambridge University Press, Cambridge, U.K, 2004.

[112] I. F. Gorodnitsky and B. D. Rao. Sparse signal reconstruction from limited data using focuss: a re-weighted minimum norm algorithm. *IEEE Transactions on Signal Processing*, 45(3):600–616, Mar 1997.

[113] Yonina C. Eldar. *Sampling Theory: Beyond Bandlimited Systems*. Cambridge University Press, New York, NY, USA, 2014.

[114] Jeffrey D. Blanchard, Coralia Cartis, and Jared Tanner. Compressed Sensing: How sharp is the Restricted Isometry Property? *SIAM Rev.*, 53(1):105–125, February 2011.

[115] Albert Cohen, Wolfgang Dahmen, and Ronald Devore. Compressed sensing and best k-term approximation. *J. Amer. Math. Soc*, pages 211–231, 2009.

[116] Kiryung Lee and Yoram Bresler. Performance of Jointly Sparse Support Recovery in Compressed Sensing. In *Information Theory and Applications Workshop*, Feb 2011.

[117] S.F. Cotter, B.D. Rao, K. Engan, and K. Kreutz-Delgado. Sparse solutions to linear inverse problems with multiple measurement vectors. *Signal Processing, IEEE Transactions on*, 53(7):2477–2488, July 2005.

[118] S.G. Mallat and Z. Zhang. Matching pursuits with time-frequency dictionaries. *Signal Processing, IEEE Transactions on*, 41(12):3397–3415, Dec 1993.

APPENDIX A

RMSE DEFINITION FOR AZIMUTH ANGLE

One far-field and $N - 1$ near-field sources are considered for J_T trials and a range of $l \in [\lambda/300, \lambda/30]$. In each trial, the near-field sources are fixed and the DOA of the far-field source is changed. The observed array output for the jth trial is constructed as

$$\mathbf{y}_j(t) = \mathbf{a}(\Theta_1^j)s(t) + \sum_{i=2}^{N} \tilde{\mathbf{a}}(\Theta_i, d_i)s(t), \quad t = 1, \ldots, E. \tag{A.1}$$

After the far-field source DOA Θ_1^j is found as described in Sec. 4.3, the NFT matrix is constructed for q^{th} index of l (l_q) as

$$\mathbf{T}_q = \mathbf{V}_q\mathbf{U}^\dagger \tag{A.2}$$

where $\mathbf{V}_q$ is the far-field data set computed for the element spacing l_q and $\mathbf{U}$ is the near-field data set. The array output is transformed to virtual ULA as

$$\tilde{\mathbf{y}}_{qj}(t) = \mathbf{T}_q\,\mathbf{y}_j(t) \tag{A.3}$$

Then the near-field source azimuth angles for l_q and j^{th} trial $\{\hat{\phi}_{qij}\}_{i=2}^{N}$ are estimated as described in Sec. 4.4.2. Finally the RMSE for l_q is computed as

$$RMSE(l_q) = \sqrt{\frac{1}{J_T(N-1)} \sum_{j=1}^{J_T} \sum_{i=2}^{N} |\hat{\phi}_{qij} - \phi_{ij}|^2} \tag{A.4}$$

where ϕ_{qij} and $\hat{\phi}_{qij}$ are the true and estimated azimuth angles respectively.

APPENDIX B

DOA ESTIMATION IN THE PRESENCE OF GAIN/PHASE MISMATCHES AND MULTIPATH

In this appendix, the signal model and the modifications to the JSR-MS method are presented in the presence of gain/phase mismatches and multipath. In this case, the signal model is given as follows

$$\mathbf{y}(t_i) = \mathbf{\Gamma} \sum_{k=1}^{K} \mathbf{a}(\bar{\Theta}_k) s_k(t_i) + \mathbf{e}(t_i), \quad i = 1, \ldots, T \tag{B.1}$$

where T is the number of snapshots, $\mathbf{e}(t_i)$ is the spatially and temporarily white, zero-mean Gaussian noise. $s_k(t_i)$ is the kth coherent source signal. The source signals are related to each other as $s_{k_1}(t_i) = \eta_{k_1 k_2} s_{k_2}(t_i)$ for $i = 1, \ldots, T$ and $k_1, k_2 = 1, \ldots, K$ where $k_1 \neq k_2$ and $\eta_{k_1 k_2}$ is a complex scalar. $\bar{\Theta}_k$ represents the direction-of-arrival (DOA) angle of the kth source. $\mathbf{a}(\bar{\Theta}_k)$ is an $M \times 1$ nominal array steering vector for the kth source. The mismatch matrix is denoted by $\mathbf{\Gamma} = diag(\gamma_1, \gamma_2, \ldots, \gamma_M)$ which is direction independent and it represents the array gain and phase uncertainties [6]. The entries of $\mathbf{\Gamma}$ are in the form of $\gamma_m = \alpha_m e^{j\beta_m}$ where $\alpha_m, \beta_m \in \mathbb{R}$ are the gain and phase mismatch terms for $m = 1, \ldots, M$ respectively.

In order to estimate source DOA angles with JSR-MS method, the array output is written in compressed sensing (CS) context as

$$\mathbf{Y} = \mathbf{\Gamma AS} + \mathbf{E} \tag{B.2}$$

where $\mathbf{Y} = [\mathbf{y}(t_1), \mathbf{y}(t_2), \ldots, \mathbf{y}(t_T)]$ is the $M \times T$ observation matrix and $\mathbf{E} = [\mathbf{e}(t_1), \mathbf{e}(t_2), \ldots, \mathbf{e}(t_T)]$. $\mathbf{S} = [\mathbf{s}(t_1), \mathbf{s}(t_2), \ldots, \mathbf{s}(t_T)]$ is an $N \times T$ matrix whose each column is a K-sparse vector, namely, all the entries of $\mathbf{s}(t_i)$ but K are zero for $i = 1, \ldots, T$. The number of non-zero entries of $\mathbf{S}$ is denoted by l_0-norm as

$||\mathbf{S}||_0 = |\{n, i : s_n(t_i) \neq 0\}|$ where n and i correspond to the source direction and snapshot indices respectively. Note that $\mathbf{S}$ has K non-zero rows and the other rows are zero. In order to find the source DOA angles and mismatch parameters, the CS problem can be written as

$$\min_{\mathbf{S} \in \mathbb{R}^{N \times T}, \mathbf{\Gamma} \in \mathbb{C}^{M \times M}} ||\mathbf{S}||_0 \ s.t. \ ||\mathbf{Y} - \mathbf{\Gamma AS}||_F^2 \leq \epsilon^2 \tag{B.3}$$

Above problem is non-linear due to the unknowns $\mathbf{S}$ and $\mathbf{\Gamma}$. Moreover, the computational complexity of P_1 increases with T. In the following part, firstly, the dependence of complexity on T is removed using the SVD of the measurement matrix $\mathbf{Y}$ [105]. Then the joint-sparsity is utilized to formulate the problem in convex and linear form so that (B.3) can be solved effectively. Therefore we first consider the SVD of $\mathbf{Y}$ as $\mathbf{Y} = \mathbf{U\Sigma V}^H$ where $\mathbf{U}$ and $\mathbf{V}$ are left and right singular vector matrices of $\mathbf{Y}$ respectively. $\mathbf{\Sigma}$ is an $M \times T$ diagonal matrix composed of the singular values of $\mathbf{Y}$. While there are K source signals, there is a single dominant singular value in $\mathbf{\Sigma}$ due to coherent source signals. Therefore, the $M \times T$ measurement matrix $\mathbf{Y}$ is reduced to an $M \times 1$ vector $\tilde{\mathbf{y}}$ as

$$\tilde{\mathbf{y}} = \mathbf{\Gamma A\tilde{s}} + \tilde{\mathbf{e}} \tag{B.4}$$

where $\tilde{\mathbf{y}} = \mathbf{U\Sigma z} = \mathbf{YVz}$, $\tilde{\mathbf{s}} = \mathbf{SVz}$ and $\tilde{\mathbf{E}} = \mathbf{EVz}$. $\mathbf{z} = [1, 0, \ldots, 0]^T$ is $T \times 1$ vector whose all entries are zero but the first entry is one. Note that the row indices of the non-zero terms in $\mathbf{S}$ and $\tilde{\mathbf{s}}$ are the same. Now the reduced model in (B.4) can be rewritten in the following form, i.e.,

$$\tilde{\mathbf{y}} = \sum_{m=1}^{M} \gamma_m \mathbf{J}_m \mathbf{A\tilde{s}} + \tilde{\mathbf{e}} \tag{B.5}$$

where $\mathbf{J}_m$ is an $M \times M$ matrix whose all entries are zero but only the mth diagonal entry is one.

In order to obtain a linear optimization problem, the model in (B.5) is further modified so that the unknown terms are inserted into a vector as

$$\tilde{\mathbf{y}} = \mathbf{D\tilde{x}} + \tilde{\mathbf{e}} \tag{B.6}$$

where the $M \times MN$ dictionary matrix $\mathbf{D}$ is defined by stacking $\mathbf{A}$ as $\mathbf{D} =$

$[\mathbf{J}_1\mathbf{A}, \mathbf{J}_2\mathbf{A}, \ldots, \mathbf{J}_M\mathbf{A}]$. The $MN \times 1$ vector $\tilde{\mathbf{x}}$ is defined as

$$\begin{aligned}
\tilde{\mathbf{x}} = \boldsymbol{\gamma} \otimes \tilde{\mathbf{s}} &= \left[\gamma_1\tilde{\mathbf{s}}^T, \gamma_2\tilde{\mathbf{s}}^T, \ldots, \gamma_M\tilde{\mathbf{s}}^T\right]^T \\
&= \left[\tilde{\mathbf{x}}^{(1)T}, \tilde{\mathbf{x}}^{(2)T}, \ldots, \tilde{\mathbf{x}}^{(M)T}\right]^T
\end{aligned} \tag{B.7}$$

where $\otimes$ denotes the Kronecker product and $\boldsymbol{\gamma} = [\gamma_1, \ldots, \gamma_M]^T$. $\tilde{\mathbf{x}}^{(m)}$ is the mth subblock of $\tilde{\mathbf{x}}$. Since $\tilde{\mathbf{s}}$ is K-sparse, $\tilde{\mathbf{x}}$ becomes an MK-sparse vector where $\tilde{\mathbf{s}}$ and mismatch parameters $\boldsymbol{\gamma}$ are embedded together. After some manipulations as in Sec. 5, the final form of the optimization problem is given as

$$\min_{\tilde{\mathbf{x}} \in \mathbb{C}^{MN \times 1}} \zeta||\tilde{\mathbf{x}}||_{2,1} + \frac{1}{2}||\tilde{\mathbf{y}} - \mathbf{D}\tilde{\mathbf{x}}||_2^2 \tag{B.8}$$

where ζ is the penalty term that balances the trade-off between $l_{2,1}/l_2$ normed terms. The mixed $l_{2,1}$-norm $||\tilde{\mathbf{x}}||_{2,1}$ is explicitly given as

$$||\tilde{\mathbf{x}}||_{2,1} = \sum_{n=1}^{N} \left(\sum_{m=1}^{M} (|\gamma_m\tilde{s}_n|)^2\right)^{1/2} \tag{B.9}$$

Once (B.8) is solved, the source DOA angles and the mismatch parameters can be found in the same way as in Sec. 5.

CURRICULUM VITAE

PERSONAL INFORMATION

Surname, Name: Elbir, Ahmet Musab

Nationality: Turkish

Date and Place of Birth: 20.10.1987, Malatya, TURKEY

Marital Status: Married

Phone: 0 312 210 4587

Fax: 0 312 210 2304

EDUCATION

Degree	Institution	Year of Graduation
B.S.	Fırat University	2009
High School	Malatya Sümer High School	2005

PROFESSIONAL EXPERIENCE

Year	Place	Enrollment
2011-2016	Middle East Technical University	Research Assistant

PUBLICATIONS

- **Journal Papers**

    1. Ahmet M. Elbir, T. Engin Tuncer, "2-D DOA and Mutual Coupling Co-efficient Estimation for Arbitrary Array Structures With Single and Mul-

tiple Snapshots,"Digital Signal Processing, Volume 54, Pages 75-86, July 2016.

2. Ahmet M. Elbir, T. Engin Tuncer, "Far-field DOA estimation and near-field localization for multipath signals," Radio Science, 49, 9, 765, 2014.

3. Ahmet M. Elbir, T. Engin Tuncer, "Calibration of antenna arrays for aeronautical vehicles on ground," Aerospace Science and Technology, Volume 30, Issue 1, Pages 18-25, October 2013.

- **International Conference Papers**

1. Ahmet M. Elbir, T. Engin Tuncer, "Direction Finding and Localization for Far-Field Sources with Near-Field Multipath Reflections", IEEE Signal Processing & SP Education Workshop, Salt Lake City UT, Aug 2015.

2. Ahmet M. Elbir, T. Engin Tuncer, "Source Localization with Sparse Recovery for Coherent Far- and Near-Field Signals", IEEE Signal Processing & SP Education Workshop, Salt Lake City UT, Aug 2015.

3. Ahmet M. Elbir, T. Engin Tuncer, "Sparse Support Recovery For DOA Estimation In The Presence Of Mutual Coupling," European Signal Processing Conference (EUSIPCO), Nice, Aug 2015.

4. Ahmet M. Elbir, T. Engin Tuncer, "Ground calibration of antenna arrays for complex platforms," Phased Array Systems & Technology, 2013 IEEE International Symposium on, pp.714,718, 15-18 Oct. 2013.

- **National Conference Papers**

1. Ahmet M. Elbir, T. Engin Tuncer, "Compressed Sensing For Single Snapshot Direction Finding In The Presence of Mutual Coupling," in Signal Processing and Communications Applications Conference (SIU), 2016 24th, Zonguldak, Turkey, 16-19 May 2016 (in Turkish).

2. Ahmet M. Elbir, T. Engin Tuncer, "Direction-of-Arrival and Mutual Coupling Coefficient Estimation With A Single Observation For Arbitrary Array Structures," in Signal Processing and Communications Applications Conference (SIU), 2016 24th, Zonguldak, Turkey, 16-19 May 2016 (in Turkish).

3. Ahmet M. Elbir, T. Engin Tuncer, "Sparse signal recovery for localization of coherent far- and near-field signals," in Signal Processing and Communications Applications Conference (SIU), 2015 23th, pp.899-902, Malatya, Turkey, 16-19 May 2015 (in Turkish).

4. Ahmet M. Elbir, T. Engin Tuncer, "Direction finding for far- and near-field sources" National Conference of Defence Technologies, Ankara, Turkey, 25-27 June 2014 (in Turkish).

5. Ahmet M. Elbir, T. Engin Tuncer, "Angle and position estimation for far-field and near-field multipath signals," in Signal Processing and Communications Applications Conference (SIU), 2014 22nd, pp.1379-1382, Trabzon, Turkey, 23-25 April 2014 (in Turkish).

6. Ahmet M. Elbir, T. Engin Tuncer, "Ground calibration of antenna arrays for aeronautical vehicles," in Signal Processing and Communications Applications Conference (SIU), 2013 21st, Cyprus, 24-26 April 2013 (in Turkish).